Mechanisms of variability in Atlantic ocean heat transport and meridional overturning in global climate models

Dylan C. Oldenburg

A dissertation
submitted in partial fulfilment of the
requirements for the degree of

Doctor of Philosophy

University of Washington

2021

Reading Committee:
Kyle Armour, Chair
LuAnne Thompson
Robert Jnglin Wills

Program Authorized to Offer Degree:
School of Oceanography

University of Washington

Abstract

Mechanisms of variability in Atlantic ocean heat transport and meridional overturning in global climate models

Dylan C. Oldenburg

Chair of the Supervisory Committee:
Dr. Kyle Armour
School of Oceanography

Meridional ocean heat transport (OHT) plays a major role in global climate. The Atlantic Ocean is particularly relevant to the global climate because its OHT is northward in both hemispheres due to the existence of the strong Atlantic Meridional Overturning Circulation (AMOC). This thesis gives new insights into what mechanisms drive changes in North Atlantic OHT. The first chapter focuses on the mechanisms that drive changes in OHT into the Arctic from the North Atlantic under both internal variability and CO_2 forced climate change, which are important to understand because the Arctic is experiencing particularly rapid climate change. Our results indicate that the mechanisms differ depending on whether the OHT changes occur under CO_2 forcing or internal variability. We also find that an increase in OHT into the Arctic can occur despite a decrease in the strength of AMOC under global warming. Chapter 2 considers the entire North Atlantic, and aims to determine the mechanisms driving low-frequency OHT variability using a novel method that isolates a mode of low-frequency variability without any explicit low-pass filtering of the data. Here our results suggest that in global climate models, North Atlantic OHT and AMOC are driven primarily by changes in water-mass transformation in the Labrador Sea regardless of which deepwater formation regions dominate the climatological water-mass transformation and AMOC. In Chapter 3, we investigate how these mechanisms differ in higher resolu-

tion models. Chapter 3 Part I focuses on determining how well the time-mean AMOC and high-latitude water-mass transformation are represented in a high-resolution coupled model compared to an equivalent low-resolution version. We find that a high-resolution coupled model reproduces the water-mass transformation found in an atmospheric reanalysis-forced ocean simulation fairly effectively, especially compared to a low-resolution version. Chapter 3 Part II applies a similar analysis to what is used in Chapter 2 to a high-resolution model to see whether the same mechanisms of OHT variability found in low-resolution models hold true. Here we find that, although the Labrador Sea plays a much smaller role in climatological water-mass transformation and AMOC in the high-resolution model compared to the low-resolution version, it still appears to play a major role in the WMT and AMOC variability at decadal and longer timescales. This work as a whole contributes to providing a better understanding of North Atlantic ocean variability, how it differs between models with differing climatologies and resolutions, and how it is linked to Arctic changes.

TABLE OF CONTENTS

LIST OF FIGURES

LIST OF TABLES

ACKNOWLEDGMENTS

I would first like to thank my advisers, Kyle Armour and LuAnne Thompson, without whom this work simply would not have been possible. I am very grateful for all the support that they have given me throughout my Ph.D. and for all that I have learnt from them. They have taught me so much about research methods and effective science communication, which have been essential skills for this work. I would also like to acknowledge my other co-authors for their contributions to this work, especially Robert Jnglin Wills, who has been a major collaborator on two of these chapters. I wish to also thank all the rest of my committee members for their support.

Finally, I wish to acknowledge the National Science Foundation and the National Aeronautics and Space Administration (NASA) for funding these projects.

INTRODUCTION

The oceans play a major role in global climate by transporting heat from low to high latitudes (e.g., Ganachaud and Wunsch 2000). The Atlantic Ocean is of particular relevance to global climate because its meridional ocean heat transport (OHT) is northward in both hemispheres, unlike in the Pacific (e.g., Peixoto and Oort 1993), owing to the existence of a strong Atlantic Meridional Overturning Circulation (AMOC) (Ganachaud and Wunsch, 2003).

The North Atlantic Current, which forms the upper branch of AMOC (e.g. Manabe and Stouffer 1988), brings warm, salty subtropical water northwards into the subpolar region of the North Atlantic, and hence is responsible for transporting large amounts of heat and salt northward. As it moves northward, it releases large amounts of heat to the atmosphere. This heat exchange with the atmosphere helps moderate the European climate (Rahmstorf, 2002; Rhines et al., 2008), and also influences rainfall patterns in the American tropics (Parsons et al., 2014) as well as the frequency of Atlantic hurricanes (e.g. Yan et al. 2017). AMOC also plays a role in Arctic climate variability (e.g. Mahajan et al. 2011; Day et al. 2012; Oldenburg et al. 2018). As the subtropical water moves northward, it begins to freshen, cool and become more dense, transforming into Subpolar Mode Water (Pérez-Brunius et al., 2004; Brambilla and Talley, 2008). This density change is referred to as *water mass transformation*. Surface-forced water-mass transformation can be estimated from air-sea heat and freshwater fluxes (Walin, 1982; Tziperman, 1986; Speer and Tziperman, 1992). Diapycnal mixing and diffusion also contribute to water mass transformation (Swift and Aagaard, 1981; Tziperman, 1986; Böning et al., 1996; Speer, 1997; Nurser et al., 1999; Khatiwala et al., 2002; Bailey et al., 2005; Haines and Old, 2005; Gulev et al., 2007; Radko et al., 2008; Grist et al., 2009, 2012; Trossman et al., 2012; Langehaug et al., 2012a; Grist et al., 2014; Groeskamp

et al., 2017; Megann, 2018; Xu et al., 2018; Garcia-Quintana et al., 2019). Areas with large water mass transformation coincide with deep mixed layers and the production of Subpolar Mode Water, which is the dominant water mass in the eastern subpolar region, above the permanent pycnocline (McCartney and Talley, 1982; Brambilla and Talley, 2008).

The North Atlantic Current splits into several branches, with some branches entering the Nordic Seas and some recirculating through the subpolar gyre towards the Labrador Sea. Approximately half of the North Atlantic Current continues to the Nordic Seas while half recirculates in the subpolar gyre towards the Labrador Sea. Studying the fraction of the transport that travels to different regions is important to understand the composition of the North Atlantic Deep Water that is produced in these regions, as well as the Deep Western Boundary Current (Smethie and Fine, 2001; Lumpkin and Speer, 2003). Regarding the mean circulation, after the North Atlantic Current crosses the Mid Atlantic Ridge at 53°N, it splits into three branches. The first branch passes through the Denmark Strait, the second continues northeastward towards the Nordic Seas, and the final branch recirculates through the subpolar gyre towards the Labrador Sea. North of Iceland, in the Denmark Strait, the poleward flowing warm, salty Atlantic Water mixes with the southward flowing cold, fresh Polar Water from the East Greenland Current (Jónsson and Valdimarsson, 2012). In the Nordic Seas, northward flowing water is transformed into deep water via heat loss to the atmosphere and leaves as southward flowing overflow water through the Greenland-Iceland-Scotland Ridge (Latarius and Quadfasel, 2016).

Warm water from the third branch of the North Atlantic Current recirculates through the Subpolar Gyre, before reaching the Labrador Sea a few hundred meters below the surface (Cuny et al., 2002; Lazier et al., 2002). Heat is carried into the interior Labrador Sea from the boundary current via eddies produced by boundary current instabilities (Lilly et al., 2003; Katsman et al., 2004; Spall, 2004). This water experiences lateral exchange with the cold, fresh surface water from the West Greenland and Labrador Currents. In the winter, deep convection takes place, which is associated with a cooling and freshening of the subsurface water, causing a positive flux of heat and salt to the surface layer and a thickening of the

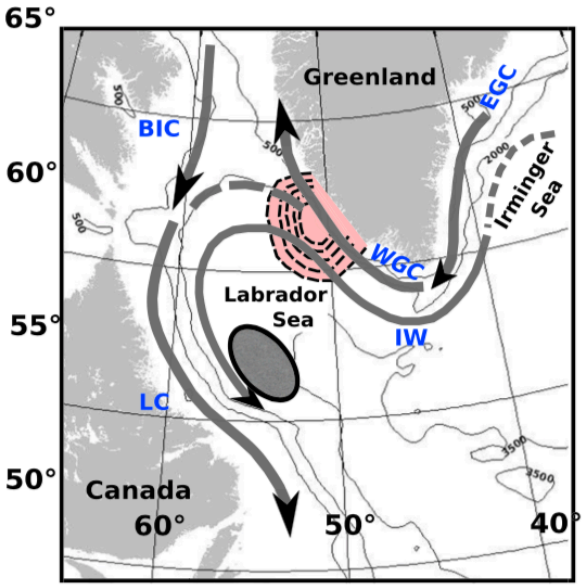

Figure 1: Schematic showing the mean circulation in the subpolar gyre and Labrador Sea. IW refers to Irminger Water, WGC is the West Greenland Current, EGC is the East Greenland Current, BIC is the Baffin Island Current, and LC is the Labrador Current. Figure from Garcia-Quintana et al. (2019).

Labrador Sea Water layer. After the end of winter convection, there is strong lateral exchange between the Central Labrador Sea and water from the boundary current due to mesoscale eddies, governed by the density gradient between the two water masses. This results in the restratification of the interior, i.e. buoyant water is converged and dense Labrador Sea Water formed during convection is exported at depth (Straneo, 2006a), primarily via the Labrador Current (Brandt et al., 2007).

In this dissertation, we will be addressing several research questions. Firstly, in Chapter 1, we seek to elucidate the mechanisms that drive changes in OHT into the Arctic from the North Atlantic, with a primary focus on how these mechanisms differ depending on whether the OHT changes are forced by CO_2 or simply due to internal variability. For the internal variability analysis, we composite on decades with anomalously high OHT at 70° N to determine the relationship between OHT at 70° N and AMOC and the gyre circulation. We also decompose the OHT into thermodynamic and dynamic components to determine how much of the OHT change is due to circulation changes and how much is due to passive temperature changes. For the CO_2 forced analysis, we look at the OHT averaged over the final 30 years of a CO_2 quadrupling simulation and do the same decomposition. In Chapter 2, we use a novel method called a low-frequency component analysis to isolate a mode of variability in North Atlantic OHT that emphasizes low-frequency variability in the OHT. We then carry out a lead-lag regression analysis between several surface properties and the mode of OHT variability to determine the mechanisms driving it. We look at three models with different representations of deep convection in the North Atlantic deepwater formation regions to determine whether the mechanisms remain the same. A key question that we investigate is whether the deepwater formation regions contributing most to AMOC and OHT in the climatology also play a dominant role in driving the low-frequency AMOC and OHT variability. In Chapter 3, we examine how these mechanisms differ for a higher resolution model, and how well the higher resolution model reproduces what is found in atmospheric reanalysis-forced ocean simulations compared to the low-resolution version. In Chapter 3 Part I, we seek to determine how much more accurate the representation of water-mass

transformation is in a high-resolution model compared to a low-resolution version of the same model. To do this, we compare the time-mean surface-forced water-mass transformation in a high and low-resolution version of the same coupled model to ocean simulations forced with atmospheric reanalyses. In Chapter 3 Part II, we use the same analysis as we used in Chapter 2 to look at the mechanisms of AMOC variability in the high-resolution coupled simulation.

Chapter 1

DISTINCT MECHANISMS OF OCEAN HEAT TRANSPORT INTO THE ARCTIC UNDER INTERNAL VARIABILITY AND CLIMATE CHANGE

This chapter is published as: **Oldenburg, D., Armour, K. C., Thompson, L., and Bitz, C. (2018). Distinct mechanisms of ocean heat transport into the Arctic under internal variability and climate change. Geophysical Research Letters, 45, 7692-7700. https://doi.org/10.1029/2018GL078719.**

Abstract

Northward ocean heat transport (OHT) plays a key role in Arctic climate variability and change. Unforced climate model simulations suggest that at decadal and longer timescales, strengthened Atlantic Meridional Overturning Circulation (AMOC) is correlated with increased OHT into the Arctic. Yet, greenhouse-gas (GHG) forced simulations predict increased Arctic OHT while AMOC weakens. Here we partition OHT changes into contributions from `dynamic' circulation changes and `thermodynamic' temperature advection, as well as meridional overturning and gyre changes. We find that under decadal-scale internal variability, strengthened AMOC converges heat in the subpolar gyre; anomalous heat is advected into the Arctic by both time-mean circulations and strengthened gyre circulations. Under GHG forcing, weakened AMOC reduces subpolar gyre heat convergence; yet Arctic OHT increases as mean overturning and strengthened gyre circulations advect warmed surface waters. Thus, caution should be exercised when inferring Arctic OHT from AMOC, as the relationship between OHT and AMOC changes depends on whether they are internally generated or externally forced.

1.1 Introduction

The Arctic has been warming more than twice as rapidly as global average temperature over recent decades (Serreze et al., 2009; Marshall et al., 2014a). This Arctic Amplification of greenhouse-gas (GHG) warming is also a robust feature of global climate model simulations (e.g., Holland and Bitz, 2003; Marshall et al., 2014a; Pithan and Mauritsen, 2014; Marshall et al., 2014b). There is growing evidence that variations in northward ocean heat transport (OHT) into the Arctic from the North Atlantic Ocean play a key role in driving changes in Arctic climate under both internal variability and GHG-induced warming.

Recent studies suggest that the strength of the Atlantic Meridional Overturning Circulation (AMOC) influences Arctic temperature and sea-ice extent on decadal and longer timescales (Mahajan et al., 2011; Day et al., 2012; Chylek et al., 2014; Yeager et al., 2015; Zhang, 2015; Delworth et al., 2016; Li and Knutson, 2017). The apparent mechanism is that strong AMOC leads to enhanced OHT throughout the North Atlantic extending into the higher latitudes through the transport of warmer Atlantic water through the Barents Sea and Eastern Fram Strait (Yeager et al., 2015; Zhang, 2015; Delworth et al., 2016; Li and Knutson, 2017). This suggests a link between variations in AMOC and OHT into the Arctic, with AMOC and associated subpolar gyre (SPG) changes perhaps driven by variability in buoyancy forcing associated with the North Atlantic Oscillation (NAO) (Yeager et al., 2015; Delworth et al., 2016; Delworth and Zeng, 2016). Indeed, it has been proposed that a period of strengthened AMOC in recent decades has contributed to the observed high rate of Arctic warming and sea-ice loss (Chylek et al., 2014; Yeager et al., 2015; Zhang, 2015; Delworth et al., 2016; Li and Knutson, 2017), which is supported by observations showing increased OHT into the Arctic in the Atlantic sector (Schauer et al., 2004; Dmitrenko et al., 2008; Skagseth et al., 2008).

Do similar mechanisms arise under GHG-induced warming? Climate models robustly predict weakening AMOC under GHG forcing, in turn reducing northward heat transport into the SPG (Gregory et al., 2005; Rugenstein et al., 2013; Jungclaus et al., 2014; Kostov

et al., 2014; Marshall et al., 2014b; Huber and Zanna, 2017; Nummelin et al., 2017). Based on the connection between AMOC and OHT seen under internal variability, weakened AMOC should lead to decreased OHT into the Arctic, reducing the pace of Arctic warming and sea-ice loss. Indeed, slower sea-ice loss has been predicted for the next decade based on modeled AMOC declines (Mahajan et al., 2011; Yeager et al., 2015). However, models robustly predict an *increase* in OHT into the Arctic while AMOC weakens under GHG forcing (Holland and Bitz, 2003; Bitz et al., 2006; Hwang et al., 2011; Mahlstein and Knutti, 2011; Rugenstein et al., 2013; Koenigk and Brodeau, 2014; Jungclaus et al., 2014; Marshall et al., 2014b; Nummelin et al., 2017) --- at odds with expectations based on internal variability. Moreover, increased OHT into the Arctic (e.g. across 70°N) is correlated with the degree of Arctic Amplification simulated across models, with increased OHT associated with greater Arctic warming and sea-ice loss (Holland and Bitz, 2003; Hwang et al., 2011; Mahlstein and Knutti, 2011; Nummelin et al., 2017).

Accurate predictions of future Arctic climate and sea ice thus hinge on our ability to predict how OHT will evolve in the future. A key question is, will the recent AMOC weakening (e.g., Smeed et al., 2014; Caesar et al., 2018; Thornalley et al., 2018) result in increased or decreased OHT into the Arctic? Answering this question requires a mechanistic understanding of how the links between AMOC, the SPG circulation and OHT into the Arctic differ under internal variability and GHG forcing.

Different patterns of Atlantic OHT under internal variability and GHG forcing are a robust feature of comprehensive global climate models, such as those participating in phase 5 of the Coupled Model Intercomparison Project (CMIP5; Taylor et al. 2012). In unforced pre-industrial control simulations, decadal variations in OHT into the Arctic (taken at 70°N here, henceforth referred to as OHT_{70}) occur with a strong meridional coherence; that is, OHT anomalies (OHT') have the same sign throughout the North Atlantic basin, from the tropics to the pole (Fig. 1.2a). During decades when OHT_{70} is anomalously large, heat is anomalously converged in the SPG and Arctic, while during decades when OHT_{70} is anomalously weak, heat is anomalously diverged from the SPG and Arctic. In contrast,

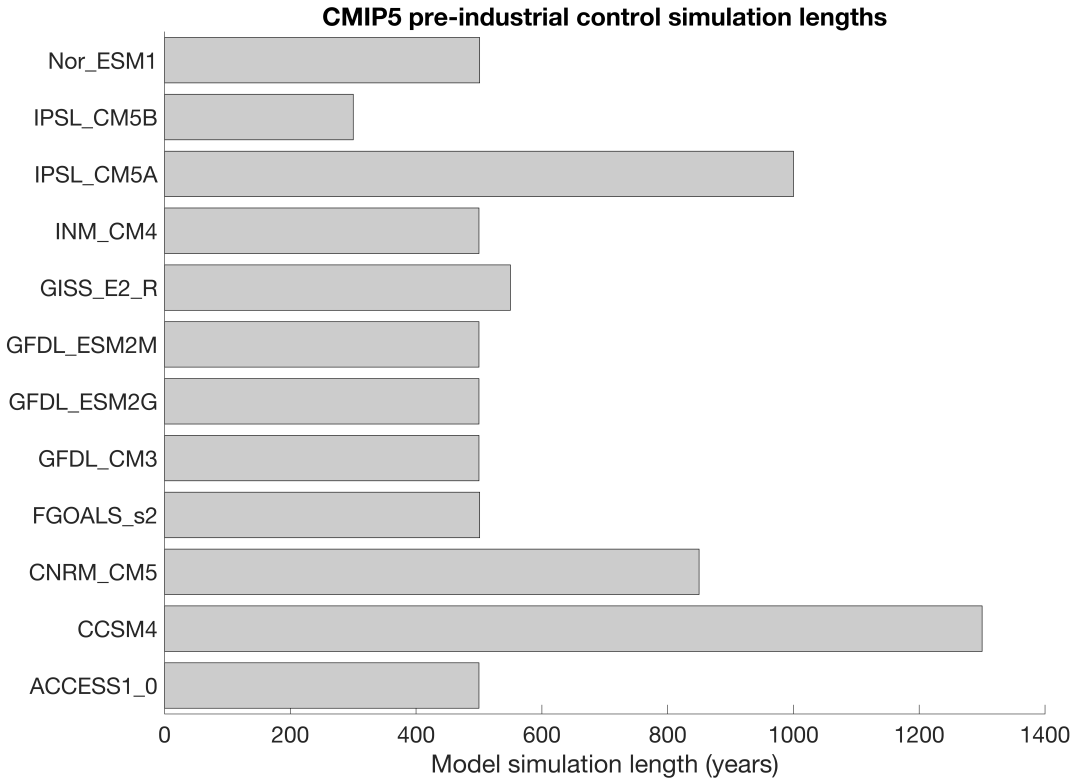

Figure 1.1: Bar graph showing lengths of the CMIP5 pre-industrial control simulations used in Fig. 1.2.

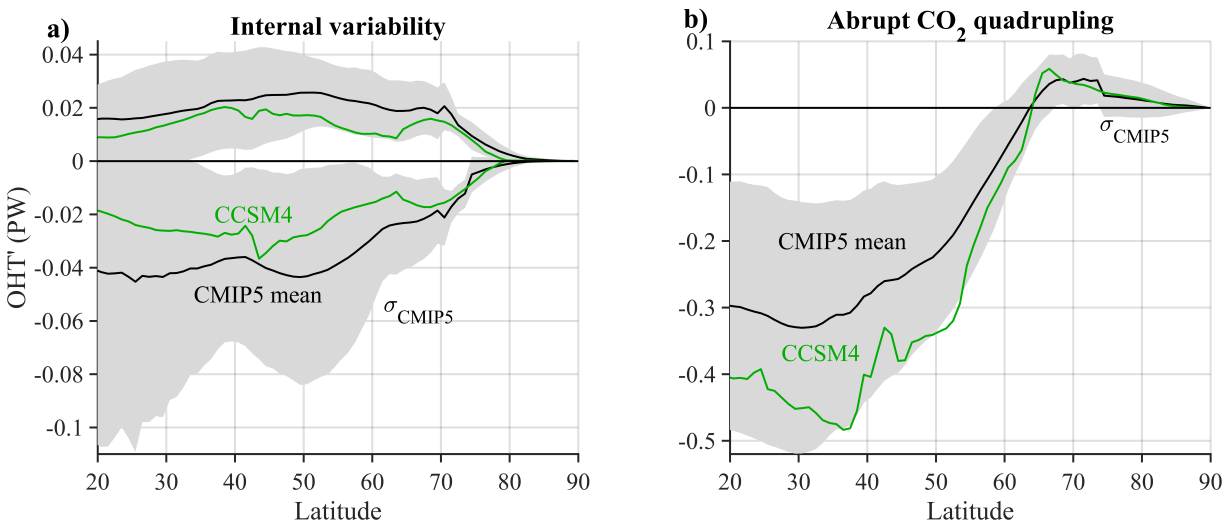

Figure 1.2: OHT′ under internal variability and abrupt CO_2 quadrupling simulations of CMIP5 models. **a)** OHT′ during decades of pre-industrial control simulations in which OHT'_{70} is greater than 1.5σ (top curves) and less than -1.5σ (bottom curves) relative to its long-term average. **b)** OHT′ (relative to the pre-industrial) at year 100 following abrupt CO_2 quadrupling. The black curves show CMIP5 mean (see Fig. 1.1 for the list of models), the grey shading shows the standard deviation across CMIP5 models, and the green curves show CCSM4. OHT′ values are computed from model output OHT ('hfbasin' in the CMIP5 archive) for all CMIP5 models except CCSM4, for which we compute OHT′ from the velocity and temperature fields (Methods).

OHT'_{70} Component	Internal variability	$4\times CO_2$
Total	0.015	0.023
Overturning dynamic	-0.0006	-0.02
Overturning thermodynamic	0.0016	0.087
Gyre dynamic	0.0096	0.059
Gyre thermodynamic	0.0035	-0.093

Table 1.1: Values of the OHT'_{70} components (PW) conditionally averaged over decades in the CCSM4 pre-industrial simulation during which $OHT'_{70} > 1.5\sigma$ and averaged over a 30 year interval centred on year 100 following an abrupt CO_2 quadrupling.

under GHG forcing (abrupt CO_2 quadrupling shown here), OHT_{70} increases even while OHT decreases throughout the mid- to low-latitudes (Fig. 1.2b), concurrent with AMOC weakening (Gregory et al., 2005; Kostov et al., 2014). These OHT anomalies under GHG forcing result in (i) anomalous divergence of heat, and thus cooling or reduced warming, within the SPG (Marshall et al., 2014b; Menary et al., 2015b; Singh et al., 2017), and (ii) anomalous convergence of heat at higher latitudes, enhancing Arctic warming (Marshall et al., 2014b; Nummelin et al., 2017; Singh et al., 2017).

Here we focus on mechanisms of Atlantic OHT changes in one particular model, the Community Climate System Model Version 4 (CCSM4; Gent et al. 2011), that simulates changes consistent with the behavior seen across CMIP5 models (Fig. 1.2). We seek to develop a mechanistic understanding of how changes in AMOC and SPG circulation are connected to OHT further north within the Nordic Seas, and of how the operation of these mechanisms may differ under GHG forcing and internal variability. In particular, we decompose and interpret OHT changes at different latitudes in terms of `dynamic' changes in ocean circulation versus `thermodynamic' temperature advection, and in terms of meridional overturning and gyre circulations. Following recent papers on the topic (e.g., Koenigk and Brodeau 2014; Zhang 2015), we focus on northward OHT crossing the Arctic Circle (taken here to be around

70°N), which is representative of OHT into the high latitudes.

1.2 Methods

To examine the mechanisms of OHT changes under internal variability, we use CCSM4's pre-industrial (PI) control simulation, which is 1300 years long and unforced (with constant 1850s GHG and aerosol levels and no volcanic eruptions). For GHG forcing, we consider CCSM4's 150-year long simulation of abrupt CO_2 quadrupling ($4\times CO_2$) relative to PI levels. We remove linear drifts over the PI control from all variables prior to analysis. The $4\times CO_2$ simulation allows us to study the ocean's time-dependent response to CO_2 forcing without having to account for the temporal variations of GHGs or other forcing agents, and is a sufficiently large forcing that changes are well outside the bounds of internal variability. Our analysis of forced response thus differs from previous studies that consider OHT changes under specific historical and future emissions scenarios (Bitz et al., 2006; Jungclaus et al., 2014; Nummelin et al., 2017). We focus on OHT into the Arctic from the Atlantic sector since it is substantially larger than OHT in the Pacific sector (across Bering Strait) in both time-mean and anomalies under internal variability and GHG forcing.

1.2.1 Calculating OHT and its components

OHT as a function of latitude and time is given by

$$\mathrm{OHT}(y,t) = \rho c_p \int_{x_1}^{x_2} \int_{z_{bot}}^{0} v\theta dz dx, \tag{1.1}$$

where ρ is the density, which is assumed to be uniform, and c_p is the heat capacity of seawater; z_{bot} is the ocean bottom depth; x_1 and x_2 are the longitude limits; θ is the monthly potential temperature as a function of x (longitude), y (latitude), z (depth) and t (time); and v is the monthly-resolved Eulerian-mean velocity. Bolus, diffusion and submesoscale flux terms make negligible contributions to OHT or its changes within the domain of our analysis (North Atlantic and Nordic Seas). Errors in OHT introduced by using monthly-mean velocity and temperature are estimated to be of order a few percent at all latitudes.

Borrowing the terminology of previous studies (e.g. Bony et al. 2004), OHT anomalies can be decomposed into contributions from (i) `dynamic' changes in circulation (anomalous currents advecting time-mean heat content), (ii) `thermodynamic' changes in temperature (anomalous heat advected by time-mean circulations), and (iii) a `nonlinear' term representing the higher order contributions to OHT$'$ from simultaneous changes in temperature and circulation:

$$\mathrm{OHT}'(y,t) = \underbrace{\rho c_p \int_{x_1}^{x_2}\int_{z_{bot}}^{0} \overline{v}\theta' dz dx}_{\text{thermodynamic}} + \underbrace{\rho c_p \int_{x_1}^{x_2}\int_{z_{bot}}^{0} v'\overline{\theta} dz dx}_{\text{dynamic}} + \underbrace{\rho c_p \int_{x_1}^{x_2}\int_{z_{bot}}^{0} v'\theta' dz dx,}_{\text{nonlinear}} \quad (1.2)$$

where overbars represent a time mean of a given variable (i.e., $\overline{v}$ and $\overline{\theta}$), and primes represent temporal anomalies of a variable relative to its time mean (i.e., v' and θ').

The grid of the ocean model within CCSM4 is not rectilinear. The OHT calculation is started by a direct calculation of OHT at 34°S, the southernmost tip of Africa, where the east-west grid line follows a line of constant latitude. Then, using the model T, u, and v fields, the divergence of heat transport for each T grid cell is calculated. The OHT at each target latitude north of 34°S is then calculated as the sum of the divergence of all T grid cells between the target latitude and 34°S plus the OHT at 34°S. We follow the same procedure for computing the dynamic, thermodynamic and nonlinear components.

We further decompose dynamic, thermodynamic, and nonlinear OHT$'$ into overturning and gyre components. The overturning components of each are calculated from the zonal-mean potential temperature, $\langle\theta\rangle$, and the meridional overturning stream function, ψ, according to:

$$\mathrm{OHT}'_{\mathrm{MOC}}(y,t) = \underbrace{\rho c_p \int_{z_{bot}}^{0} \overline{\psi}\frac{\partial\langle\theta\rangle'}{\partial z} dz}_{\text{thermodynamic}} + \underbrace{\rho c_p \int_{z_{bot}}^{0} \psi'\frac{\partial\overline{\langle\theta\rangle}}{\partial z} dz}_{\text{dynamic}} + \underbrace{\rho c_p \int_{z_{bot}}^{0} \psi'\frac{\partial\langle\theta\rangle'}{\partial z} dz,}_{\text{nonlinear}} \quad (1.3)$$

where

$$\psi(y,z,t) = -\int_{z}^{0}\int_{x_1}^{x_2} v(x,y,\tilde{z},t) dx d\tilde{z}. \quad (1.4)$$

The gyre component of OHT can be expressed as:

$$\mathrm{OHT}'_{\mathrm{gyre}}(y,t) = \rho c_p \int_{z_{bot}}^{0}\int_{x_1}^{x_2} \dot{v}\dot{\theta} dx dz \quad (1.5)$$

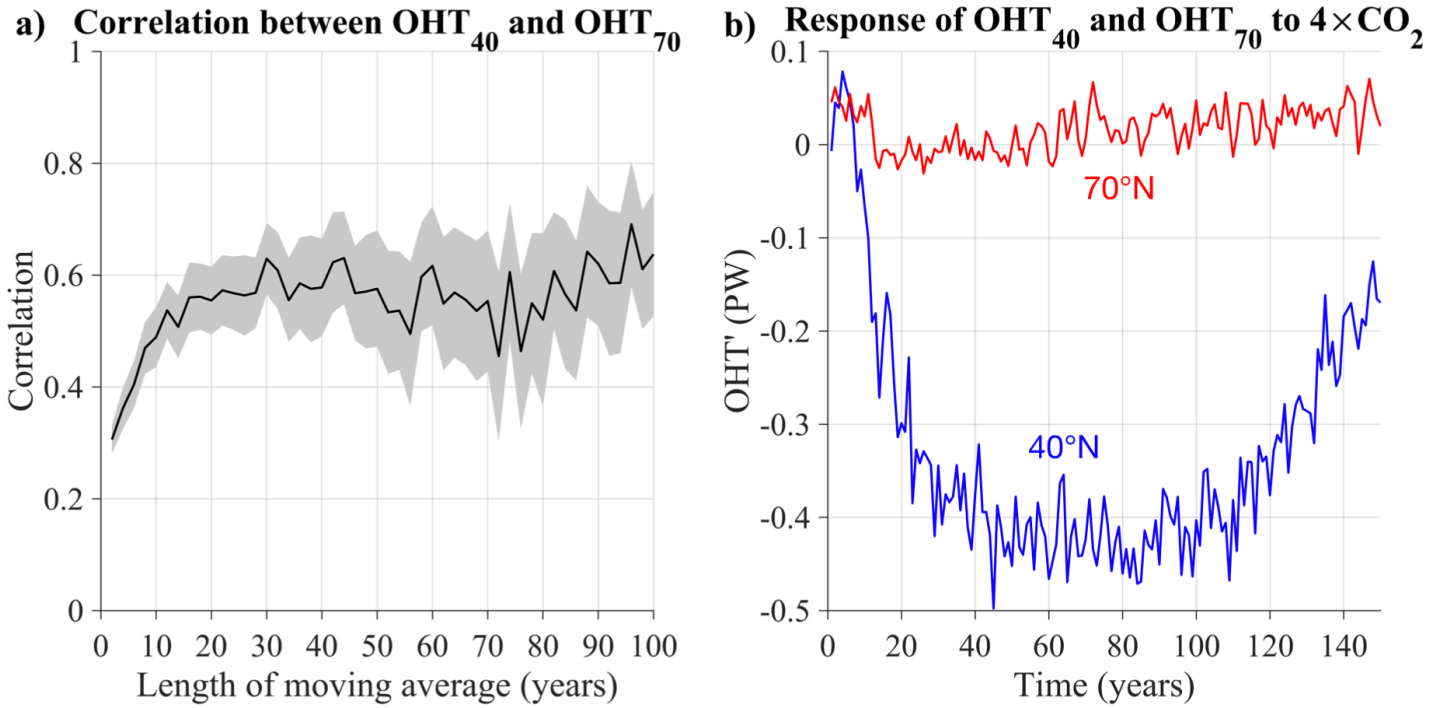

Figure 1.3: a) Correlation coefficient between OHT_{40} and OHT_{70} as a function of timescale in the CCSM4 1300 year pre-industrial simulation. The grey shading shows the uncertainty of the correlation, computed via the bootstrapping method. b) OHT' time series at 40°N (blue) and 70°N (red) during the $4\times\mathrm{CO}_2$ simulation. 40°N is chosen because this is near the latitude of maximum pre-industrial mean overturning.

where $\dot{v}$, $\dot{\theta}$ are anomalies relative to the zonal mean at each latitude. As is typical in observational studies (L. Bryden and Imawaki, 2001; Piecuch and Ponte, 2011), we calculate $\mathrm{OHT}'_{\mathrm{gyre}}$ as a residual between OHT' and $\mathrm{OHT}'_{\mathrm{MOC}}$. This is based on the assumptions that there is no meridional mass transport through the ocean basin and that the transport associated with parameterized eddies is small.

Internal variability in OHT

Motivated by previous studies (Mahajan et al., 2011; Day et al., 2012; Yeager et al., 2015; Zhang, 2015; Delworth et al., 2016), we focus on mechanisms of internal, decadal-scale OHT

variability. At decadal timescales there is a high positive correlation between OHT'_{70} and OHT' in the mid-latitudes within PI control simulations (Fig. 1a and Fig. 1.3), suggesting a potential link between changes in AMOC and OHT_{70}. This positive correlation remains high for variability at multidecadal timescales, but decreases toward interannual timescales (Fig. 1.3).

To isolate internal variability of OHT at decadal timescales, we calculate monthly Atlantic OHT over the length of CCSM4's PI control simulation and take 10-yr moving averages with each interval overlapping the previous by half. For each decadal average, we calculate OHT' and its components, where anomalies are defined with respect to the time-mean over the PI control. To focus on OHT into the Arctic, we conditionally average all OHT components during the 10-yr periods during which OHT'_{70} is greater than 1.5 standard deviations (σ) away from its time-mean value (Fig. 1a); results are similar if other choices, such as 1σ or 2σ, are used instead. In the analysis below, we focus on the periods when OHT'_{70} is large for a more direct comparison to the mechanisms of increased OHT_{70} under GHG forcing. Results are nearly symmetric for $OHT'_{70} > 1.5\sigma$ and $OHT'_{70} < -1.5\sigma$ (Fig. 1.4).

GHG-forced changes in OHT

To analyze the mechanisms governing GHG-forced changes in OHT into the Arctic, we calculate monthly Atlantic OHT over the length of CCSM4's $4\times CO_2$ simulation and over the concurrent 150 years of the PI control. We calculate OHT' and its components relative to the PI control. For our main analysis, we consider OHT' averaged over a 30-yr period around year 100 (years 86-115) following CO_2 quadrupling; other periods, such as 30-yr intervals around year 70 or year 130, yield similar results (Fig. 1.5).

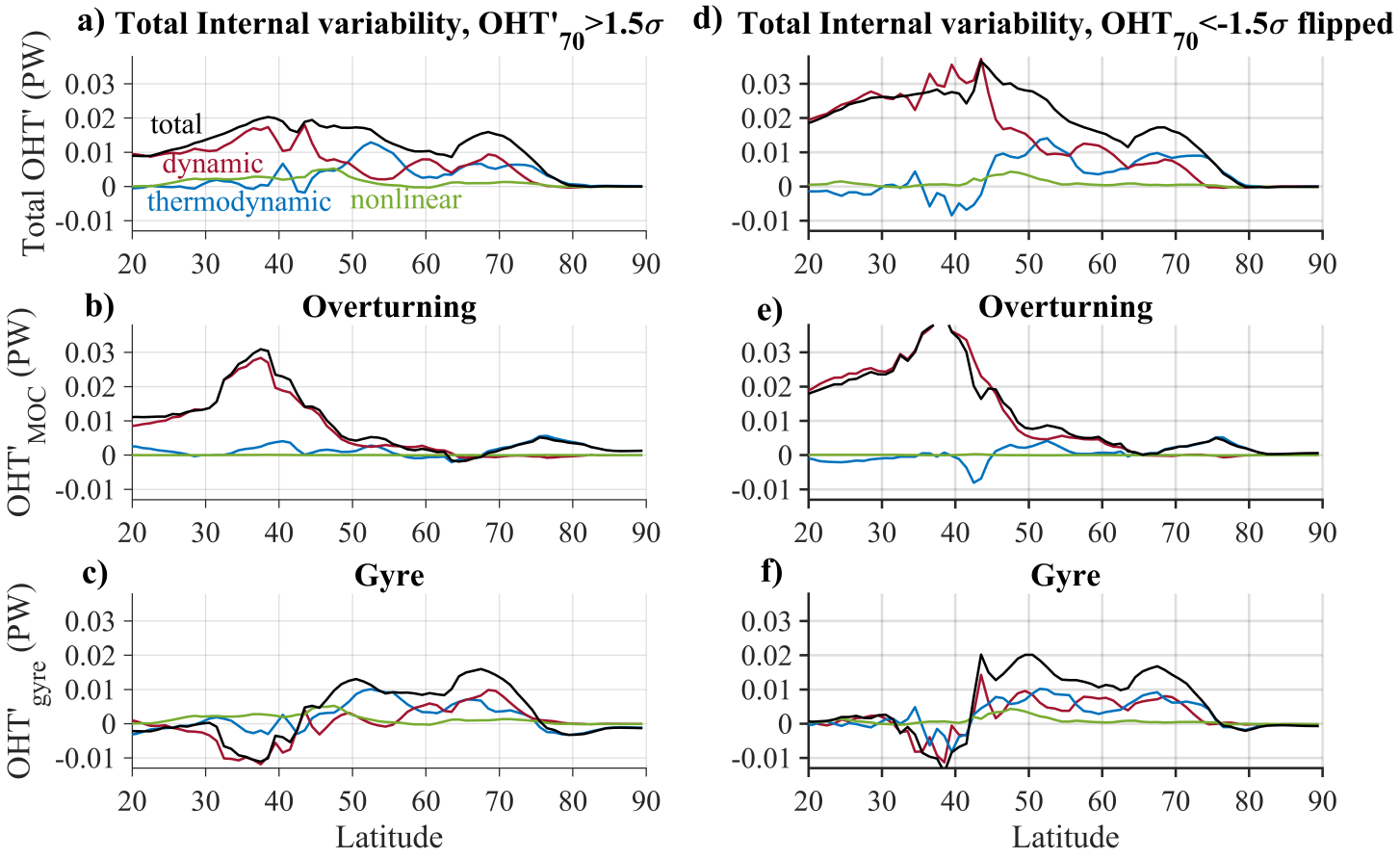

Figure 1.4: Overturning and gyre, as well as dynamic, thermodynamic and nonlinear contributions to OHT′ under internal variability simulations of CCSM4. a) Total OHT′ components conditionally averaged over decades in the PI control simulation during which $\mathrm{OHT}'_{70} > 1.5\sigma$. b) Overturning OHT′ components. c) Gyre OHT′ components. d) Total OHT′ components conditionally averaged over decades in the PI control simulation during which $\mathrm{OHT}'_{70} < -1.5\sigma$, flipped about the y-axis for easier comparison. e) Overturning OHT′ components. f) Gyre OHT′ components.

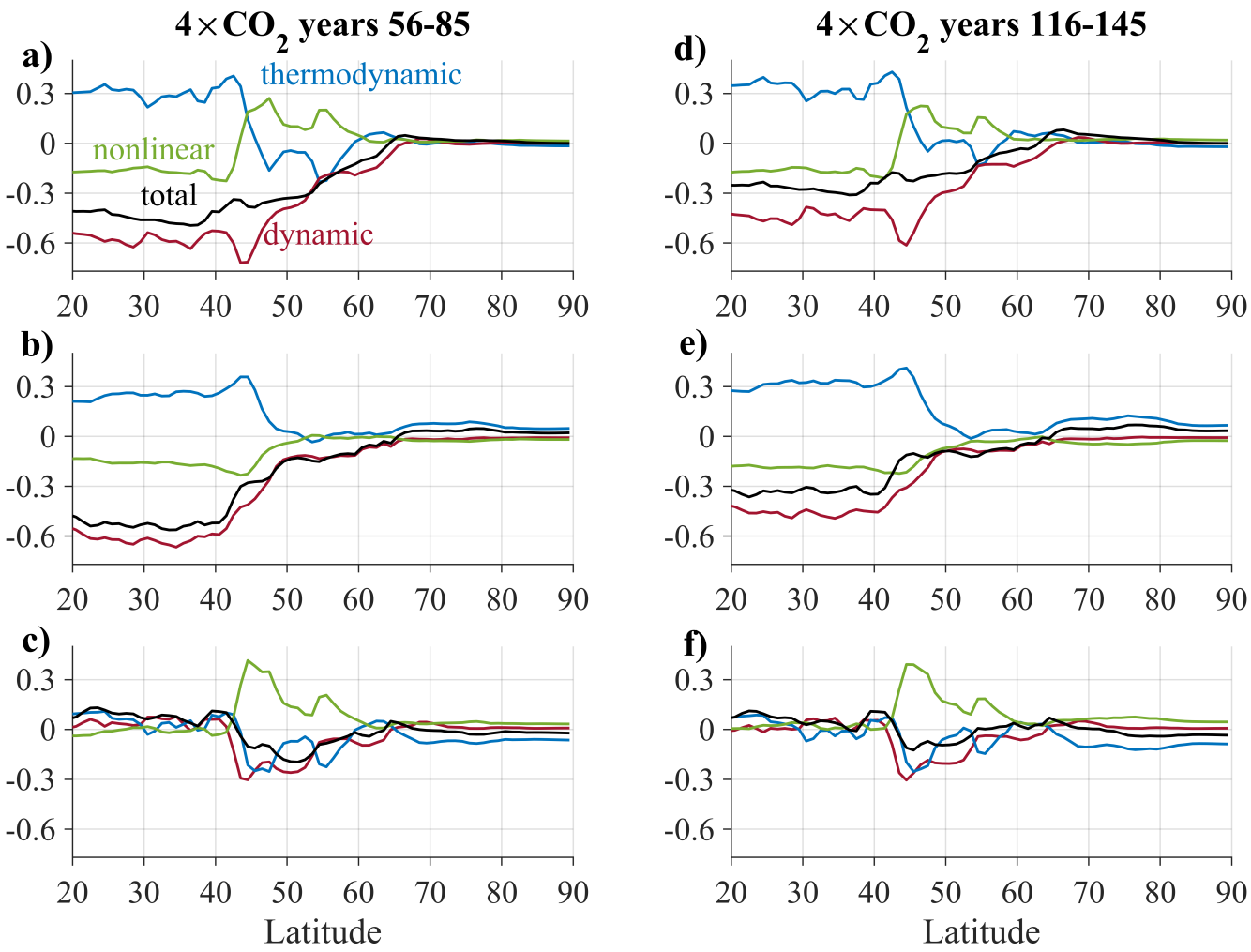

Figure 1.5: Overturning and gyre, as well as dynamic, thermodynamic and nonlinear contributions to OHT′ under abrupt CO_2 quadrupling simulations of CCSM4. a) Total OHT′ components averaged over years 56-85 following abrupt CO_2 quadrupling. b) Overturning components. c) Gyre components. d) Total OHT′ components averaged over years 116-145 following abrupt CO_2 quadrupling. e) Overturning components. f) Gyre components.

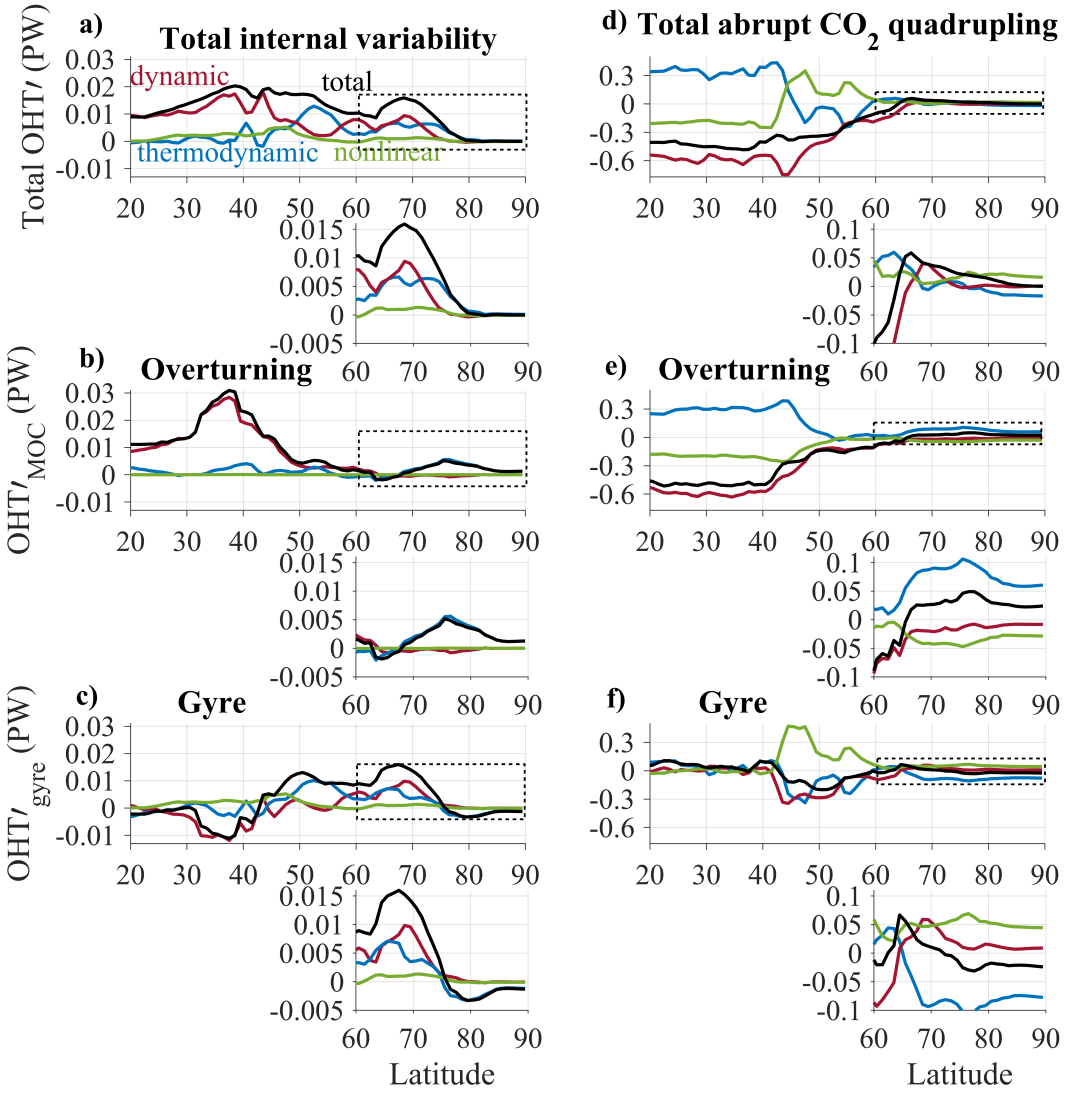

Figure 1.6: Overturning and gyre, as well as dynamic, thermodynamic and nonlinear contributions to OHT' under internal variability (left) and abrupt CO_2 quadrupling (right) simulations of CCSM4. a) Total OHT' components conditionally averaged over decades in the PI control simulation during which $\mathrm{OHT}'_{70} > 1.5\sigma$. b) Overturning OHT' components. c) Gyre OHT' components. d) Total OHT' components averaged over a 30 year interval centred on year 100 following an abrupt CO_2 quadrupling. e) Overturning OHT' components. f) Gyre OHT' components.

1.3 Results

1.3.1 Mechanisms of OHT changes under internal variability

During decades of the PI control simulation when $\mathrm{OHT}'_{70} > 1.5\sigma$, OHT' is also positive from the equator to the North Pole (Fig. 1.6a). The latitudinal variations in OHT' indicates that heat is anomalously converged over most latitudes poleward of 40°N, and most strongly within the SPG (50° to 60°N) and Arctic (poleward of 70°N).

What circulations contribute to these OHT anomalies? In the mid-latitudes (equatorward of about 45°N), positive OHT' arises from anomalous $\mathrm{OHT}_{\mathrm{MOC}}$ (Fig. 1.6b), with changes in $\mathrm{OHT}_{\mathrm{gyre}}$ slightly opposing the total OHT' (Fig. 1.6c). Moreover, mid-latitude OHT', $\mathrm{OHT}'_{\mathrm{MOC}}$ and $\mathrm{OHT}'_{\mathrm{gyre}}$ primarily reflect dynamic changes in circulations, with relatively small thermodynamic and negligible nonlinear components.

Within the SPG (50° to 60°N), OHT' is positive, primarily owing to thermodynamic $\mathrm{OHT}'_{\mathrm{gyre}}$ (Fig. 1.6c). OHT' is positive in the Nordic Seas and at 70°N primarily owing to $\mathrm{OHT}'_{\mathrm{gyre}}$, split about equally between dynamic and thermodynamic gyre changes; $\mathrm{OHT}'_{\mathrm{MOC}}$ plays a minor role at these latitudes. This suggests a hand-off across latitudes in which heat converged on the southern edge of the SPG by changes in meridional overturning is carried further northward by the time-mean SPG circulation and converged into the Arctic by both dynamic and thermodynamic gyre components. Nonlinear components are, as expected, small compared to the other components since both v' and T' are small under internal variability relative to $\overline{v}$ and $\overline{T}$. Values of the OHT'_{70} components under internal variability are given in Table 1.1.

The components of OHT' can be physically understood in terms of either time-mean or anomalous circulations acting on time-mean or anomalous ocean potential temperatures. Figs. 1.7a, b show the MOC and potential temperature patterns conditionally averaged over the same decades during which OHT'_{70} is high. AMOC is anomalously strong during these decades (Fig. 1.7a), consistent with positive dynamic $\mathrm{OHT}'_{\mathrm{MOC}}$ in the mid-latitudes. Surface waters in the mid-latitudes are anomalously warm (Fig. 1.7b), slightly enhancing

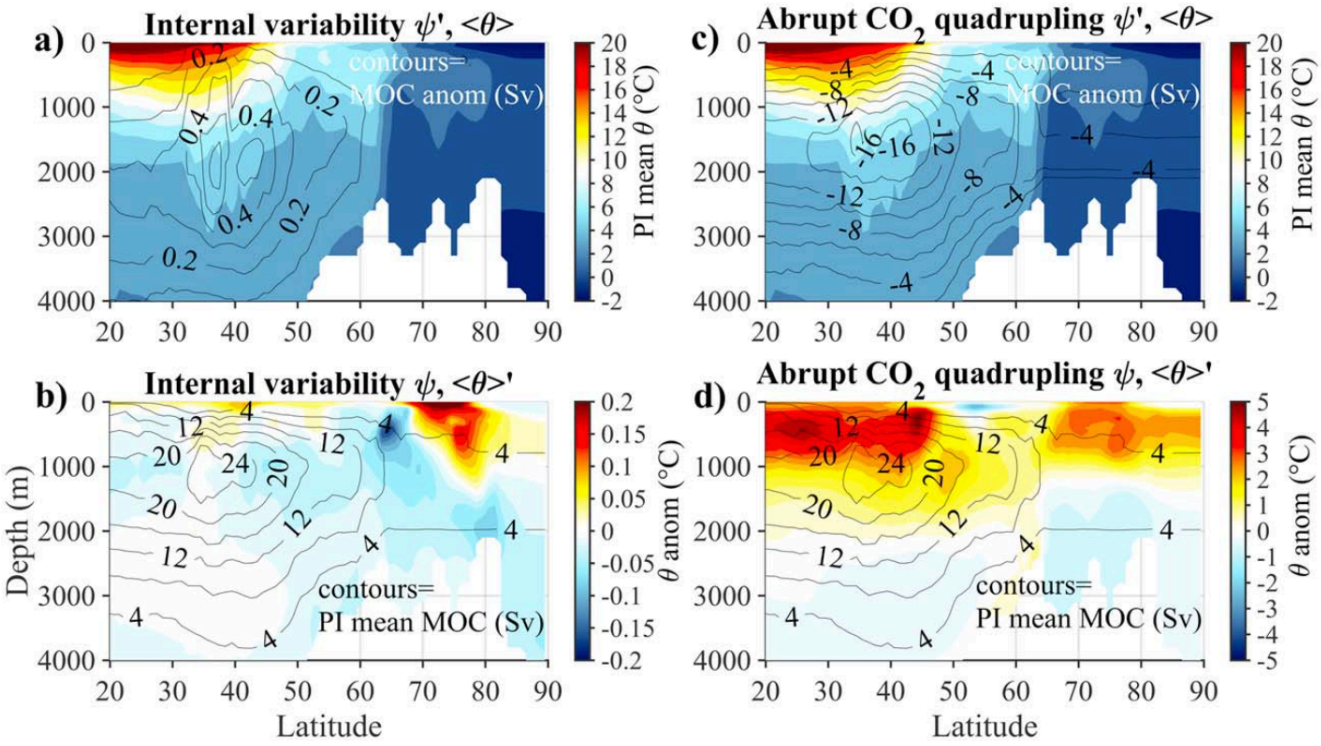

Figure 1.7: Meridional overturning and zonal-mean potential temperature anomalies under internal variability (left) and abrupt CO_2 quadrupling (right) simulations of CCSM4. a) MOC anomalies conditionally averaged over decades in the pre-industrial simulation during which $\mathrm{OHT}'_{70} > 1.5\sigma$ (contours, spaced every 0.1 Sv). Colors show PI control average zonal-mean θ. b) PI control average MOC (contours, spaced every 4 Sv). Colors show zonal-mean θ anomalies. c) MOC anomalies under abrupt CO_2 quadrupling (contours, spaced every 2 Sv). Colors show PI control average zonal-mean θ. d) PI control average MOC (contours, spaced every 4 Sv). Colors show zonal-mean θ anomalies.

the vertical temperature gradient on which the time-mean overturning acts, consistent with a weak but positive thermodynamic $\mathrm{OHT}'_{\mathrm{MOC}}$ in the mid-latitudes. Meanwhile, the MOC weakens slightly near 70°N (Fig. 1.7a), but because this overturning acts on a relatively weak time-mean vertical temperature gradient it has a minimal effect on OHT'_{70}. Surface waters are anomalously warm at 70°N (Fig. 1.7b), enhancing the vertical temperature gradient on which the time-mean overturning acts, consistent with a thermodynamic $\mathrm{OHT}'_{\mathrm{MOC}}$ that contributes to OHT'_{70}.

We also consider changes associated with the barotropic circulation (Figs. 1.8a, b). Because the barotropic circulation is a depth-integrated streamfunction, it lacks a baroclinic component and thus its heat transport only approximates $\mathrm{OHT}_{\mathrm{gyre}}$ (Fig. 1.9). Nonetheless, it is useful for gaining physical understanding. During decades when OHT'_{70} is high, the barotropic circulation is anomalously strong everywhere poleward of about 45°N. Given that the time-mean depth-averaged ocean potential temperature is generally warmer in the east than the west at these latitudes, these circulation changes are consistent with positive dynamic $\mathrm{OHT}'_{\mathrm{gyre}}$. Moreover, depth-averaged ocean potential temperature increases by more in the east than the west poleward of about 45°N, enhancing the zonal temperature gradient on which the barotropic circulation acts, consistent with positive thermodynamic $\mathrm{OHT}'_{\mathrm{gyre}}$ in the SPG and at 70°N.

The results described above hold for internal variability at multidecadal (e.g., 30-yr) timescales. However, at interannual timescales, OHT_{70} variability is dominated by local gyre circulation changes at 70°N, with little changes in ocean temperature, only localized mid-latitude MOC changes, and a lack of meridional coherence in OHT' (not shown). Our interpretation is that the links between OHT_{70} and AMOC changes hold at decadal and longer timescales, while at shorter timescales OHT_{70} changes become primarily driven by local wind variability.

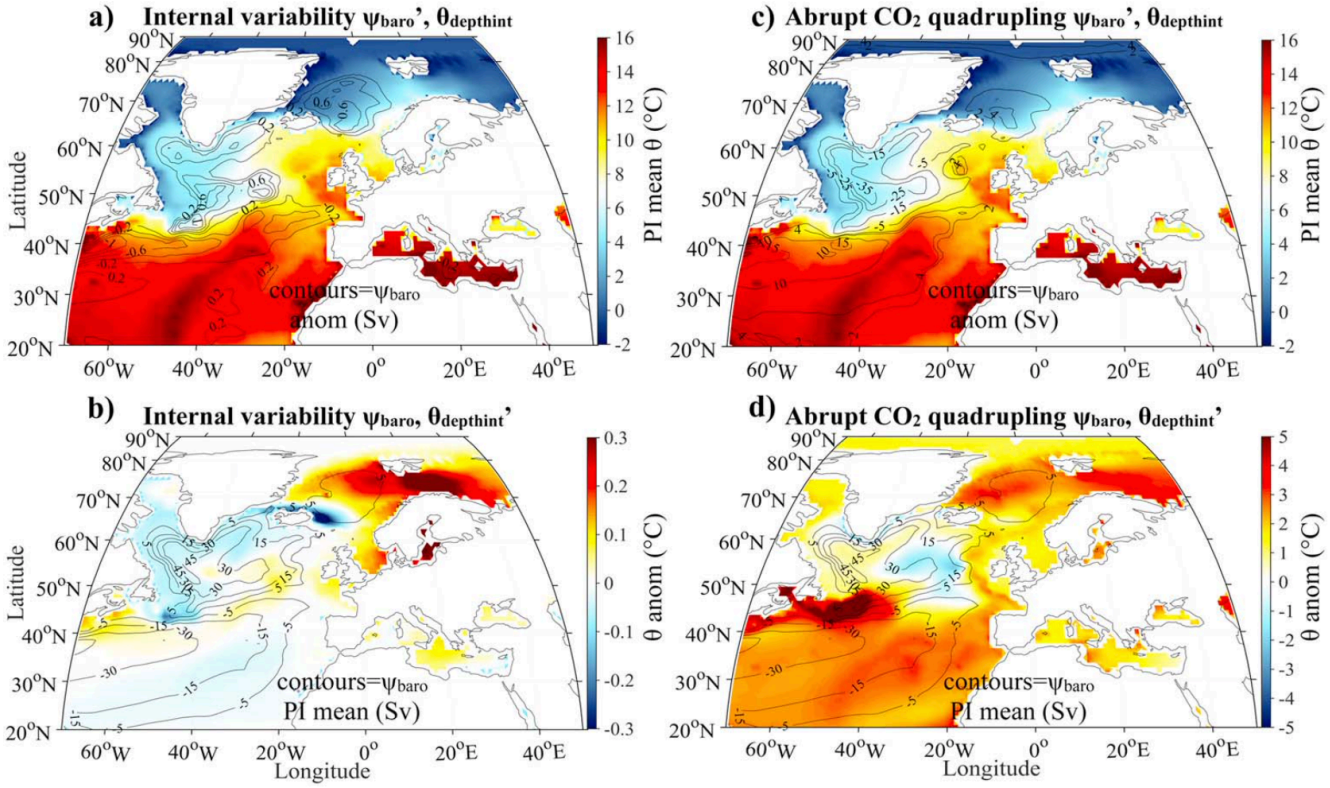

Figure 1.8: Barotropic streamfunction and depth-averaged potential temperature anomalies under internal variability (left) and abrupt CO_2 quadrupling (right) simulations of CCSM4. Positive values indicate counterclockwise circulation; negative values indicate clockwise circulation. a) Barotropic streamfunction anomalies conditionally averaged over decades in the pre-industrial simulation during which $\mathrm{OHT}'_{70} > 1.5\sigma$ (contours, spaced every 0.2 Sv). Colors show PI control average depth-averaged θ. b) PI control average barotropic streamfunction (contours). Colors show depth-averaged θ anomalies. c) Barotropic streamfunction anomalies under abrupt CO_2 quadrupling (contours). Colors show PI control average depth-averaged θ. d) PI control average barotropic streamfunction (contours). Colors show depth-averaged θ anomalies.

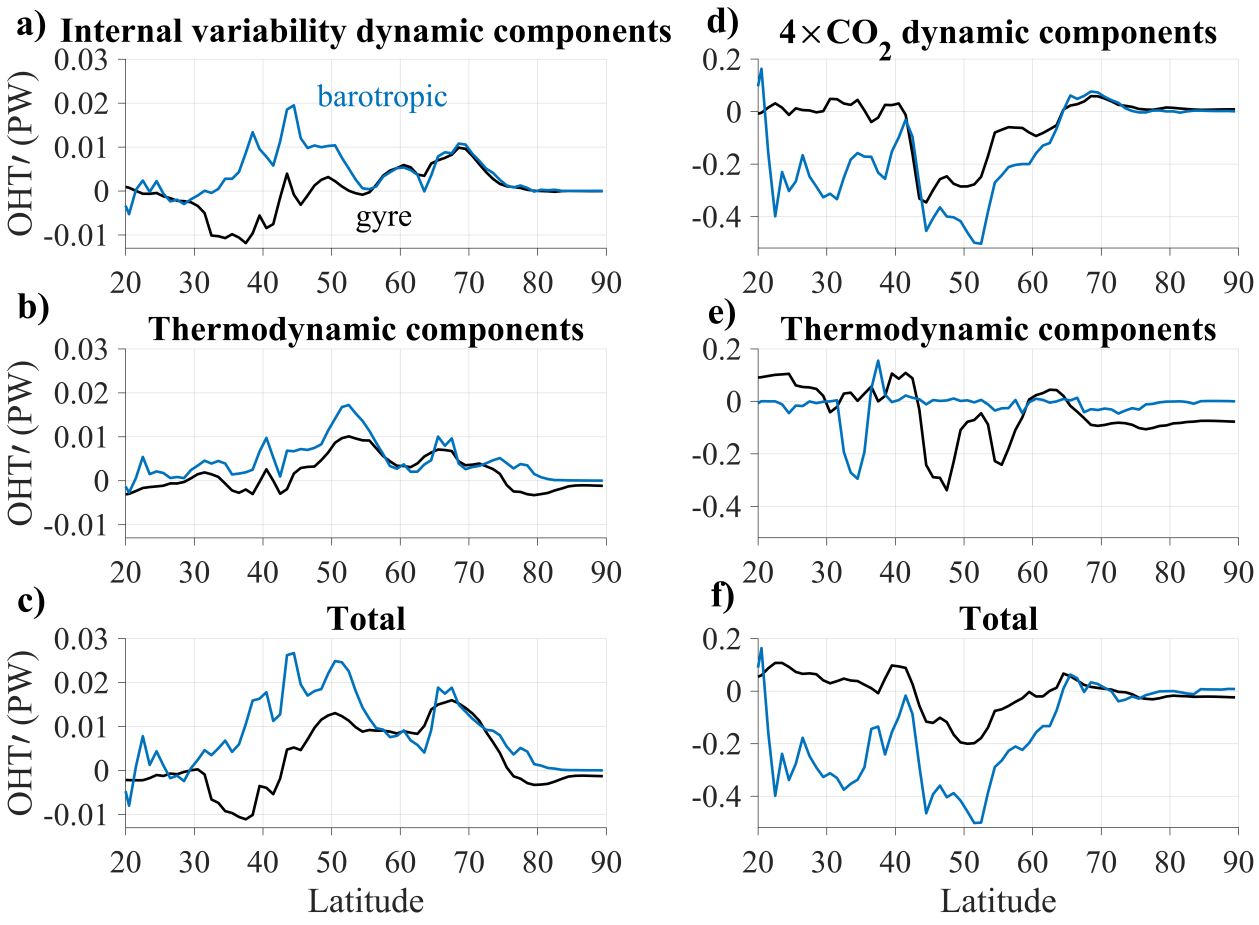

Figure 1.9: Comparison of barotropic versus gyre OHT components under internal variability simulations of CCSM4 (a)-c)) and averaged over years 86-115 after a CO_2 quadrupling (d)-f)).

1.3.2 Mechanisms of OHT changes under GHG forcing

Averaged around year 100 following abrupt CO_2 quadrupling, OHT' is negative south of 65°, and positive north of there. The variations in OHT' with latitude indicate that heat is anomalously diverged between 38°N and 42°N, anomalously converged between 42°N and 45°N, anomalously diverged between 45°N and 67°N (i.e. in the SPG), and anomalously converged between 67°N and the pole (Fig. 1.2d).

What circulations contribute to these OHT' values? In the mid-latitudes, negative OHT' is owing to both negative OHT'_{MOC} (Fig. 1.2e) and OHT'_{gyre} (Fig. 1.2f). Both dynamic and thermodynamic changes contribute to OHT'_{MOC} and OHT'_{gyre}. For OHT'_{MOC}, the negative dynamic component is about twice the magnitude of the positive thermodynamic component, and hence the total OHT'_{MOC} is negative.

Within the SPG (50° to 60°N), OHT' is negative owing to both dynamic and thermodynamic OHT'_{gyre} (Fig. 1.6f), with a small contribution from dynamic OHT_{MOC}. Positive OHT' in the Nordic Seas and at 70°N primarily reflects positive OHT'_{MOC}, split between a positive thermodynamic component and a much smaller negative dynamic component. OHT'_{gyre} actually provides a negative contribution to OHT'_{70}, since the thermodynamic component at 70°N is negative and large in magnitude, overwhelming the positive dynamic component. This suggests that water warmed by GHG forcing in the high latitudes is converged into the Arctic by both thermodynamic meridional overturning and gyre circulations. The nonlinear components are comparable in magnitude to the other components because v' and T' under GHG forcing are similar in magnitude to $\overline{v}$ and $\overline{T}$. Values of the OHT'_{70} components under abrupt CO_2 quadrupling are given in Table 1.1.

Figures 1.7c, d show the MOC and potential temperature anomalies around year 100 after abrupt CO_2 quadrupling. A weak AMOC (Fig. 1.7c) is consistent with a negative dynamic OHT'_{MOC} in the mid-latitudes. Surface waters in the mid-latitudes are anomalously warm (Fig. 1.7d), slightly enhancing the vertical temperature gradient on which the time-mean overturning acts, consistent with a positive thermodynamic OHT'_{MOC} in the mid-latitudes.

Meanwhile, the MOC weakens near 70°N (Fig. 1.7c), but because this overturning acts on a relatively weak time-mean vertical temperature gradient it has a small effect on OHT'_{70}. Surface waters are anomalously warm at 70°N (Fig. 1.7d), enhancing the vertical temperature gradient on which the time-mean overturning acts, consistent with a positive dynamic OHT'_{MOC} that contributes to OHT'_{70}.

Meanwhile, the barotropic circulation becomes anomalously weak in the SPG (between 45°N and 60°N; Fig. 1.8c). Given that the time-mean depth-averaged ocean potential temperature is generally warmer in the east than the west at these latitudes, these circulation changes are consistent with a negative dynamic OHT'_{gyre}. Moreover, depth-averaged ocean potential temperature is seen to increase everywhere besides a small warming hole in the SPG, owing to a divergence of heat from the region. The depth-averaged ocean potential temperature increases by more in the west than the east poleward of about 45°N, weakening the zonal temperature gradient on which the barotropic circulation acts, consistent with a negative thermodynamic OHT'_{gyre} in the SPG and at 70°N (Fig. 1.8d).

1.4 Discussion & Conclusions

Within CCSM4's PI control simulation, we find that AMOC plays a central role in changes in OHT into the Arctic under internal variability at decadal (and longer) timescales. During decades when OHT'_{70} is high, enhanced AMOC results in anomalous heat convergence at the southern flank of the SPG; anomalous heat is then carried northward to the Nordic Seas primarily by the time-mean SPG circulation. Within the Nordic Seas and at 70°N, high OHT' is due in about equal parts to (i) thermodynamic advection of heat by time-mean gyre circulations and (ii) dynamic heat redistribution by strengthened gyre circulations. These results suggest there is a complex hand-off of heat between overturning and gyre circulations at different latitudes under internal variability, with a strong AMOC correlated with enhanced OHT_{70}.

Within CCSM4's simulation of abrupt CO_2 quadrupling, we find that both AMOC and the SPG circulation weaken substantially, resulting in less heat convergence into the SPG.

Yet, owing to the GHG forcing, surface waters are warmed everywhere poleward of 60°N, resulting in thermodynamic northward advection of heat by time-mean circulations and heat convergence near 70°N. At 70°N, heat is anomalously carried northward by (i) thermodynamic advection by time-mean overturning circulations and (ii) dynamic heat redistribution by strengthened gyre circulations. These results suggest that OHT_{70} increases under GHG forcing, despite weakening AMOC.

Previous studies of internal variability suggest that positive OHT'_{70} arises from enhanced delivery of warm waters into the Nordic Seas by AMOC and subsequent thermodynamic advection of this heat into the Arctic (Day et al., 2012; Zhang, 2015). Nummelin et al. 2017 propose a similar mechanism for positive OHT'_{70} under GHG forcing: anomalous heat originating from reduced heat loss in the SPG is advected northward by time-mean circulations. However, our results suggest that the situation is more complicated: a portion of OHT'_{70} under both internal variability and GHG forcing can be attributed to thermodynamic advection of anomalously warm water, yet the majority of OHT'_{70} arises from changes in ocean circulation at 70°N. Moreover, we find that these circulation changes at 70°N are different under internal variability and GHG forcing. While CMIP5 models robustly show an increased OHT'_{70} in response to GHG forcing, the partitioning of dynamic/thermodynamic and MOC/gyre components appears to vary between different models [e.g. Bitz et al. 2006; Koenigk and Brodeau 2014; Marshall et al. 2014b; Jungclaus et al. 2014]. It thus seems possible that mechanisms driving OHT'_{70} differ between models, perhaps due to different representations of the location of deep convection and/or of transport across the Iceland/Scotland Ridge. It is also possible that more realistic forcing scenarios that include non-CO_2 forcings (e.g., aerosols) may produce different results.

We have homed in on the mechanisms of changes in OHT into the Arctic, and found interactions between overturning and gyre circulations across latitudes that are distinct between decadal-scale internal variability and the response to GHG forcing. In both cases, we find that AMOC and the SPG circulation covary, consistent with what is expected from topographic coupling (Yeager, 2015). However, it is less clear how changes in overturning

and gyre circulations in the Nordic Seas are related to circulation anomalies further south. One possibility is that ocean heat content anomalies in the mid-latitudes, originating from AMOC variability, propagate northward (Årthun and Eldevik, 2016) and affect circulations in the Nordic Seas via changes in stratification. It is also possible that large-scale wind and buoyancy forcing (e.g., owing to NAO variability) drives simultaneous circulation changes in the mid-latitudes and the Nordic Seas. Our analysis of internal variability, based on on decadal averages, does not distinguish between these scenarios. Under GHG forcing, we find a substantial role for overturning and gyre circulation changes in the Nordic Seas in driving increased OHT into the Arctic, consistent with previous studies (Bitz et al., 2006; Koenigk and Brodeau, 2014; Marshall et al., 2014b). Here too it is unclear whether these changes are driven by local wind and buoyancy anomalies or whether they are a response to changes in stratification arising from anomalous heat converged from further south. These mechanisms thus merit further study.

Our findings suggest that the mechanisms of changes in OHT into the Arctic differ under internal variability and climate forcing. Importantly, the relationship between anomalies in AMOC and OHT'_{70} changes sign between these two cases. Thus, knowledge of AMOC trends alone is insufficient to infer even the sign of trends in OHT into the Arctic, as it matters whether those trends are internally generated or externally forced. Caution should thus be exercised when applying the results of studies linking anomalies in AMOC and OHT_{70} under internal variability (Day et al., 2012; Chylek et al., 2014; Zhang, 2015; Delworth et al., 2016; Li and Knutson, 2017) to predicting how Arctic climate will change in response to anticipated AMOC weakening over the coming decades.

Chapter 2

MECHANISMS OF LOW-FREQUENCY VARIABILITY IN NORTH ATLANTIC OCEAN HEAT TRANSPORT AND AMOC

This chapter is published as: **Oldenburg, D., Wills, R. C. J., Armour, K. C., Thompson, L., and Jackson, L. C. (2021). Mechanisms of Low-Frequency Variability in North Atlantic Ocean Heat Transport and AMOC, Journal of Climate, 34(12), 4733-4755.**

Abstract

Ocean heat transport (OHT) plays a key role in climate and its variability. Here, we identify modes of low-frequency North Atlantic OHT variability by applying a low-frequency component analysis (LFCA) to output from three global climate models. The first low-frequency component (LFC), computed using this method, is an index of OHT variability that maximises the ratio of low-frequency variance (occurring at decadal and longer timescales) to total variance. Lead-lag regressions of atmospheric and ocean variables onto the LFC timeseries illuminate the dominant mechanisms controlling low-frequency OHT variability. Anomalous northwesterly winds from eastern North America over the North Atlantic act to increase upper ocean density in the Labrador Sea region, enhancing deep convection, which later increases OHT via changes in the strength of the Atlantic Meridional Overturning Circulation (AMOC). The strengthened AMOC carries warm, salty water into the subpolar gyre, reducing deep convection and weakening AMOC and OHT. This mechanism, where changes in AMOC and OHT are driven primarily by changes in Labrador Sea deep convection, holds not only in models where the climatological (i.e., time-mean) deep convection is concentrated in the Labrador Sea, but also in models where the climatological deep con-

vection is concentrated in the Greenland-Iceland-Norwegian (GIN) Seas or the Irminger and Iceland Basins. These results suggest that despite recent observational evidence suggesting that the Labrador Sea plays a minor role in driving the climatological AMOC, the Labrador Sea may still play an important role in driving low-frequency variability in AMOC and OHT.

2.1 Introduction

In order to understand low-frequency Atlantic OHT variability, it is important to study the driving mechanisms. Mechanisms of this variability have been widely analyzed using low--pass filtered model output (Dong and Sutton, 2001, 2002, 2003, 2005), where low-frequency variability is defined as variability at decadal and longer timescales. These analyses suggest that AMOC variability controls low-frequency OHT variability. Analyses of different low-frequency AMOC indices, such as the first principal component (PC) of the low-pass filtered MOC or a convective index, all show that density anomalies in high-latitude deep-convection regions precede changes in AMOC on these timescales (Delworth et al., 1993; Danabasoglu et al., 2012b; Tulloch and Marshall, 2012).

Low-frequency variations in AMOC and OHT are closely linked to changes in North Atlantic sea-surface temperatures (SSTs) and sea-level pressure (SLP) (Bjerknes, 1964; Kushnir, 1994), both of which have exhibited substantial decadal and multidecadal variability in the twentieth century (e.g., Bjerknes 1964; Kushnir 1994; Schlesinger and Ramankutty 1994; Knight et al. 2005; Delworth et al. 2007; Ting et al. 2009; Deser et al. 2010). The North Atlantic Oscillation (NAO) appears to play a key role in driving these AMOC and SST fluctuations via surface-buoyancy-flux and wind-stress changes (Eden and Jung, 2001; Mecking et al., 2015; Delworth et al., 2016; Delworth and Zeng, 2016; Kim et al., 2018, 2020). Delworth and Zeng (2016) use a series of model experiments to show that NAO-related anomalous heat fluxes in the subpolar gyre can drive cooling that results in increased upper ocean density in that region, increasing mixed-layer depths and deep convection, resulting in a strengthening of AMOC and the associated OHT. NAO also plays a major role in controlling decadal variability in Labrador Sea Water formation (Langehaug et al., 2012a).

AMOC and its associated OHT are also closely related to the amount of water-mass transformation (WMT) in the high-latitude regions of the North Atlantic (Marsh, 2000; Isachsen et al., 2007; Grist et al., 2009; Josey et al., 2009; Langehaug et al., 2012b). The WMT is the conversion of a parcel from one density class to another via air-sea exchanges or mixing, and is typically described as a density flux. Surface-forced WMT can be estimated from air-sea heat and freshwater fluxes (Walin, 1982; Tziperman, 1986; Speer and Tziperman, 1992). This WMT allows subsequent deepwater formation, as evidenced by the deep mixed layers in many regions of the North Atlantic. In the North Atlantic, WMT occurs when the North Atlantic Current carries subtropical water northward, where it is cooled by air-sea fluxes, thereby becoming more dense and transforming into Subpolar Mode Water, which is the dominant water mass in the eastern subpolar region above the permanent pycnocline (Pérez-Brunius et al., 2004; McCartney and Talley, 1982; Brambilla and Talley, 2008).

Although there is a well-established link between AMOC and high-latitude WMT, there is debate about which high-latitude deep-water formation regions control time-mean AMOC and its variability. Recent observational analyses suggest that the Greenland-Iceland-Norwegian (GIN) Seas play a primary role, rather than the Labrador Sea (Chafik and Rossby, 2019; Lozier et al., 2019; Petit et al., 2020; Zou et al., 2020). Global climate models (GCMs) differ in their representations of which North Atlantic deep convection regions control AMOC, where biases in the deep convection regions are coincident with biases in temperature and salinity relative to observations (Langehaug et al., 2012b; Menary et al., 2015b; Heuze, 2017). Several models from the Coupled Model Intercomparison Project phase 5 (CMIP5, Taylor et al. 2012), such as NCAR's Community Climate System Model version 4 (CCSM4; Gent et al. 2011), show convection primarily occurring in the Labrador Sea (Danabasoglu et al., 2012b; Brodeau and Koenigk, 2016). However, others, such as the Geophysical Fluid Dynamics Laboratory Earth System Model version 2M (GFDL-ESM2M; Dunne et al. 2012, 2013) and the Hadley Centre Global Environment Model version 3.1 (HadGEM3-GC3.1-LL; Kuhlbrodt et al. 2018; Roberts et al. 2019), show deep convection occurring in the GIN Seas, the Irminger and Iceland Basins, and the Labrador Sea. Though there has been much at-

tention paid to which deep convection regions control climatological AMOC, a key question is whether the same regions also control low-frequency variability in AMOC and OHT.

There are two potential limitations of previous analyses of the causes of low-frequency variability in OHT. First, AMOC does not account for all of the low-frequency variability in Atlantic OHT, as it misses contributions from gyre circulation changes in response to surface wind and buoyancy flux anomalies (e.g., Eden and Jung 2001; Drijfhout and Hazeleger 2006; Menary et al. 2015a; Wills et al. 2019a). Thus, methods that composite OHT on AMOC or convective indices may be missing key contributions to low-frequency OHT variability. Second, using a PC analysis of low-pass filtered data results in a loss of temporal resolution, making it difficult to discern lead-lag relationships between variables on timescales less than the filtering period (Cane et al., 2017; Wills et al., 2019a). Here, we instead use a low-frequency component analysis (LFCA) applied directly to OHT. This method separates low-frequency from high-frequency variability based on differences in their latitudinal structure, while still retaining information about the high-frequency variability. LFCA is described in Wills et al. (2018) and has been applied to characterise and understand modes of low-frequency Atlantic and Pacific SST variability (Wills et al., 2019a,b; Årthun et al., 2021). LFCA makes no *a priori* assumptions about which processes drive or contribute to OHT variability. Moreover, because the resulting indices of low-frequency variability are not low-pass filtered, it is possible to discern how high-frequency variations (e.g., in SLP and surface buoyancy fluxes) contribute to OHT variations at longer timescales. It is important to note that this method cannot be used to determine the sensitivity of the OHT and AMOC to changes in, for example, WMT in different deepwater formation regions. Instead, this method allows us to determine where WMT occurs preceding periods of enhanced OHT and AMOC. In other words, it combines an analysis of where the variance in WMT is concentrated with an analysis of where the ocean is sensitive to this variance.

Here, we use LFCA to determine which mechanisms are responsible for the decadal to multidecadal variability of Atlantic OHT. Specifically, we examine the role of AMOC and whether the mechanisms differ between models with different primary locations of climato-

logical (i.e., time-mean) deep convection. We compare three fully-coupled GCMs that span a range of climatological regions of deep convection: CCSM4, in which deep convection is primarily concentrated in the Labrador Sea; GFDL-ESM2M, in which deep convection is primarily concentrated in the Irminger and Iceland Basins; and HadGEM3-GC3.1-LL, in which the deep convection is primarily concentrated in the GIN Seas. Our low-frequency component analysis provides a novel view of the mechanisms of low-frequency AMOC variability, its role in OHT, and its links to WMT variability.

This chapter is organised as follows. In section 2.2.1, we describe the models used in this analysis. In section 2.2.2, we compare and contrast the model climatologies of Atlantic OHT and ocean circulation. In section 2.2.3, we describe the models' climatologies of AMOC in density space. In section 2.2.4, we examine the surface-forced overturning streamfunction and water-mass transformation in each model. In section 2.3, we compare the water-mass transformation computed from model data to the water-mass transformation calculated from observational datasets. In section 2.4, we use low-frequency component analysis and subsequent lead-lag regression analyses to elucidate the mechanisms of low-frequency OHT variability in the three models. In section 2.5, we summarise our results, describe our main conclusions, and make comparisons with the results from other studies.

2.2 Model climatologies

2.2.1 Description of models

We examine the mechanisms of low-frequency Atlantic OHT variability within three coupled atmosphere-ocean GCM simulations: a 1300-year pre-industrial control simulation of CCSM4 (Gent et al., 2011), a 500-year pre-industrial control simulation of GFDL-ESM2M (Dunne et al., 2012, 2013), and a 500-year pre-industrial control simulation of HadGEM3-GC3.1-LL (Kuhlbrodt et al., 2018; Roberts et al., 2019), all of which have ocean-model resolution of $\sim 1^{\circ}$ in the midlatitudes. All three simulations are forced with constant 1850s greenhouse-gas and aerosol levels, with no volcanic eruptions. We chose these three GCMs for several reasons.

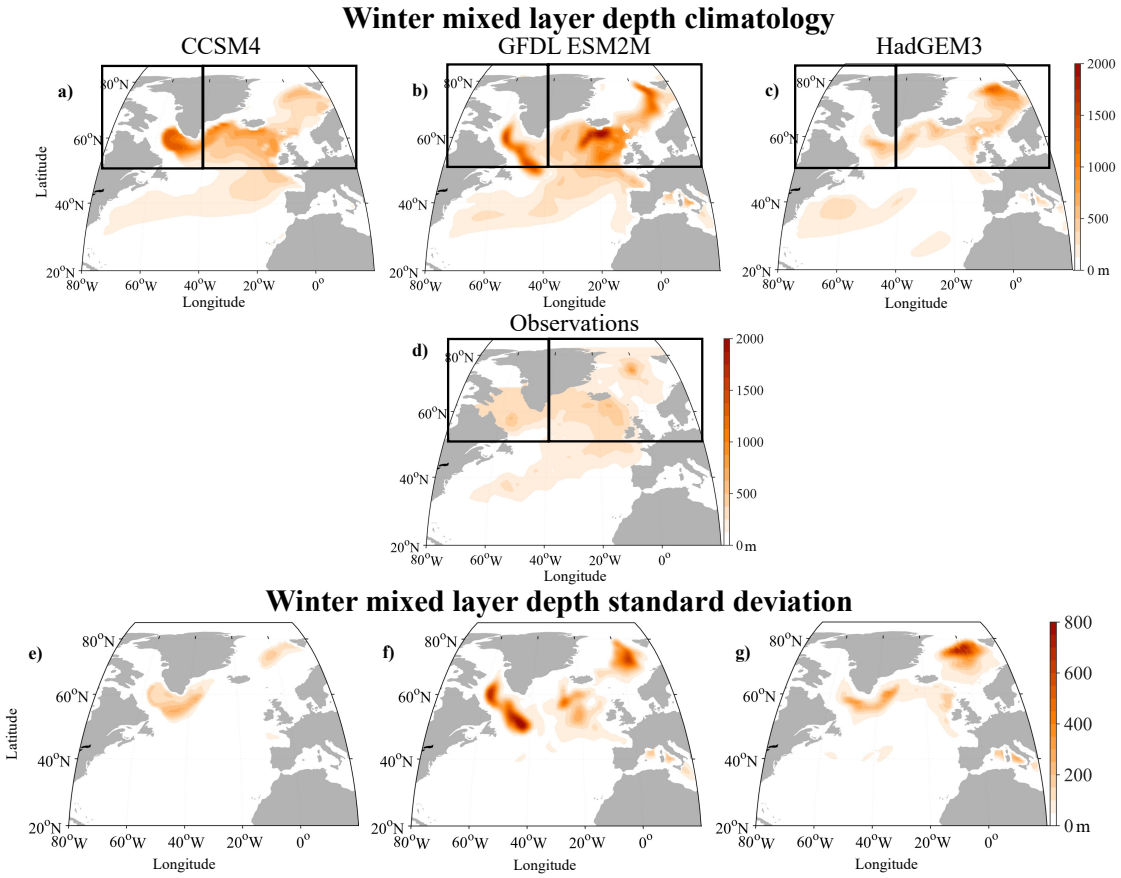

Figure 2.1: Top row: Climatology of winter mixed-layer depth averaged over January, February and March for **a)** CCSM4, **b)** GFDL-ESM2M, **c)** HadGEM3, and **d)** the de Boyer observation based dataset from 1961-2008 (de Boyer Montégut et al., 2004, 2007; Mignot et al., 2007). Bottom row: Standard deviation of 10-year low-pass filtered winter mixed-layer depth for **e)** CCSM4, **f)** GFDL-ESM2M, and **g)** HadGEM3. Although not shown on the map, the Eastern North Atlantic (right) box also includes the area between 20° E and 40° E.

First, AMOC and Atlantic OHT variability have been extensively documented within each GCM (Danabasoglu et al., 2012b,c; Dunne et al., 2012; MacMartin et al., 2013; Msadek et al., 2013; Zhang and Wang, 2013; MacMartin et al., 2016; Kuhlbrodt et al., 2018; Menary et al., 2018; Docquier et al., 2019; Li et al., 2019; Jackson et al., 2020; Koenigk et al., 2020; Roberts et al., 2020). Second, they are comprised of three distinct and commonly-used ocean model components: CCSM4 uses the Parallel Ocean Program version 2 (POP2); GFDL-ESM2M uses the Modular Ocean Model version 4p1 (MOM4p1); and HadGEM3 uses the Nucleus for European Modelling of the Ocean version 3.6 (NEMO3.6). Finally, as noted above, the three models differ substantially in their locations of deep convection: CCSM4 shows deep convection primarily in the Labrador Sea; ESM2M shows deep convection primarily in the Irminger and Iceland Basins; and HadGEM3 shows deep convection primarily in the GIN Seas (Fig. 2.1a, b, c).

These simulations all have small trends in sea-surface temperature, salinity and potential density. North Atlantic SST trends are on the order of $\sim 1 \times 10^{-3}$ °C yr^{-1} or less. North Atlantic sea-surface salinity trends are on the order of $\sim$1-5$\times 10^{-4}$ g kg^{-1} yr^{-1}. North Atlantic sea-surface density trends are on the order of $\sim$1-4$\times 10^{-4}$ kg m^{-3} yr^{-1}. We remove the linear trends from all quantities prior to analysis.

2.2.2 Atlantic OHT and mixed-layer depth

A comparison of the model climatologies of the ocean circulation and density structure along with the OHT gives context for the analysis of the variability. First, we consider the Atlantic OHT. The climatological Atlantic OHT is similar in all three GCMs, with a peak at around 20°N (Fig. 2.2a, b, c), though the magnitude of the peak varies between them, with CCSM4 having the largest peak OHT and HadGEM3 having the smallest. For all of the models, the ocean model grid is rectilinear in the southern part of our analysis domain, but not in the northern part. For CCSM4 and HadGEM3, the true meridional OHT is calculated during run time and is provided as saved monthly fields. However, for GFDL-ESM2M, the OHT on the native grid is provided as saved output. Because the grid in this model is rectilinear

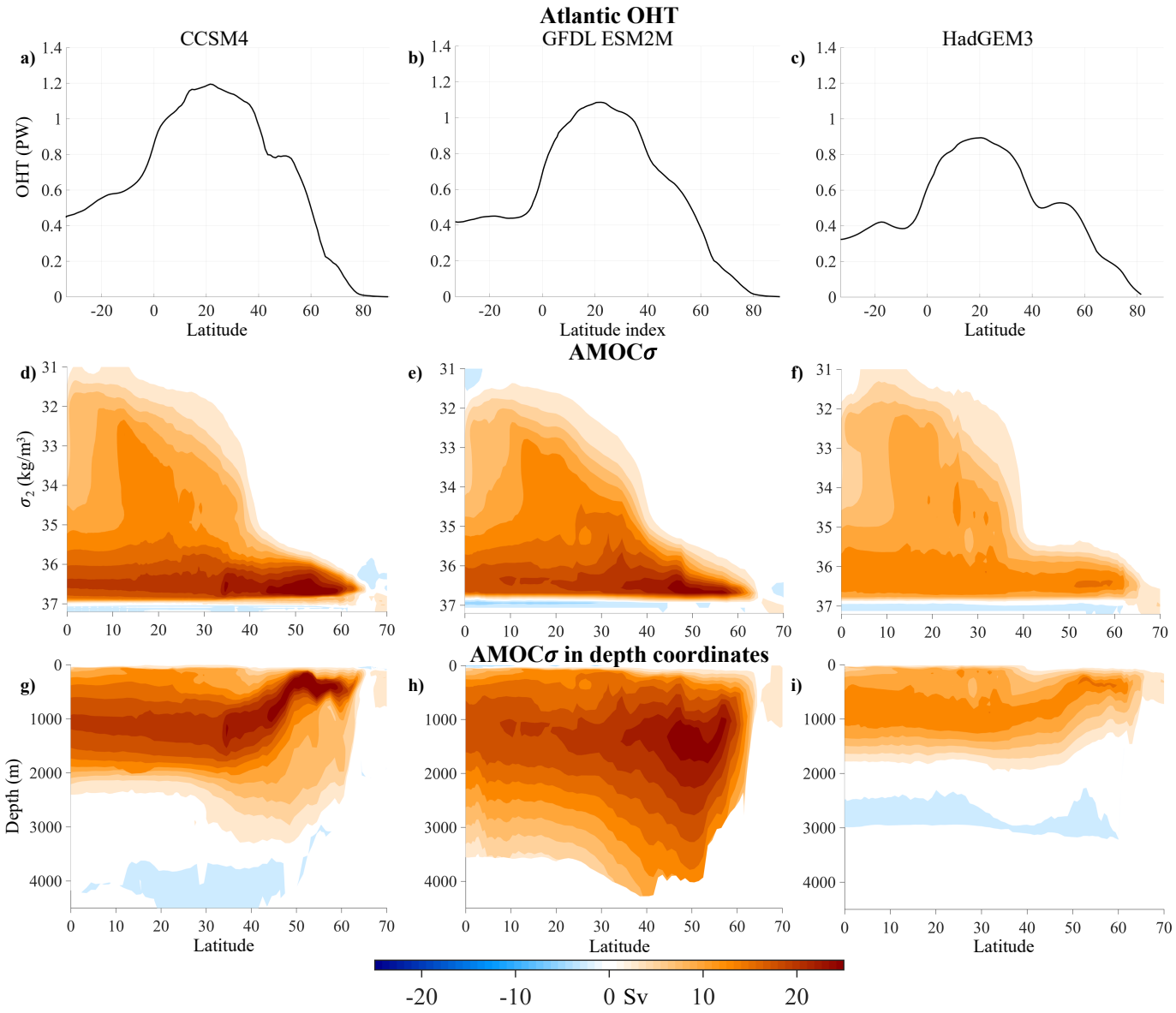

Figure 2.2: Climatological fields in CCSM4 (left column), GFDL-ESM2M (middle column) and HadGEM3 (right column). **a**, **b**, **c)** Atlantic OHT. **d**, **e**, **f)** AMOCσ. **g**, **h**, **i)** AMOCσ remapped to depth coordinates. This mapping is done by calculating the time-mean depth of each isopycnal.

south of 65°N, this gives an accurate estimate throughout most of our study region.

We also analyze the winter mixed-layer depth (MLD) climatologies, which indicate the regions where the deep convection is concentrated in each model. MLDs are calculated during run time based on the vertical structure of density in the upper ocean (Levitus, 1983; Large et al., 1994). The winter MLD climatologies vary considerably between the three GCMs. In CCSM4, the winter mixed layers are deepest in the Labrador Sea, with some deep mixed layers in the Iceland and Irminger Basins as well (Fig. 2.1a). In GFDL-ESM2M, mixed layers are deeper than in CCSM4, and the deepest mixed layers are located in the Iceland and Irminger Basins, though there is a small band of deep mixed layers in the Labrador Sea (Fig. 2.1b). In HadGEM3, mixed layers are the shallowest of all the models, and the deepest mixed layers are located in the GIN Seas (Fig. 2.1c). Given that we are interested in low-frequency variability, we also look at the standard deviation of the 10-year low-pass filtered winter MLD for each model. In CCSM4, the low-frequency variability is almost entirely concentrated in the Labrador Sea, with a small patch of strong variability in the GIN Seas (Fig. 2.1e). Though there is strong climatological deep convection in the Irminger and Iceland Basins in this model, there appears to be very little low-frequency variability there. In GFDL-ESM2M, the variability pattern looks somewhat similar to the climatological MLD pattern, but strong variability is more concentrated in the Labrador Sea than climatological deep mixed layers (Fig. 2.1f). Also, low-frequency variability is overall much stronger than in CCSM4. In HadGEM3, the pattern of low-frequency variability is similar to the climatological MLD pattern, with largest values in the GIN Seas (Fig. 2.1g).

For comparison, we also include winter MLD climatology computed from observation based datasets from 1961-2008 (Fig. 2.1d) (de Boyer Montégut et al., 2004, 2007; Mignot et al., 2007). In this dataset, deep convection seems to be essentially evenly distributed between the Labrador Sea, Irminger and Iceland Basins and the GIN Seas. The observed MLD pattern looks like a combination of the three model climatologies, with somewhat deep mixed layers in all three regions, though the deep mixed layers in the models are not seen in the observations.

2.2.3 AMOC in density space

The meridional overturning streamfunction can be calculated in both density space (AMOCσ) and depth space (AMOCz). In density space, AMOCσ shows a maximum in the subpolar region (Fig. 2.2d-f), because north of 45°N, the steep isopycnals below 200m depth are nearly perpendicular to the isobars. In the subpolar latitudes, there is an extremely large gradient in the overturning streamfunction across a very narrow density range, which represents the North Atlantic Deep Water (NADW), southward deep flow moving along the steep isopycnals. This maximum in overturning is not visible in depth space, because in the subpolar gyre region, the northward transport in the east is compensated by southward transport in the west within the same depth layer (Zhang, 2010). In AMOCz, strong recirculation south of NADW formation regions yields a maximum in the mid-latitudes instead. Thus, AMOCσ is more appropriate for analysing subpolar AMOC variability and also allows a focus on the evolution of water-mass properties as a function of latitude better than AMOCz (Straneo, 2006b; Pickart and Spall, 2007).

AMOCσ in density space (henceforth simply referred to simply as AMOC) is calculated using the following equation:

$$\mathrm{AMOC}(\sigma, y, t) = -\int_{x_W}^{x_E} \int_{-B(x,y)}^{z(x,y,\sigma,t)} v(x, y, z, t) dz dx, \tag{2.1}$$

where σ is the potential density referenced to 2000m, y is the latitude, x is longitude, x_W and x_E are the western and eastern longitudinal limits of the basin, respectively, v is the meridional velocity, z is depth (positive upwards), $B(x, y)$ is the bottom depth, and t is time. For CCSM4, we do this calculation ourselves using monthly model output velocity data. For GFDL-ESM2M and HadGEM3, we use model output of the AMOC.

The relative strength of AMOC and the density class where AMOC reaches its maximum for each model will become relevant when we discuss the regressions of AMOC and the WMT onto the first low-frequency component (LFC) of OHT. The AMOC climatologies for CCSM4 and ESM2M are similar, though ESM2M's is weaker, and its maximum is shifted towards

lower latitudes and slightly lighter densities (Fig. 2.2d, e). CCSM4's AMOC maximum of 29.1 Sv is located at 52.2° N and $\sigma_2 = 36.69$ kg/m^3. ESM2M's AMOC maximum of 27.4 Sv is located at 47.5° N and $\sigma = 36.6$ kg/m^3 (Fig. 2.2d, e). HadGEM3's AMOC maximum of 15.4 Sv, which is much weaker than that in CCSM4 or ESM2M, is located at 52.3° N and $\sigma_2 = 36.5$ kg/m^3 (Fig. 2.2f, i). The vertical structure is substantially different between the models as well (Fig. 2.2g-i). In CCSM4 and HadGEM3, AMOC shoals with latitude and the maximum AMOC is at a shallower depth than in GFDL-ESM2M, where the overturning streamfunction actually deepens with latitude.

2.2.4 Surface-forced water-mass transformation and overturning streamfunction

The surface-forced WMT quantifies the density flux into the ocean due to surface buoyancy forcing (i.e., air-sea heat and freshwater fluxes). It also links changes in surface fluxes and winds in different regions to changes in AMOC (Langehaug et al., 2012b). WMT is calculated from air-sea heat and freshwater fluxes (Tziperman, 1986; Speer and Tziperman, 1992; Langehaug et al., 2012b). Mixing also provides a substantial contribution to WMT (Nurser et al., 1999), often opposing the surface-forced WMT in the North Atlantic (Tandon and Zhao, 2004), though it is generally much weaker than the surface-forced component outside of the tropics. Nurser et al. (1999) used a coupled model and estimated the magnitude of the total mixing component to be about 4 Sv in the subpolar North Atlantic, or about 40% as large as the surface-forced component. Here we neglect this contribution as the publicly available model data do not have sufficient time resolution to examine the mixing component in these models.

Our WMT calculation follows the methods of Speer and Tziperman 1992. The surface density flux $D(x,y,t)$ is calculated via:

$$D(x,y,t) = \frac{\alpha(x,y,t)Q_H(x,y,t)}{c_w} - \beta(x,y,t)S(x,y,t)Q_F(x,y,t), \tag{2.2}$$

where the first and second terms are the heat and freshwater flux components respectively, both in units of kg m^{-2} s^{-1}; $\alpha(x,y,t)$ is the thermal expansion coefficient calculated at each

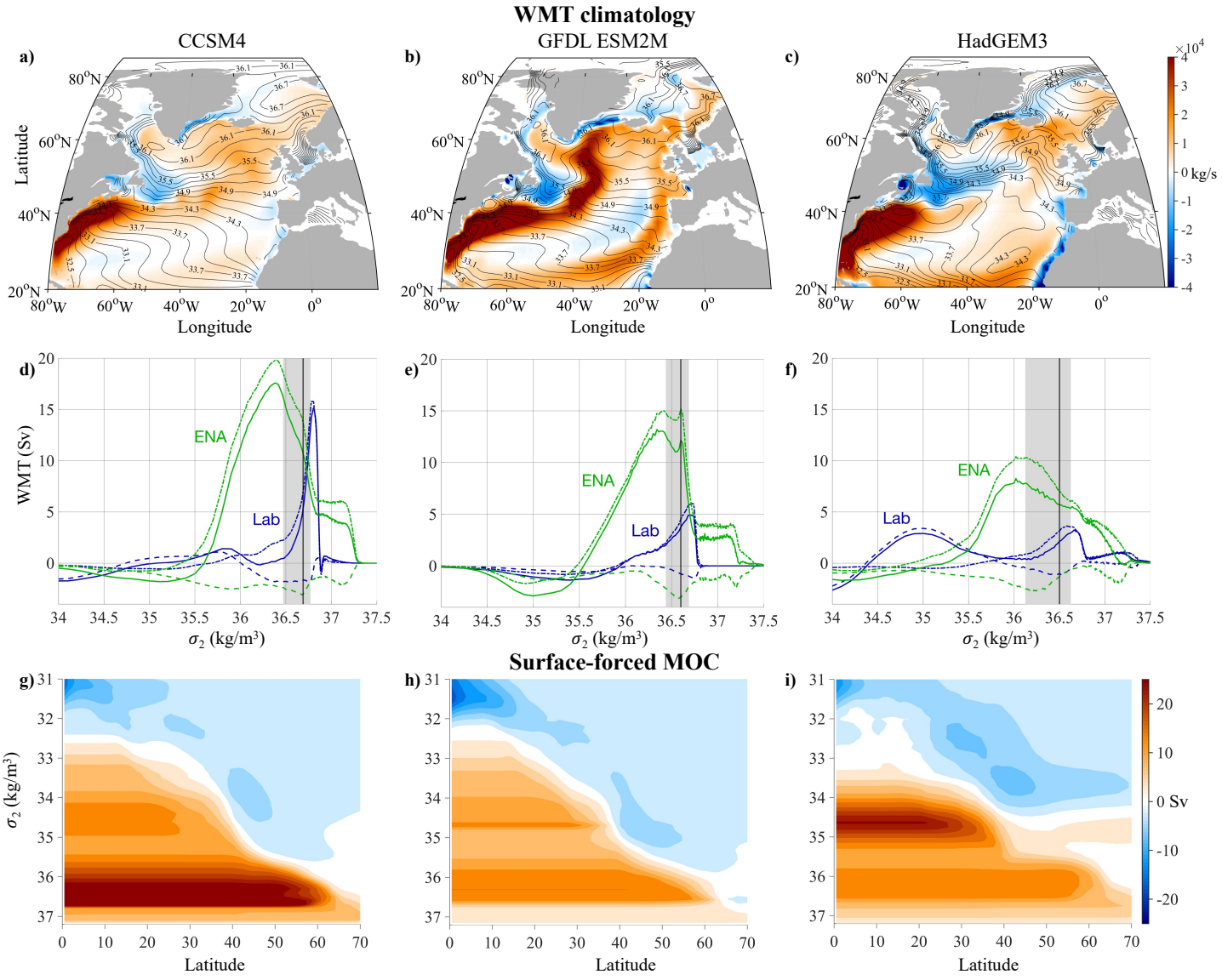

Figure 2.3: Climatological fields in CCSM4 (left column), GFDL-ESM2M (middle column) and HadGEM3 (right column). **a**, **b**, **c)** Total surface density flux $D(x,y,t)$, calculated using Eq. (2.2). **d**, **e**, **f)** Water mass transformation thermal (dot-dash lines), freshwater (dashed lines) and total (solid lines) components in the Labrador Sea and Eastern North Atlantic (ENA) section. The black vertical lines indicate the density where the climatological AMOCσ reaches its maximum in each model. The grey shaded areas represent the density range where AMOCσ is within 10% of its maximum value. **g**, **h**, **i)** Surface-forced overturning streamfunction in density coordinates.

grid point for every month of output data; Q_H is the surface heat flux into the ocean in W m^{-2}; c_w is the specific heat capacity of seawater, assumed to be uniform and constant with a value of 4186 J kg^{-1} K^{-1}; $\beta(x,y,t)$ is the haline contraction coefficient also calculated at each grid point for each time step; S is the surface absolute salinity; and Q_F is the freshwater flux in kg m^{-2} s^{-1}. The surface heat flux includes contributions from latent and sensible heat fluxes, net shortwave and longwave radiation fluxes, and heat fluxes from sea-ice changes. The freshwater flux is the sum of the precipitation, evaporation, runoff, and sea ice formation and melt fluxes. All quantities listed here are either from monthly model output data or calculated using monthly data. $D(x,y,t)$ model climatologies are shown in Fig. 2.3a-c.

The surface-forced WMT at each density is calculated by integrating $D(x,y,t)$ over all surface area in each density bin:

$$F(\sigma) = \frac{1}{\Delta\sigma} \int_{\sigma}^{\sigma+\Delta\sigma} D(x,y,t) dA, \tag{2.3}$$

where $F(\sigma)$ is the surface forced WMT in Sv, $\sigma = \rho - 1000$ is the potential density referenced to 2000m in kg m^{-3}, and $\Delta\sigma$ is the width of each density bin.

We also examine the total $F(\sigma)$ in regions that encompass the Labrador Sea separately from the GIN Seas and Irminger and Iceland Basins (for the location of these regions, see the marked boxes in Fig. 2.1). Here, we include both the GIN Seas and the Iceland and Irminger Basins in one box which we call the Eastern North Atlantic section (ENA) in order to include all surface density fluxes east of the Labrador Sea. We use potential density referenced to 2000 m to allow for easier comparison with AMOCσ, which is typically computed using σ_{2000}. We have also carried out our analysis using σ_0 and this did not substantially change our results.

The partitioning of climatological WMT between the Labrador Sea and the ENA differs substantially among the models (Fig. 2.3d-f). Because models with a greater proportion of WMT in a particular high-latitude deepwater formation region also have deep mixed layers there, it is possible to identify where high-latitude WMT is concentrated by looking at MLD. In CCSM4, because there are large areas with deep mixed layers not only in the Labrador Sea but also in the Iceland and Irminger Basins, both the Labrador Sea and ENA contribute

substantially to the WMT within the density range where AMOC is at or near its maximum (Fig. 2.3d). For both ESM2M and HadGEM3, the ENA dominates the WMT at all density classes that outcrop in the models' deepwater formation regions (i.e., the regions with the deepest mixed layers). In all three models, the thermal WMT component dominates over the haline component. The haline component provides a substantial opposing contribution in both the Labrador Sea and ENA in the density range where AMOC is at its maximum (Fig. 2.3d, e, f). The haline component of WMT is most important in HadGEM3 and least important in GFDL-ESM2M (Fig. 2.3e, f). We compare the WMT computed from the models to what is found in observational datasets in section 2e below.

To understand how much of the structure of AMOC in latitude and density can be attributed to WMT, we compare the full AMOC from Eq. (2.1) against the surface-forced overturning streamfunction (as a function of latitude rather than in specific regions) calculated following Marsh (2000). The surface-forced MOC $F(\sigma, \Theta, t)$ is calculated from the divergence of the surface density flux:

$$F(\sigma, \Theta, t) = -\frac{\partial}{\partial \sigma} \int \int_{\theta > \Theta, \sigma^* > \sigma} D(x, y, t) dA, \tag{2.4}$$

where σ is the surface density; σ^* is a dummy variable representing surface density; Θ is the latitude; θ is a dummy variable representing latitude; $D(x, y, t)$ is the density flux given by Eq. (2.2); t is the time; and A is the surface area.

In both CCSM4 and ESM2M, there is a substantial discrepancy between the climatological surface-forced overturning streamfunction and the climatological full AMOC streamfunction (Figs. 2.3g, h; cf. Fig. 2.2d, e), which can be attributed to mixing. The maximum surface-forced MOC across all densities and all latitudes north of 35°N is equal to 32.9 Sv and 15.0 Sv for CCSM4 and ESM2M, respectively (Fig. 2.3g, h), whereas the maximum AMOC is equal to 29.9 Sv and 27.4 Sv, respectively (Fig. 2.2d, e). In CCSM4, the mixing contribution to overturning is small, about 10% as large as the surface-forced term, and acts to weaken the overturning. In ESM2M, the mixing term is more substantial, about 45% as large as the surface-forced contribution, and acts to strengthen overturning. Substantial discrepancies between the surface-forced MOC and the total AMOC are not uncommon in

models; discrepancies greater than 15 Sv have been found in some models (Grist et al., 2009). The surface-forced AMOC is typically stronger than the total AMOC, but the reverse has been found in at least one model (Grist et al., 2009).

In HadGEM3, the surface-forced overturning streamfunction and full AMOC are similar in magnitude (Figs. 2.2f and 2.3i). The maximum surface-forced MOC across all densities and all latitudes north of 35°N is equal to 15.6 Sv (Fig. 2.3i), and the maximum AMOC is equal to 15.4 Sv (Fig. 2.2f) such that there is a very small mixing contribution in this model, about 1% as large as the surface-forced component. However, mixing weakens the MOC substantially in less dense layers (Figs. 2.2f and 2.3i).

Our results are somewhat similar to what was found in an analysis of a high-resolution model (Xu et al., 2018), which noted a substantial discrepancy between the total and surface-forced overturning streamfunctions.

2.3 Comparison of model water mass transformation to observational datasets

To determine how realistic the representation of surface WMT is in each of the GCMs, we compare with WMT computed from oceanic and atmospheric observation-based datasets. We further consider whether model biases in sea-surface temperature, salinity, or air-sea surface fluxes are responsible for any discrepancies in WMT between the models and observations. To do so, we use monthly surface air-sea heat fluxes over the 26 year period 1984-2009 from the Objectively Analyzed Air-Sea Fluxes dataset (OAFlux; Yu and Weller 2008), monthly SSTs from NOAA Optimum Interpolation Sea Surface Temperature V2 (OISST; Reynolds et al. 2002) and surface salinities from the Hadley Centre's EN4.2.1 (Good and Rayner 2013). Using SST data from EN4.2.1 instead of OISST does not substantially change the results. To estimate freshwater fluxes, we use monthly precipitation, evaporation, snow melt and river runoff data from the ECMWF atmospheric reanalysis (ERA5; Hersbach and Dee 2016). Precipitation and evaporation are taken directly from ERA-5 monthly averaged output, while river runoff is calculated by routing net precipitation over land (from ERA5) to the appropriate ocean grid point using the STN30p River Topology

	Thermal/Labrador	Freshwater/Labrador	Thermal/ENA	Freshwater/ENA
CCSM4/CCSM4	0.94	3.76	0.65	1.86
GFDL-ESM2M/GFDL-ESM2M	0.96	0.54	1.76	0.86
HadGEM3/HadGEM3	0.76	0.45	1.00	0.64
OAFlux/CCSM4	0.88	0.23	0.83	0.17
OAFlux/GFDL-ESM2M	0.82	0.28	1.4	0.23
OAFlux/HadGEM3	0.47	0.25	1.40	0.40
CCSM4/EN4/OISST	1.12	0.61	2.98	0.88
GFDL-ESM2M/EN4/OISST	0.47	0.22	1.58	0.67
HadGEM3/EN4/OISST	0.29	0.21	1.72	1.02

Table 2.1: Absolute value of the bias change between convolved and observation-based WMT components for CCSM4, GFDL-ESM2M and HadGEM3 in the Labrador Sea and ENA regions. Each number represents the absolute value difference between the convolved WMT and the WMT computed from observation-based data averaged over the density range 35 kg/m^3 $< \sigma_2 <$ 37.3 kg/m^3.

dataset (Vörösmarty et al., 2000), as described in Wills and Schneider (2015).

We convolve the monthly observed surface fluxes with SSTs and surface salinities from the equivalent years (1984-2009) of OISST and EN4.2.1 to calculate the WMT and compare that to the WMT in models. We then swap out the observed sea-surface temperature and salinity for those fields taken from each of the models, comparing the resulting WMT with that derived from observations. Similarly, we repeat the calculation using observed sea-surface temperature and salinity fields but with the observed surface fluxes swapped for modeled fluxes. In Table 2.1, we provide the absolute value difference between the convolved WMT and the observation-based WMT averaged over the density range 35 kg/m^3 $< \sigma_2 <$ 37.3 kg/m^3. We choose this density range because it is the range of peak AMOC. Although we use data from pre-industrial control simulations in this analysis, we have also done the same calculations using historical simulation data and found similar results.

Similar to the models, the observation-based WMT shows positive values in the Labrador

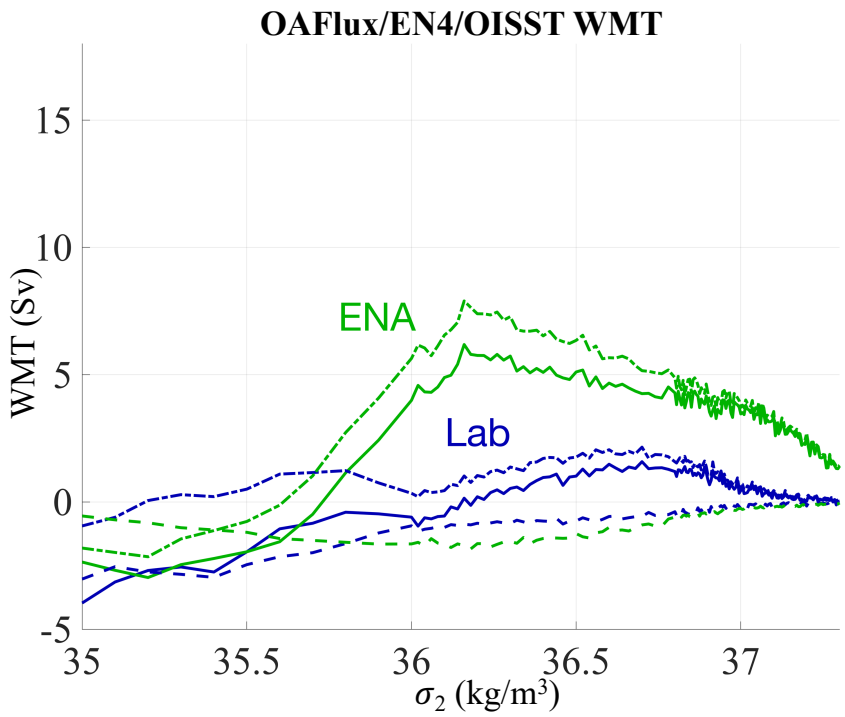

Figure 2.4: Water-mass transformation thermal (dot-dash lines), freshwater (dashed lines) and total (solid lines) components integrated over the Labrador Sea and ENA boxes using OAFlux surface heat fluxes and ERA5 freshwater fluxes convolved with OISST SSTs and EN4.2.1 surface salinities.

Sea as well as the ENA. In both of these regions, strong, sustained winter heat loss to the atmosphere overwhelms any compensating effects from freshwater fluxes (Fig. 2.4). The ENA dominates the WMT at densities above approximately 35.8 kg/m^3. The freshwater components in both regions are negative, with a small but non-negligible magnitude corresponding to approximately 17% of that of the thermal component in the Labrador Sea and 22% in the ENA. The WMT in the two regions occur over a larger range of densities compared to the WMT in models (Fig. 2.4, Fig. 2.3d-f). Of the three models, HadGEM3 is the most similar to observations (cf. Fig. 2.3f).

To examine what features of the models control the differences with observations, we first convolve observation-based sea-surface temperatures and salinities with surface fluxes from the different models. Swapping out the observed surface heat and freshwater fluxes for CCSM4's results in a large increase in the magnitude of the thermal WMT component in the ENA, and a smaller increase in the Labrador Sea (Fig. 2.5d). The magnitude of the freshwater component becomes substantially larger in both regions as well. Swapping out the observed surface heat and freshwater fluxes for ESM2M's yields a result that is closer to the WMT computed from observations than CCSM4 (Fig. 2.5e). Finally, swapping in HadGEM3's surface fluxes results in a WMT that is closest to observations in the Labrador Sea, but slightly worse than GFDL-ESM2M in the ENA (Fig. 2.5f).

Convolving the observed surface fluxes with CCMS4 SST and surface salinities causes the Labrador Sea WMT to be concentrated over a smaller density range and at a higher density class, and also yields substantially stronger thermal WMT in the ENA (Fig. 2.5a). Swapping out the observed SSTs and salinities for ESM2M's causes both the Labrador Sea and ENA WMT to be concentrated over smaller density ranges, with large, narrower peaks at $\sigma_2 = 36.6$ and $\sigma_2 = 36.7$ respectively. This ENA WMT is less similar to observations than CCSM4 (Fig. 2.5b). In the Labrador Sea, the result is not substantially closer or further from observations (Fig. 2.5b). Swapping out the observed SSTs and salinities for HadGEM3's in the Labrador Sea gives a result that is the most similar to what is found when using observational data (Fig. 2.5c), In the ENA, HadGEM3 performs worse than CCSM4 when averaged over the

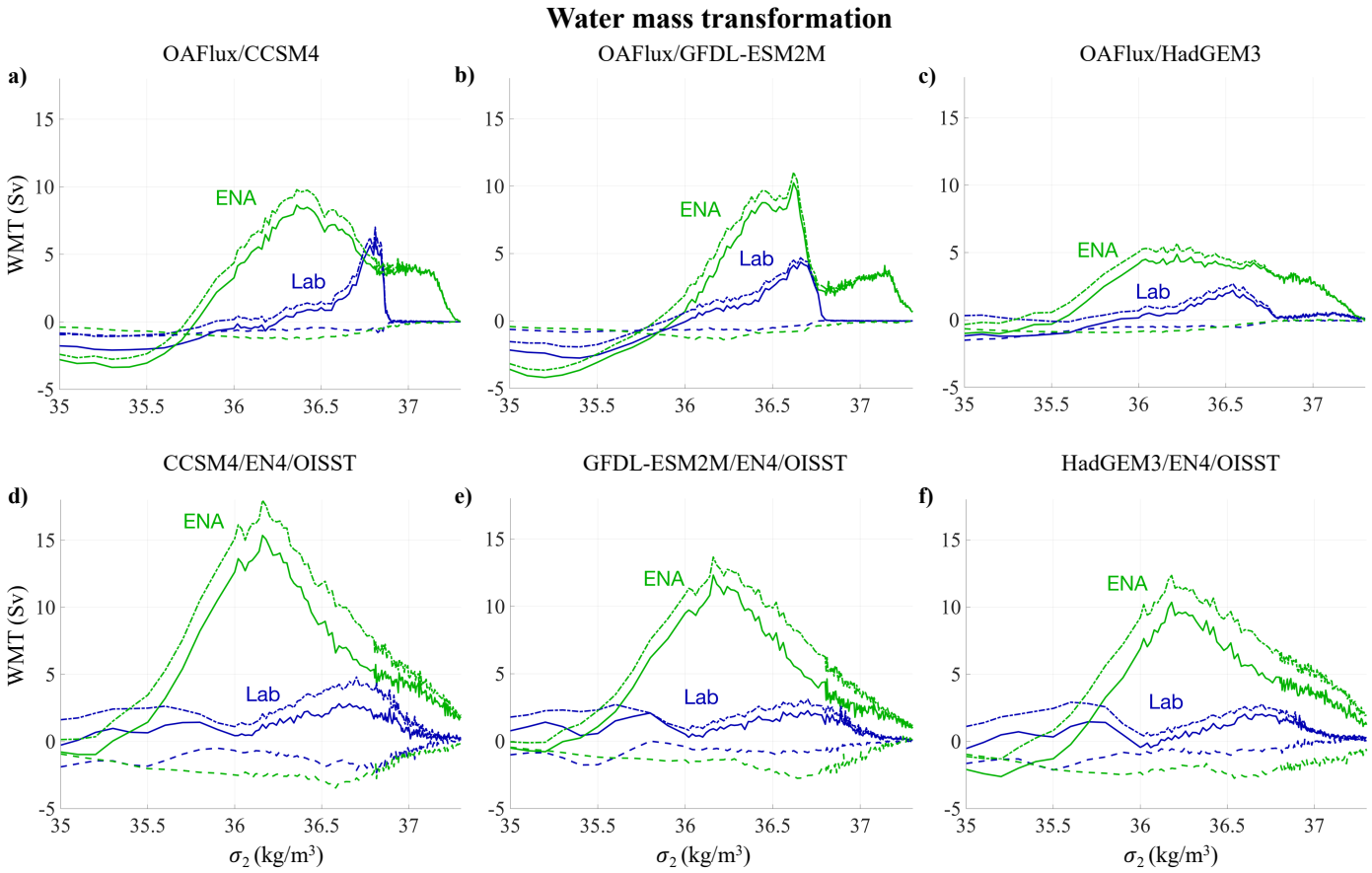

Figure 2.5: Water-mass transformation thermal (dot-dash lines), freshwater (dashed lines) and total (solid lines) components integrated over the Labrador Sea and ENA boxes. Top row: WMT calculated using OAFlux surface heat fluxes and ERA5 freshwater fluxes convolved with sea-surface temperatures and salinities from **a)** CCSM4, **b)** GFDL-ESM2M, and **c)** HadGEM3. Bottom row: OISST SSTs and EN4.2.1 surface salinities convolved with surface heat and freshwater fluxes from **d)** CCSM4, **e)** GFDL-ESM2M, and **f)** HadGEM3.

entire density range. However, the full pattern actually looks more similar to observations than the other two models (Fig. 2.5c). The freshwater WMT component becomes slightly smaller when using sea-surface temperatures and salinities from models, particularly when using GFDL-ESM2M and HadGEM3 SSTs and salinities.

Based on these results, it appears that in the ENA, biases in surface heat and freshwater fluxes are largely responsible for the discrepancy between WMT calculated from models and from observational data; biases in sea-surface temperatures and salinities play a secondary role. However, in the Labrador Sea, it seems that biases in sea-surface temperatures and salinities are more responsible for the discrepancy. Although HadGEM3 is the most realistic of all the models in both its surface fluxes and surface temperatures and salinities, particularly in the Labrador Sea, it still has substantial biases in surface fluxes relative to observations, especially in the ENA. This will be important to keep in mind when we consider the role of WMT variability in low-frequency OHT variability in these models in the following section.

2.4 Mechanisms of low-frequency OHT variability

To examine the controls on low-frequency OHT variability, we first apply a low-frequency component analysis (LFCA; Wills et al. 2018, 2019a) to Atlantic OHT in all three GCMs. We solve for the low-frequency patterns (LFPs) of the OHT, which are the linear combinations of the leading empirical orthogonal functions (EOFs) that maximize the ratio of low-frequency variance to total variance in their corresponding timeseries (called low-frequency components; LFCs). Low-frequency variance is defined as the variance that remains after the pointwise application of a Lanczos filter with a low-pass cutoff of 10 years. The 10-year low-pass filter is only used in identifying the LFPs, and all information about high-frequency variations in the data is preserved. LFCA is related to a broader class of statistical analyses that identify patterns that maximize the ratio of signal to noise (Allen and Smith, 1997; Venzke et al., 1999; Schneider and Griffies, 1999; Schneider and Held, 2001; Ting et al., 2009). We focus on the first LFP/LFC (Fig. 2.6a-c, g-i), which has the highest ratio of low-frequency variance to total variance and is well separated in this ratio from the second LFP/LFC.

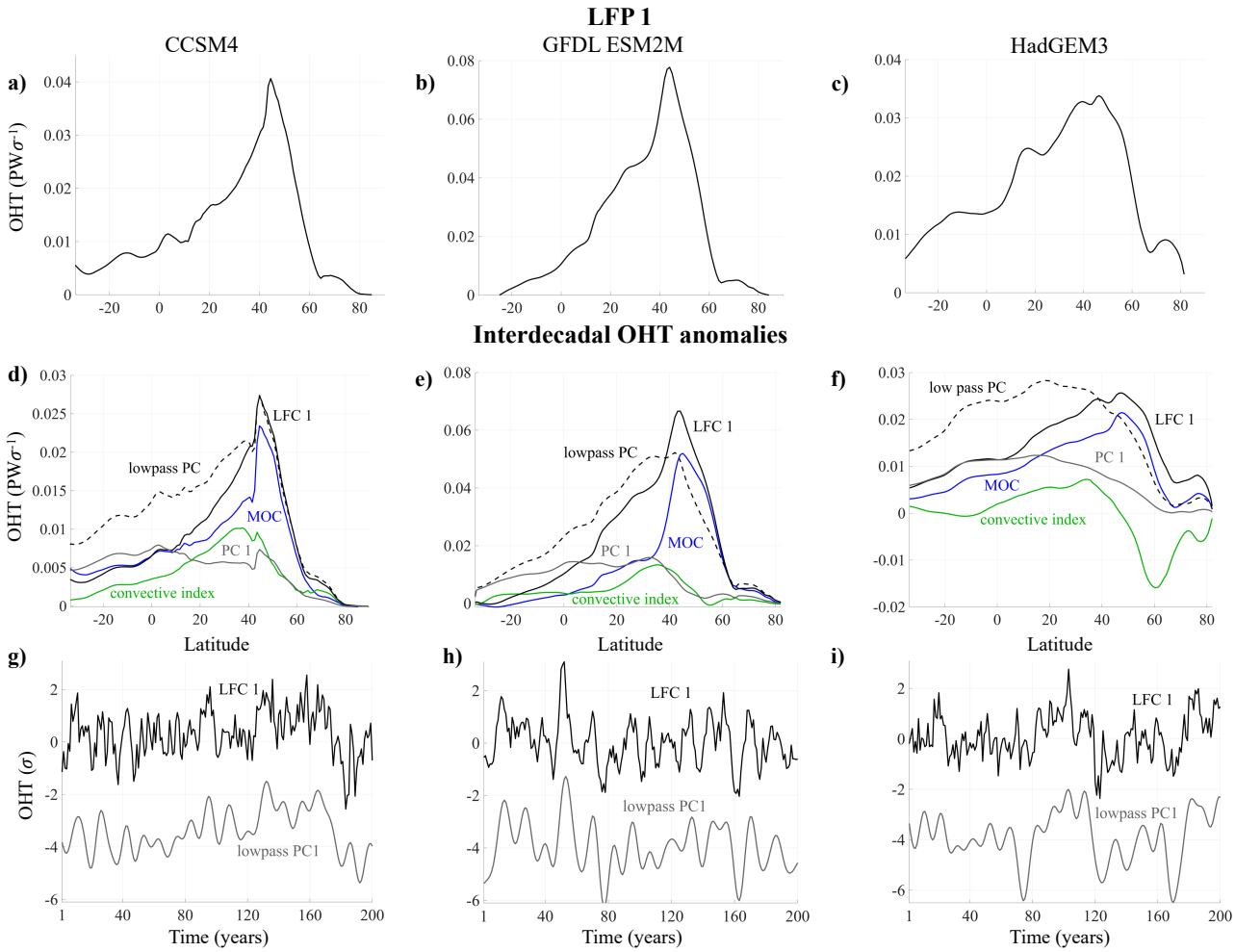

Figure 2.6: Top row: First LFP of Atlantic OHT for **a)** CCSM4, **b)** GFDL-ESM2M and **c)** HadGEM3. Middle row: Regressions of 10-year low-pass filtered Atlantic OHT on different indices in units of PW per standard deviation of the index for **d)** CCSM4, **e)** GFDL-ESM2M and **f)** HadGEM3. The AMOC index is the normalized maximum value of the meridional overturning streamfunction in density coordinates across all densities and latitudes north of 35°N. The convective index is the normalized density anomaly in the models' respective convective regions, excluding grid cells with winter MLD < 500m for CCSM4, winter MLD < 700m for GFDL-ESM2M and winter MLD < 400m for HadGEM3. PC1 represents the first principal component of the OHT. Lowpass PC1 is the first principal component of the 10 year low pass filtered OHT. Bottom row: Time series for both LFC 1 and the lowpass PC1 for **g)** CCSM4, **h)** GFDL-ESM2M and **i)** HadGEM3. Lowpass PC1 time series are shifted downwards by -4 on the y-axis.

This LFP represents the Atlantic OHT anomaly associated with a one standard deviation (1σ) anomaly in the corresponding LFC time series. When calculating the LFPs/LFCs for CCSM4 and HadGEM3, we include the six leading EOFs (92.8 and 93.1% of the total variance, respectively). For GFDL-ESM2M, we include the seven leading EOFs (96.5% of the total variance). The choice of the number of EOFs does not substantially change the results for any of the models.

A traditional approach to studying AMOC variability is to composite on indices such as the AMOC index, defined as the normalized maximum value of the meridional overturning streamfunction in density coordinates across all densities and latitudes north of 35°N, or a convective index (Delworth et al., 1993; Danabasoglu et al., 2012b; Langehaug et al., 2012b; Tulloch and Marshall, 2012; MacMartin et al., 2013), defined as the normalized density anomaly averaged over the models' respective deep convection regions. However, those indices explain a smaller fraction of low-frequency OHT variance than does the first LFC (Fig. 2.6 d-f), and also have a smaller signal-to-noise ratio. Another commonly-used metric, the first principal component of the low-pass filtered OHT, explains a similar amount of low-frequency variance (Fig. 2.6d-f); however, the loss of time resolution makes it difficult to discern lead-lag relationships (Fig. 2.6g-i, Cane et al. 2017; Wills et al. 2019a), precluding a full mechanistic understanding of the drivers of OHT changes, particularly the role of processes occurring on shorter timescales. To determine the mechanisms driving low-frequency OHT variability, we compute lead-lag regressions of anomalies in several atmospheric and ocean fields onto the LFC: upper ocean density, SLP, ocean heat content, winter MLD, the barotropic streamfunction, AMOCσ, and WMT. We calculate the statistical significance at the 95% level for all regressions in each model using 500 phase randomized samples of the LFC (Ebisuzaki, 1997). The salient features of all regressions are statistically significant at the 95% level. Plots of statistical significance are included here for winter MLD (Fig. 2.7) and upper-ocean density (Fig. 2.8).

Although high-frequency variability (in, for example, WMT) doesn't necessarily affect AMOC and OHT, only variability associated with low-frequency changes in AMOC and

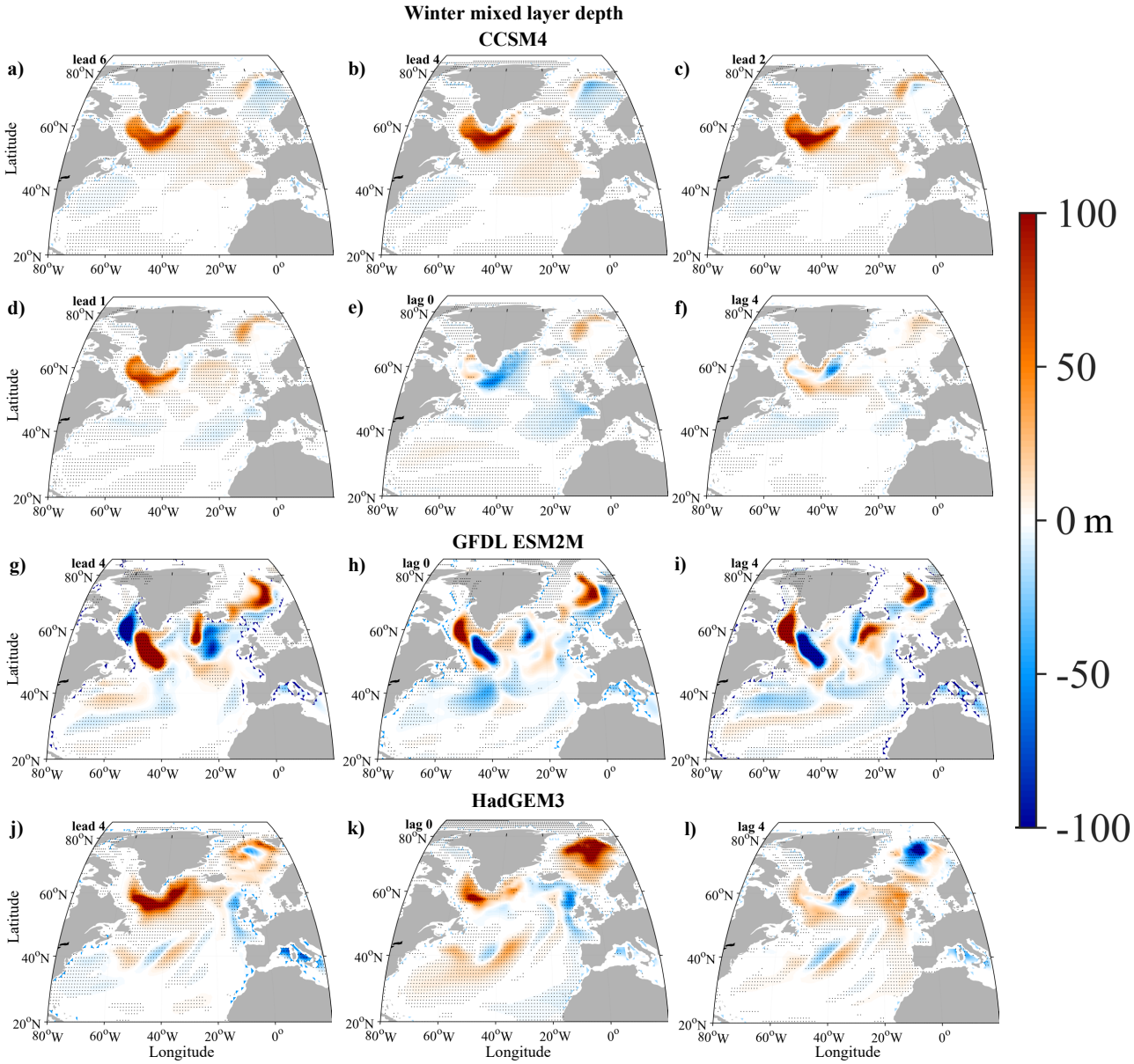

Figure 2.7: Lead-lag regressions of mixed-layer depth averaged over January, February and March onto the first LFC of OHT for **(a-f)** CCSM4, **(g-i)** GFDL-ESM2M and **(j-l)** HadGEM3. Lead times indicate anomalies that lead the LFC, i.e., prior to the maximum OHT. Stipples indicate points where the regressions are statistically significant at the 95% level. Because the LFCs are unitless, the regressions simply have units of m.

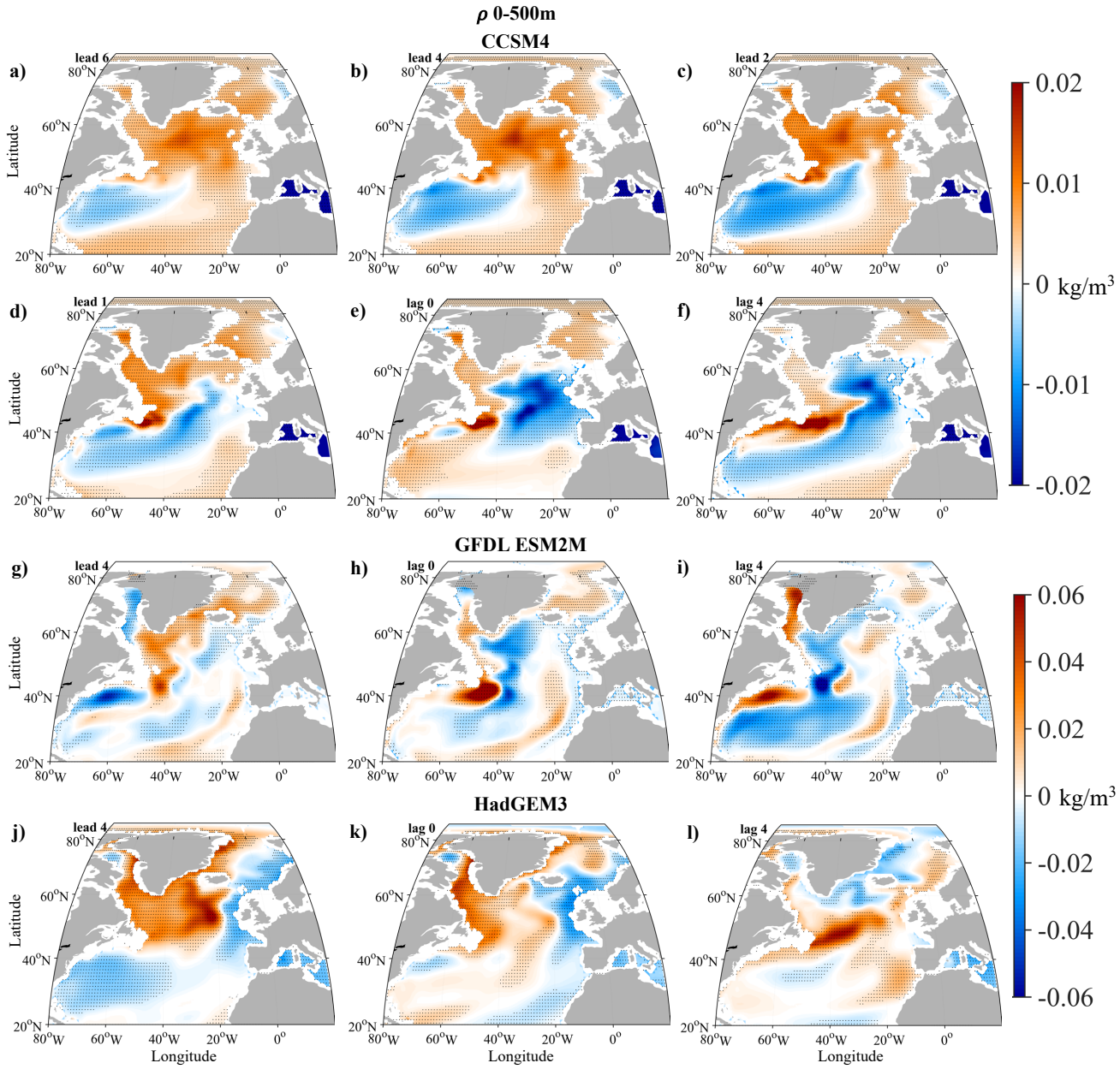

Figure 2.8: Lead-lag regressions of water density averaged over 0-500 m onto the first LFC of OHT for **(a-f)** CCSM4, **(g-i)** GFDL-ESM2M and **(j-l)** HadGEM3. Lead times indicate anomalies that lead the LFC, i.e., prior to the maximum OHT. Stipples indicate points where the regressions are statistically significant at the 95% level. Because the LFCs are unitless, the regressions simply have units of kg/m^3.

OHT would show up in the regressions, because the variables are regressed onto the LFC. Other unrelated high-frequency variability would not be correlated with the LFC because the LFC has very little high-frequency variability.

2.4.1 The pattern of low-frequency Atlantic OHT variability

The first LFPs of CCSM4 and GFDL-ESM2M are similar, i.e., they are both meridionally coherent with a narrow peak in the mid-latitudes around 45°N (Fig. 2.6a, b). The main difference is that GFDL-ESM2M's LFP has a higher magnitude owing to stronger AMOC variability in that model (Yan et al., 2018). For HadGEM3, the magnitude of the first LFP of OHT is smaller than the other two models, with a broader peak in the mid-latitudes (Fig. 2.6c). The ratios of low-frequency variance to total variance are equal to 0.69, 0.89 and 0.76 for CCSM4, GFDL-ESM2M, and HadGEM3, respectively.

To justify our use of the LFCA as opposed to using a more conventional index, we include here a plot of the regressions of the LFC and other indices onto the 10-year low-pass filtered OHT, which are a measure of the low-frequency OHT variance explained by the different indices. The regressions indicate that in all three models, the LFC indeed explains more low-frequency OHT variance than other indices, including the first PC of the non-low-pass filtered OHT, the AMOC index, and the convective index (Fig. 2.6d-f). This indicates that although AMOC plays a major role in low-frequency OHT variability, there are other important processes that contribute to the variability as well. It is also evident that in CCSM4 and ESM2M, the LFP exhibits a similar pattern to the first PC of the low-pass filtered OHT, with the peaks almost exactly aligned, though it explains less low-frequency variance at some latitudes. In all models, the meridional structure of the LFC is more similar to the structure of the OHT regressed onto the AMOC index than the low-pass PC. The LFP creates an index that yields a similar time series to that of the low-pass PC but with all time resolution left intact; hence the LFP captures rapid transitions within low-frequency OHT variability (Fig. 2.6g-i). For HadGEM3, the LFC spatial pattern is different from what is found in the low-pass PC; the peak in the low-pass PC is located further south than that

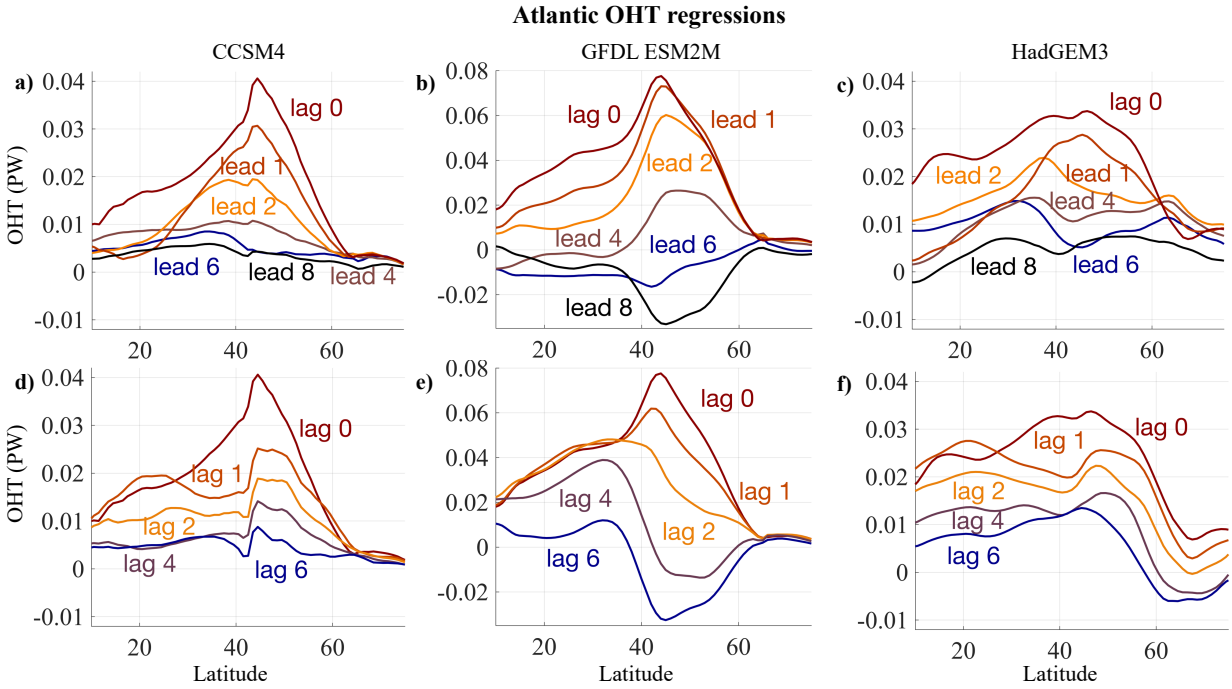

Figure 2.9: Lead-lag regressions of OHT onto the first LFC of OHT for CCSM4 (left column), GFDL-ESM2M (middle column) and HadGEM3 (right column). Lead means LFC 1 lags, i.e., prior to the maximum OHT. **a**, **b**, **c)** Lead times. **d**, **e**, **f)** Lag times. Because the LFCs are unitless, the regressions simply have units of PW.

in the LFP, i.e., at 18.5°N vs. 45°N for the LFC (Fig. 2.6f), possibly because the low-pass PC aliases higher-frequency subtropical OHT variability. In other words, sufficiently strong white noise in tropical and subtropical OHT could still be present in low-pass filtered data and shift the maximum in the EOF towards the tropics.

2.4.2 Mechanisms of low-frequency OHT variability in CCSM4

In order to examine the mechanisms that drive low-frequency OHT variability, we next study lead-lag relationships between the first LFC time series and different oceanic and atmospheric variables. We begin by discussing the results for CCSM4 before comparing to the other two models in the subsequent subsections. Lagged regressions of the OHT onto the LFC time

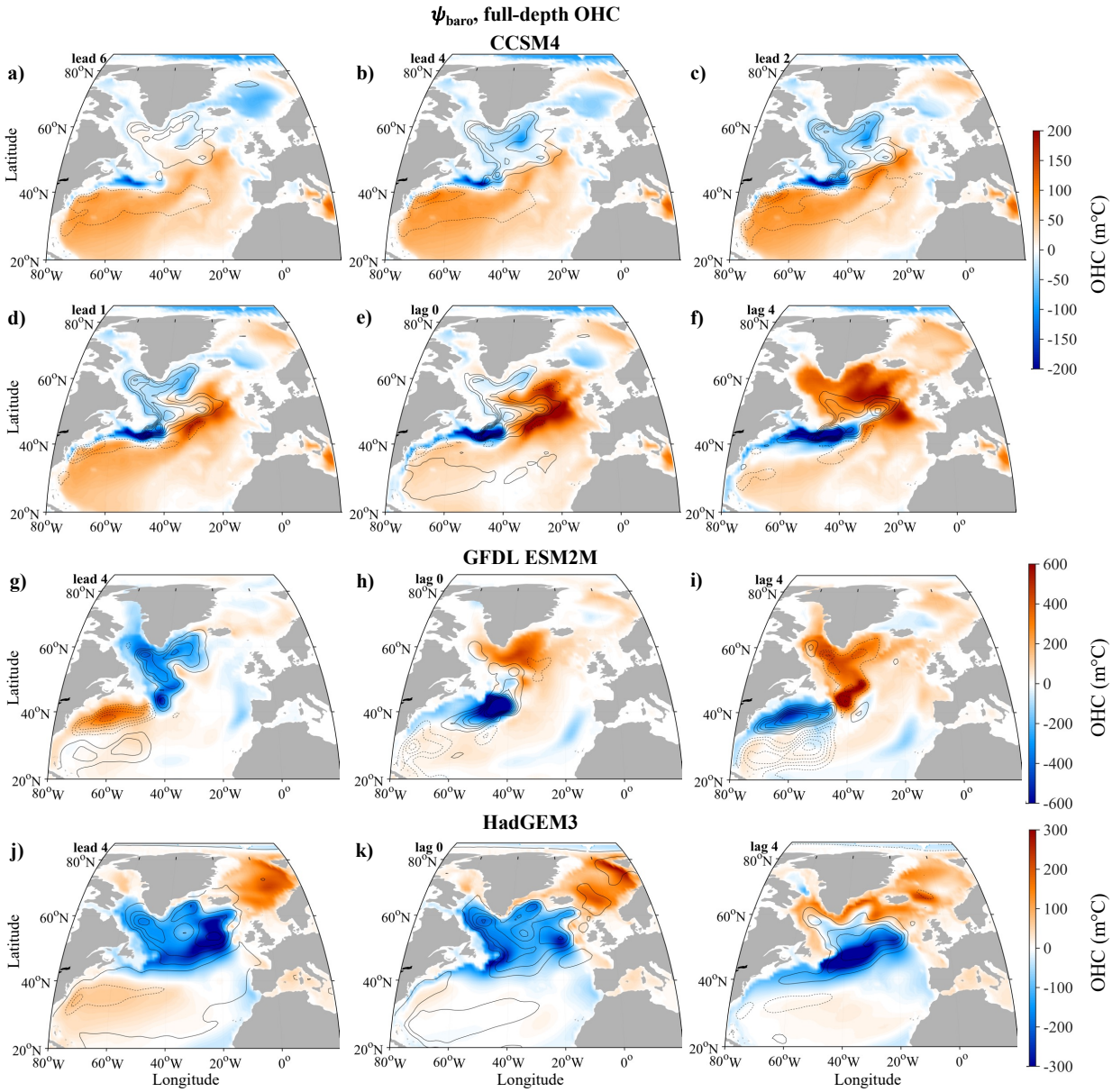

Figure 2.10: Lead-lag regressions of the barotropic streamfunction (contours) and full-depth ocean heat content (colors) onto the first LFC of OHT for **(a-f)** CCSM4, **(g-i)** GFDL-ESM2M and **(j-l)** HadGEM3. Barotropic streamfunction contours are spaced every 0.25 Sv for CCSM4 and HadGEM3 and 0.5 Sv for GFDL-ESM2M. Solid lines indicate cyclonic/positive values, and dashed lines indicate anticyclonic/negative values. Lead times indicate anomalies that lead the LFC, i.e., prior to the maximum OHT. Because the LFCs are unitless, the regressions simply have units of Sv and °C∗m for the barotropic streamfunction and OHC, respectively.

series reveals how the OHT pattern progresses leading up to (Fig. 2.9a) and following (Fig. 2.9d) the time of maximum OHT, as captured by the LFC. These regressions indicate that at lead times (i.e., prior to the time of maximum OHT), the OHT steadily increases in magnitude before reaching its maximum at lag zero with a peak at 45°N. (Fig. 2.9a). At lag times (i.e., after the time of maximum OHT), the OHT steadily decreases in magnitude. The OHT spatial pattern at lag times is different from the one at lead times, as there is a large change in gyre circulation after the time of maximum OHT, causing an abrupt jump in OHT at the boundary between the subtropical and subpolar gyres (cf. Fig. 2.10f).

Lagged regressions between the LFC and winter SLP, as well as the associated wind stress anomalies, reveal the role that atmospheric forcing plays in driving the OHT variability. In the eight years before the time of maximum OHT, there is a persistent SLP pattern associated with anomalous northwesterly winds off eastern North America (Fig. 2.11a-c shows leads up to 6 years). This pattern is similar to the NAO, but the centre of the high-pressure system is northwest of where it appears in the NAO SLP pattern in observations. Since the persistence time scale of SLP anomalies is less than one month (Ambaum and Hoskins, 2002), the persistence of this pattern must be due to memory in the ocean. In the two years before the time of maximum OHT, this pattern becomes more zonal. At the time of maximum OHT, the eastern part of the high-pressure region near western Europe intensifies, while the western part dissipates. This intensification corresponds to Ekman transport that reinforces the low-frequency OHT pattern, which shows up because high-frequency variability is not completely filtered out by the LFCA. This intensification does not occur when the SLP data are low-pass filtered (not shown). Only weak SLP anomalies remain after the maximum OHT (Fig. 2.11f), indicating a weak atmospheric response to this variability. The anomalous winds at lead times cause mixed layers in the Labrador Sea to deepen by inducing anomalous heat loss to the atmosphere and increasing mixing at the surface (Fig. 2.7a-c). The mixed layers reach their deepest two years prior to the maximum OHT, and quickly shoal after lead 1 (Fig. 2.7d-f).

Concurrent with deepening mixed layers in the Labrador Sea, WMT in that region in-

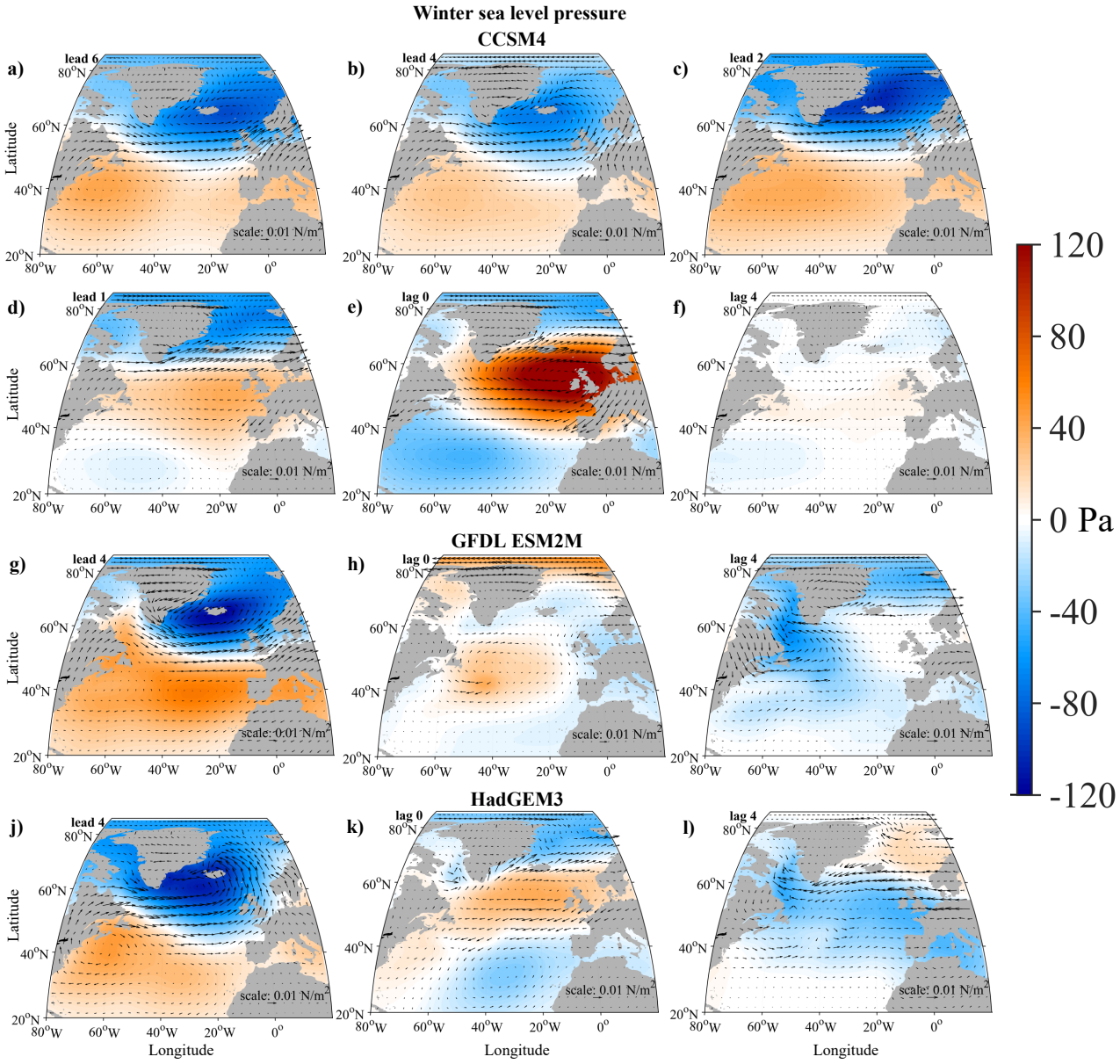

Figure 2.11: Lead-lag regressions of sea-level pressure averaged over January, February and March (colors) and surface wind stress (arrows) onto the first LFC of OHT for **(a-f)** CCSM4, **(g-i)** GFDL-ESM2M and **(j-l)** HadGEM3. Lead times indicate anomalies that lead the LFC, i.e., prior to the maximum OHT. Because the LFCs are unitless, the regressions simply have units of Pa (N/m^2).

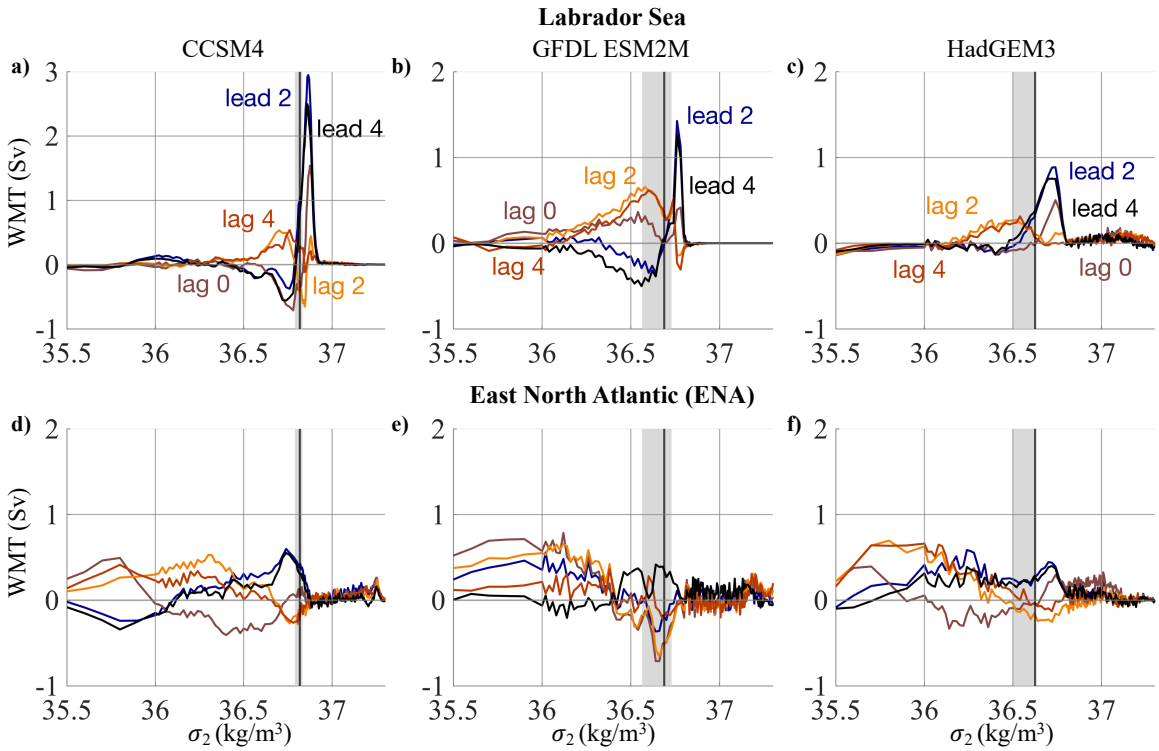

Figure 2.12: Lead-lag regressions of water mass transformation (WMT) onto the first LFC of OHT for CCSM4 (left column), GFDL-ESM2M (middle column) and HadGEM3 (right column). **a, b, c)** WMT summed over the Labrador Sea region. **d, e, f)** WMT summed over the Eastern North Atlantic (ENA) section. The black vertical lines indicate the density where the AMOCσ regression at lag zero reaches its maximum in each model. The grey shaded areas represent the density range where the AMOCσ regression at lag zero is within 20% of its maximum value. The left and right boxes in Fig. 2.1 **a, b, c)** represent what we consider to be the Labrador Sea and Eastern North Atlantic (ENA) in this calculation. Lead means LFC 1 lags, i.e., prior to the maximum OHT. Because the LFCs are unitless, the regressions simply have units of Sv.

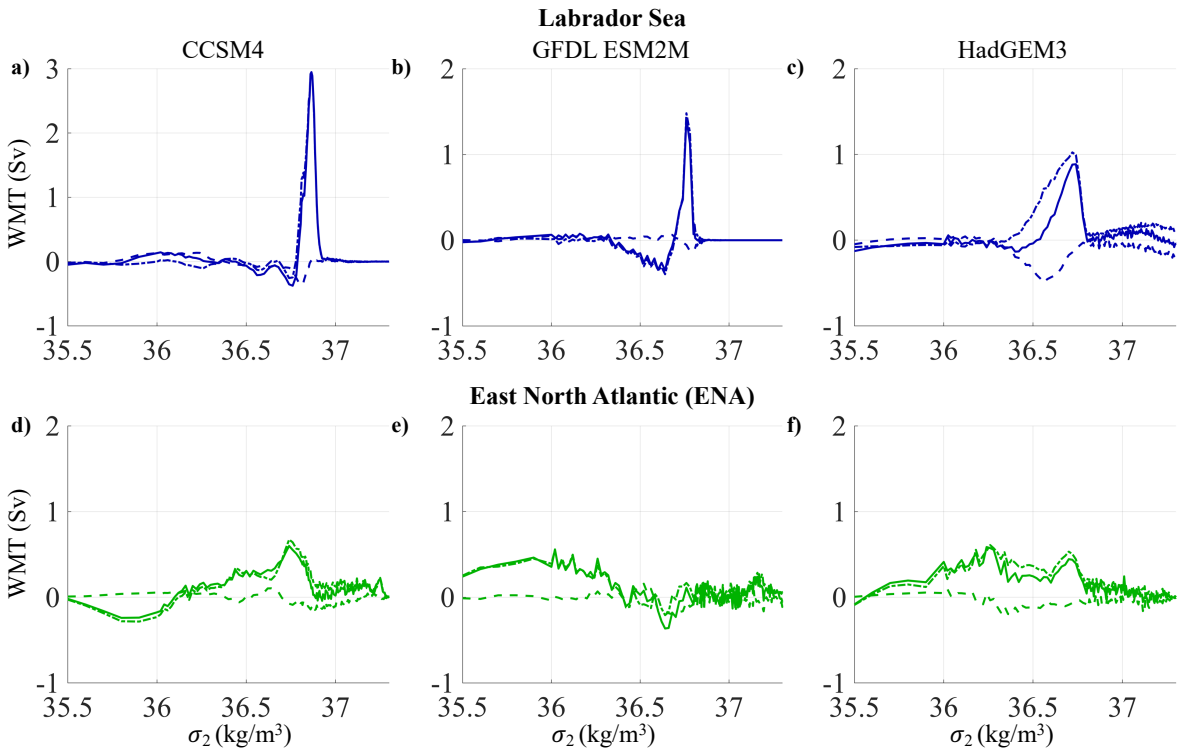

Figure 2.13: 2-year lead-time regressions of thermal (dot-dash lines), freshwater (dashed lines) and total (solid lines) WMT components onto the first LFC of OHT for CCSM4 (left column), GFDL-ESM2M (middle column) and HadGEM3 (right column). **a, b, c)** WMT summed over the Labrador Sea region. **d, e, f)** WMT summed over the Eastern North Atlantic (ENA). The left and right boxes in Fig. 2.1 **a, b, c)** represent what we consider to be the Labrador Sea and ENA in this calculation.

creases, peaking two years before the maximum OHT (Fig. 2.12a). This increase in WMT is centred around $\sigma_2 = 36.87$, where it reaches a maximum of 2.9 Sv. This is at a somewhat higher density than the density where the AMOC anomaly at lag zero reaches its maximum (Fig. 2.12a). There is a relatively small change in WMT in the ENA (Fig. 2.12d), which peaks at $\sigma_2 = 36.74$, with a maximum value of 0.6 Sv. This is a substantially lower density than where the AMOC anomaly reaches its maximum at lag zero, albeit closer to the density of maximum climatological AMOC. The WMT changes are overwhelmingly dominated by heat-flux changes (Fig. 2.13a, d). After lead 2 years, WMT decreases in both regions as the SLP pattern becomes more zonal at lead 1 before weakening after the time of maximum OHT. It is unclear which density range is most important for AMOC variability, and neither the Labrador Sea nor the ENA WMT peaks align exactly with the peak in the AMOC anomaly (Figs. 11a,d). However, the peak in WMT is generally larger in the Labrador Sea than the ENA. Moreover, the Labrador Sea peak occurs at higher densities than the AMOC anomaly, which would be consistent with internal mixing acting to lighten the densest water masses. Altogether, this suggests to us that the Labrador Sea primarily drives OHT and AMOC variability in this model, though the ENA may still make an important contribution.

As WMT increases in the Labrador Sea, near-surface Labrador Sea waters cool and densify (Fig. 2.8a-c), and the increase in WMT and surface density fluxes causes AMOC to strengthen (Fig. 2.14a-e). The anomalous AMOC then carries anomalously warm water northward into the subpolar gyre starting at lead 2 years. Concurrently, the subpolar gyre strengthens (Fig. 2.10a-e). The strengthened gyre circulation then carries this water into the Labrador Sea, where it eliminates the positive density anomalies and hence the deep convection (Fig. 2.8d-f). Meanwhile, a persistent cold, positive density anomaly forms in the Gulf Stream Extension region (Fig. 2.8d-f, Fig. 2.10d-f), suggesting a southward shift of the North Atlantic Current and Gulf Stream. Also, the gyre anomalies become concentrated around the boundary between the subpolar and subtropical gyres (Fig. 2.10f).

Owing to the increase in Labrador Sea surface density fluxes and WMT, AMOC strengthens at lead times in the high latitudes, beginning around nine years before the maximum OHT

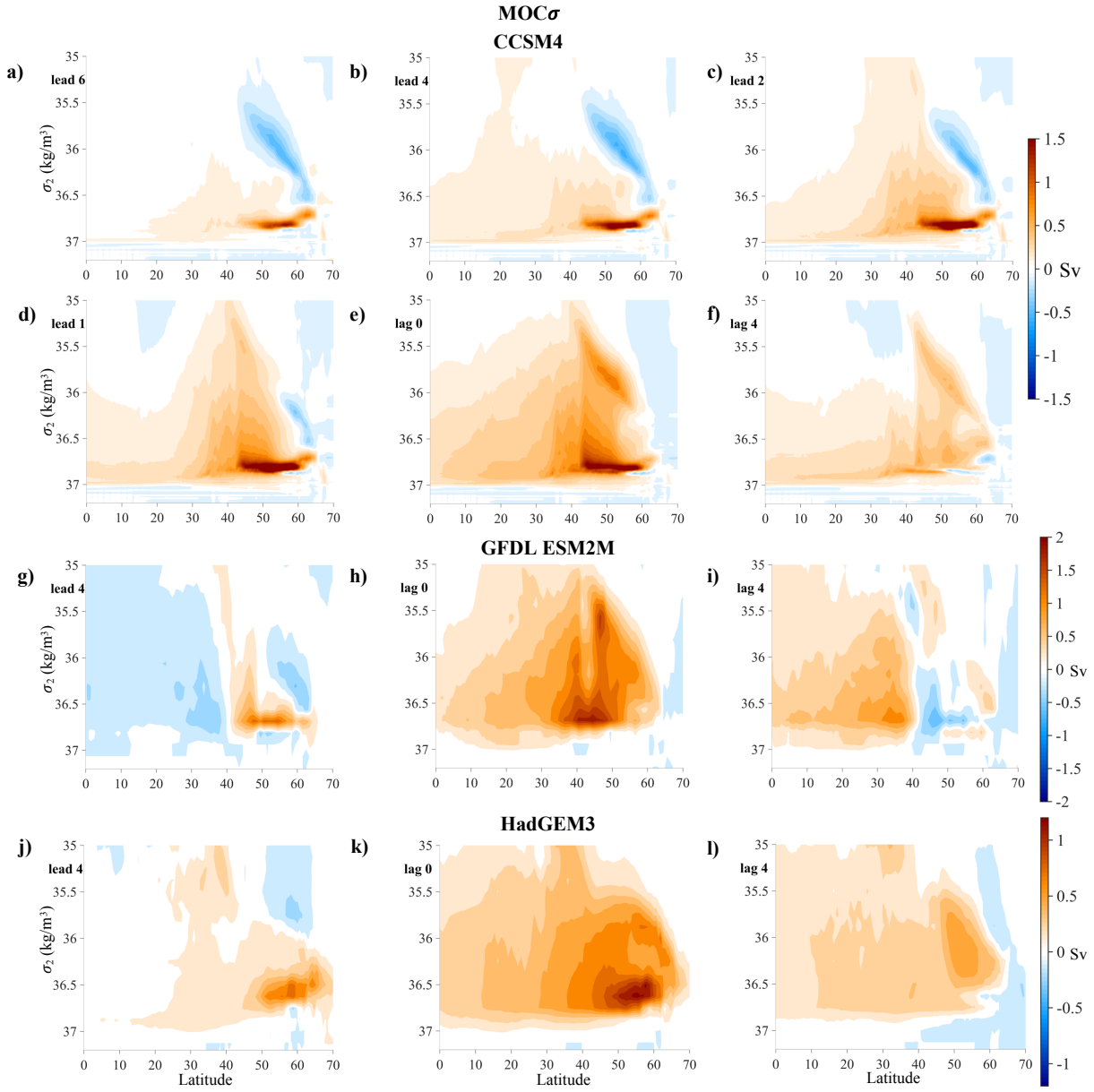

Figure 2.14: Lead-lag regressions of the overturning streamfunction onto the first LFC of OHT for **(a-f)** CCSM4, **(g-i)** GFDL-ESM2M and **(j-l)** HadGEM3. Lead times indicate anomalies that lead the LFC, i.e., prior to the maximum OHT. Because the LFCs are unitless, the regressions simply have units of Sv.

(Fig. 2.14a-e). Given that the gyre circulation projects onto AMOC in density space, part of this signal is likely a result of the concurrent subpolar gyre strengthening (Fig. 2.10a-c). The AMOC anomaly extends throughout the North Atlantic, and is centered around 56° N and $\sigma_2 = 36.82$, where it reaches a maximum of 2.1 Sv (Fig. 2.14e). This is farther north and at a higher density than the maximum climatological AMOC. While the peak WMT anomaly is at a higher density class than the maximum AMOC anomaly, it still coincides with the large, broad AMOC anomaly. Leading up to the time of maximum OHT, this anomaly intensifies and spreads southwards and to lower densities. AMOC reaches its maximum strength when the OHT is at its maximum (i.e., at lag 0). At lag times, AMOC declines as a result of the reduced WMT in the Labrador Sea (Fig. 2.14e, f).

2.4.3 Comparison to mechanisms of low-frequency OHT variability in GFDL-ESM2M

Applying the same analysis to ESM2M, we find largely similar mechanisms of low-frequency OHT variability. As in CCSM4, OHT strengthens leading up to the time of maximum OHT (Fig. 2.9b). At lag times, OHT steadily decreases, as expected, eventually becoming negative at lag 6, indicating periodicity in this model's OHT variability (Fig. 2.9e). This has been reported in previous studies (Dunne et al., 2012) and is evident as a peak in the OHT and AMOC power spectra at 15 years (not shown). This periodicity is not found in either of the other two GCMs examined here.

The SLP pattern at lead times is similar to what is found in CCSM4, with a high pressure system over the Labrador region of Canada driving anomalous northwesterly winds over the Labrador Sea (Fig. 2.11g), though the intense high pressure system found in CCSM4 at lag 0 is weaker and at lower latitudes in ESM2M. Similar to CCSM4, SLP anomalies are weak at lag times (Fig. 2.11i), though ESM2M does show negative SLP anomalies throughout the North Atlantic.

The anomalous northwesterly winds cause mixed layers in the southern Labrador Sea to deepen, though they shoal in the northern portion of the sea (Fig. 2.7g-i). This dipole pattern abruptly flips at lead 1 years, and then the new dipole pattern remains in place until

lag 6. A dipole pattern also appears in the Iceland Basin at lead times, with deeper mixed layers to the west and shallower mixed layers to the east. This pattern flips at lead 1 and remains until lag 6. There is also a dipole pattern in the GIN Seas, which does not flip, unlike the other dipoles.

Even though climatological WMT in GFDL-ESM2M is focused in the Irminger and Iceland Basins, the lagged regressions of WMT onto the first LFC look surprisingly similar to CCSM4, with a much more pronounced peak in the Labrador Sea at lead times than in the ENA box. The WMT anomaly in the Labrador Sea at lead 2 years is centred at $\sigma_2 = 36.76$ with a maximum value of 1.6 Sv. The WMT in the ENA starts out with a positive anomaly at lead 4 years, centered around $\sigma_2 = 36.68$ with a maximum value of 0.3 Sv, before it becomes negative at lead 2 years (Fig. 2.12b, e). The leading ENA WMT anomalies extend to much lower densities than the Labrador Sea WMT anomalies, which have a very narrow peak located at densities substantially higher than the peak in the AMOC anomaly at the time of maximum OHT (Fig. 2.12b, e). Both the Labrador Sea and ENA WMT variability show substantial periodicity, as found with the other variables in this model. The WMT variability is dominated by heat flux changes, with freshwater flux changes playing a minor role (Fig. 2.13b, e).

The anomalous WMT and surface density fluxes over the Labrador Sea drives near-surface cooling and densification in the region at lead times (Fig. 2.8g), albeit less pronounced than in CCSM4. The concurrent increase in WMT and surface density fluxes cause AMOC to strengthen. Similar to CCSM4, the intensified AMOC increases the OHT, which then reduces the density anomalies and high latitude deep convection (Fig. 2.8g-i). Meanwhile, density anomalies propagate southward along the western boundary (Fig. 2.8g-i), a process not seen in either of the other models.

Similar to CCSM4, AMOC begins to strengthen about six years prior to the maximum OHT. However, unlike in CCSM4, as the AMOC anomaly intensifies, it begins to propagate southward, similar what is found for the density anomalies (Fig. 2.14g, h). At lag times, the AMOC anomaly rapidly dissipates and continues to propagate southward, after which it is

replaced by a smaller negative AMOC anomaly at high latitudes (Fig. 2.14i), which we do not find in CCSM4. The AMOC anomaly at the time of maximum OHT is centred around $\sigma_2 = 36.69$ and $\theta = 44.5$°N, with a maximum value of 2 Sv. This is south of and at a higher density class than the maximum climatological AMOC in this model.

Similar to CCSM4, while AMOC strengthens at lead times, both the subpolar and subtropical gyres strengthen and the subpolar gyre cools (Fig. 2.10g). Starting about one year before the maximum OHT, the barotropic streamfunction anomalies begin to congregate around the gyre boundary (Fig. 2.10h). These anomalies continue to propagate along the western boundary.

2.4.4 Comparison to mechanisms of low-frequency OHT variability in HadGEM3

For HadGEM3, OHT gradually strengthens leading up to the time of maximum OHT, maintaining a similar pattern with a very broad peak in the mid-latitudes (Fig. 2.9c). At lag times, the OHT gradually weakens. This process is more gradual than it is in the other models (Fig. 2.9f).

The SLP pattern at lead times is similar to what is found in the other models, with a pronounced high-pressure system over Labrador only occurring between lead 5 and lead 3 (Fig. 2.11j). At lead 1, this NAO-like pattern disappears and at lag zero there is a high pressure system over the eastern subpolar gyre and the Iceland Basin, similar to what is found in CCSM4, albeit much weaker. Immediately after lag zero, the SLP anomalies become small (Fig. 2.11l), similar to what is found in the other two models.

Although the climatological WMT in HadGEM3 primarily occurs in the ENA (Fig. 3e), the WMT regressions at lead times show that much of the WMT variability at higher densities occurs in the Labrador Sea. There is a pronounced increase in WMT in the Labrador Sea at lead times, with a peak at lead 2 years, as in the other models. The anomaly at lead 2 years is centered at $\sigma_2 = 36.74$ with a maximum value of 0.9 Sv (Fig. 2.12c). There is also a peak in the ENA WMT at lead 2 centered around the same density, with a maximum magnitude equal to half of what is found in the Labrador Sea, i.e., 0.44 Sv (Fig. 2.12f). This peak is

much broader than the peak in the Labrador Sea WMT, extending even to densities below $\sigma = 36$. As for the CCSM4 and ESM2M results above, the assessment of which region plays a dominant role in driving AMOC variability depends on which density ranges are considered to be important. The larger peak in WMT in the Labrador Sea, occurring at densities slightly higher than the peak density of AMOC variability (Fig. 2.12c), suggests that the Labrador Sea may play a larger role. However, this feature is not as pronounced as it is in CCSM4 and ESM2M, suggesting that the ENA may play a relatively large role in HadGEM3 compared to those other models. The WMT variability in this model is dominated by heat flux changes, though freshwater fluxes do contribute more than in the other models (Fig. 2.13c, f), providing a small negative contribution to the WMT at lead times.

As seen in the other two GCMs, there is pronounced densification in both the Labrador Sea and the Irminger and Iceland Basins at lead times (Fig. 2.8j), peaking at lead 2 years. This coincides with increased WMT and surface density fluxes in these regions, strengthening AMOC, which then acts to weaken the high-latitude deep convection by carrying anomalously warm water northward. This warm water enters the subpolar gyre from the Iceland and Irminger Basins at the northeastern edge shortly after lag 0 (Fig. 2.8k), and is then propagated westward, reaching the Labrador Sea at lag 4 years (Fig. 2.8l). This warm water does not have as pronounced of a density anomaly as seen in CCSM4. Similar to CCSM4, there is a persistent positive density anomaly in the Gulf Stream Extension region, and in contrast to ESM2M there is no southward propagation of upper ocean density anomalies.

Similar to CCSM4 and GFDL-ESM2M, at lead times, there is a substantial deepening of the mixed layers in the Labrador Sea, peaking at lead 2 years before rapidly shoaling afterwards (Fig. 2.7j, k). However, unlike in the other two models, mixed layers in the GIN Seas deepen at lead times as well, reaching their deepest at lag zero (Fig. 2.7j, k). After the time of maximum OHT, these mixed layers shoal as well (Fig. 2.7l).

As in CCSM4, AMOC strengthens at lead times, reaching a maximum at lag zero, coinciding with the time of maximum OHT (Fig. 2.14j-k). Afterwards, AMOC steadily weakens as a result of the reduced WMT (Fig. 2.14l). The AMOC anomaly at the time of maximum

OHT is centered around $\sigma_2 = 36.63$ and $\theta = 55.6°$N, with a maximum value of 1.3 Sv. This is north of and at a higher density class than the maximum climatological AMOC in this model.

At lead times, while AMOC strengthens, the subpolar gyre also strengthens, and at lag times, the positive anomalies become more concentrated at the boundary between the subpolar and subtropical gyres (Fig. 2.10j-l), as seen in the other models.

2.5 Discussion and Conclusions

Our results suggest a mechanism for low-frequency North Atlantic OHT variability that is consistent across the three distinct GCMs used here: persistent SLP anomalies in the 4-9 years prior to the time of maximum OHT, which are associated with anomalous northwesterly winds off eastern North America that cool and densify the Labrador Sea waters through air-sea heat fluxes, coinciding with an increase in WMT in that region. This increased WMT causes AMOC to strengthen, increasing the OHT as a result. The strengthened AMOC carries anomalous warm water northward into the subpolar gyre, which then carries it into the Labrador Sea, where it shuts down the anomalous deep convection and associated WMT and weakens AMOC and OHT.

Although this mechanism is similar across the models, in GFDL-ESM2M there is pronounced periodicity in the density, AMOC, OHT and water-mass transformation variability. AMOC anomalies also appear to propagate southward in that model, consistent with what was found in Zhang (2010).

Our results suggest that AMOC variability is closely linked to preceding density anomalies in the subpolar gyre and the Labrador Sea, consistent with mechanisms discussed in Tulloch and Marshall (2012) and Kwon and Frankignoul (2014). However, our findings are not in agreement with those of Dong and Sutton (2005), who found a salinity dominated mechanism in HadCM3, where a strengthened North Atlantic Current causes an increase in deep convection in the GIN Seas.

A comparison of WMT with observations indicates that biases in surface heat and fresh-

water fluxes play a much larger role than sea-surface temperatures and salinities in setting the discrepancies between model and observation-based WMT in the ENA, with sea-surface temperature and salinity biases playing a larger role in the Labrador Sea. Of the three models used here, HadGEM3 has the most realistic surface heat fluxes, sea-surface temperatures, and salinities, though HadGEM3 heat fluxes in both the Labrador Sea and ENA are still larger than observational (OAFlux) estimates, and there are still substantial temperature and salinity biases in both regions in this model. HadGEM3's freshwater fluxes are not any more realistic than what is found in the other models. Given that HadGEM3 is the most realistic of the models, particular weight is added to the results of our low-frequency OHT variability analysis of that model.

The lead-lag regression analysis of water mass transformation suggests that regardless of a model's primary location of climatological convection and WMT, the Labrador Sea plays a major role in driving low-frequency AMOC and OHT variability. In CCSM4, climatological convection and WMT is concentrated in the Labrador Sea, and the GIN Seas and Irminger and Iceland Basins play a relatively minor role in driving the AMOC and OHT variability, though this conclusion is dependent on which density range is more important for AMOC. In GFDL-ESM2M, climatological WMT is primarily in the Irminger and Iceland Basins, but the Labrador Sea still plays a substantial role in driving the AMOC variability, albeit with WMT anomalies concentrated at higher densities than the AMOC anomalies at the time of maximum OHT. In HadGEM3, the climatological WMT is mainly in the ENA, yet the Labrador Sea still contributes twice as much as the ENA to the WMT anomalies at higher densities, with ENA WMT anomalies more evenly spread across densities higher and lower than where AMOC reaches its maximum at the time of maximum OHT. While not all of the anomalous surface-forced WMT in the Labrador Sea necessarily translates to anomalous overturning owing to compensation from mixing processes, the robust lead-lag relationship between low-frequency OHT variability and WMT in the Labrador Sea suggests a mechanistic link. By applying the low-frequency component analysis to AMOC in each model instead of OHT, we find that WMT in the Labrador Sea also exhibits a clear lead-lag relationship

with low-frequency AMOC variability (not shown). This analysis does not tell us the sensitivity of AMOC and OHT to changes in WMT in the Labrador Sea and ENA. Instead, it tells us the proportion of WMT variability in the different deepwater formation regions that is linked to low-frequency OHT variability. The fact that in CCSM4, for example, WMT variability in the ENA has only a very weak imprint on OHT does not indicate how sensitive OHT is to changes in WMT in the ENA, because there is very little WMT variability there in the model.

In CCSM4 and ESM2M, which both have warm, salty biases in the Labrador Sea relative to observations, heat fluxes dominate the WMT variability, consistent with what was found by Menary et al. (2015b). Heat fluxes also dominate the WMT variability in HadGEM3, even though this model does not have the same biases in the Labrador Sea. Freshwater fluxes play a more substantial role in the WMT climatology in HadGEM3, although the heat fluxes still dominate the variability.

Recent observations from the Overturning in the Subpolar North Atlantic Program (OSNAP) suggest that the Labrador Sea plays a minor role in driving the climatological overturning in the North Atlantic compared to the GIN Seas (Lozier et al., 2019; Zou et al., 2020). Zou et al. (2020) found that this is a consequence of density compensation in the Labrador Sea, where warm, salty water that enters the Labrador Sea exits as cold, fresh water in the same density class. They also propose that large salinity biases in the Labrador Sea are responsible for the discrepancy between models and observations, as these biases may lead to a temperature dominated density structure, which is in agreement with our results in CCSM4. The OSNAP data set is only 21 months long, and hence it was not possible to discern the mechanisms controlling decadal and multidecadal variability. Menary et al. (2020) show that high-latitude AMOC computed in both medium and low-resolution HadGEM3 agrees well with AMOC computed from OSNAP data. Yet, the Labrador Sea features more predominantly in the low-frequency AMOC and OHT variability in HadGEM3 than would be expected based on its WMT climatology. This suggests that the Labrador Sea may also play an important role in the low-frequency WMT, AMOC, and OHT variability in nature

despite its limited role in setting the WMT and AMOC climatologies.

There are several caveats to our analysis. In this chapter, when we analyze the link between WMT and AMOC, we choose to focus on WMT in the density range where AMOC is near its maximum. However, because we neglect mixing, we could be missing WMT contributions at other density classes which could cause the ENA to be more important. For example, there could be strong mixing in the ENA at lower density classes, which would drive densification of lower density water masses and also contribute to AMOC. There could also be concurrent mixing in the Labrador Sea that cancels out the surface-forced WMT there. Both CCSM4 and ESM2M have substantial temperature and salinity biases in the Labrador Sea (Menary et al., 2015b), which could distort the representation of deep convection and overturning in these models. The low-resolution models used here also likely overestimate Labrador Sea convection because they do not resolve eddies, which play a significant role in Labrador Sea stratification (Straneo, 2006a; Brandt et al., 2007; Garcia-Quintana et al., 2019). Another issue is that Nordic Seas overflow processes, which play an important role in AMOC and occur at relatively small spatial scales (Treguier et al., 2005; Langehaug et al., 2012a), are too weak in many low-resolution ocean models (Bailey et al., 2005). However, CCSM4 includes parameterized overflows, yet still shows similar behavior to what is found in the other two models (Danabasoglu et al., 2012a), which only use model resolved processes. Based on this, it would be valuable to perform a similar analysis in a high-resolution coupled model.

Here, we have found that the Labrador Sea plays a major role in low-frequency variability in water-mass transformation, meridional overturning, and Atlantic OHT in three models with distinct primary climatological deep-water-formation regions. The results suggest that the Labrador Sea may play a larger role in AMOC and OHT variability than what would be expected based on its contribution to climatological WMT. The consensus between the three distinct models studied here, including a model (HadGEM3) which reproduces observed overturning in the Eastern North Atlantic from the OSNAP program, suggests that the mechanisms that control decadal variability of the subpolar North Atlantic in these models

may be representative of what is found in nature.

Chapter 3

AMOC AND WATER MASS TRANSFORMATION IN LOW- AND HIGH-RESOLUTION COUPLED AND REANALYSIS-FORCED OCEAN MODEL SIMULATIONS

Abstract

Recent studies indicate that high-resolution coupled models resolve deepwater formation in the North Atlantic subpolar regions more accurately than low-resolution models due to the resolution of mesoscale ocean eddies. This has important implications for AMOC variability. Here we analyze both a low and high-resolution version of the same coupled model with the goal of determining what sets the relative strength of the water-mass transformation in the different subpolar North Atlantic regions and whether low-frequency variability of AMOC is affected by differences in resolution and differences in climatological water-mass transformation. We find that the high-resolution coupled model more accurately reproduces the water-mass transformation found in a reanalysis-forced high-resolution ocean simulation compared to the low-resolution version. We also find that the low-resolution models, including one forced with the same atmospheric reanalysis data, have larger biases in surface heat fluxes, sea-surface temperatures and salinities compared to the high-resolution model. However, despite these major climatological differences, the mechanisms of low-frequency AMOC variability in the high-resolution model are still largely similar to the low-resolution version. The Labrador Sea still plays a major role in driving the AMOC variability, albeit not as pronounced as in the low-resolution model, and there is a similar leading NAO-like sea-level pressure pattern. However, one major difference is that the high-resolution simulation shows a much more substantial atmospheric response to the AMOC variability, with a negative NAO-like pattern appearing after the strong AMOC. Given that this high-reso-

lution model accurately reproduces reanalysis-forced water-mass transformation, it is likely that these results are representative of the processes in the real climate system.

3.1 Introduction

The link between surface-forced water-mass transformation in the subpolar regions and AMOC has been the subject of many studies, mainly using low resolution ($\sim$1°) global climate models (e.g. Langehaug et al. (2012b)). As mentioned in Chapter 2 (Oldenburg et al., 2021), low-resolution global climate models disagree on which deep-water formation regions dominate AMOC. This is likely owing to temperature and salinity biases in the subpolar regions relative to observations (Langehaug et al., 2012b). In addition, Nordic Seas overflow processes, which are responsible for producing the dense water masses that make up the southward flowing portion of AMOC, and occur at relatively small spatial scales (Treguier et al., 2005; Langehaug et al., 2012a), are too weak in many low-resolution ocean models (Bailey et al., 2005). This results in a deficit in these water masses. Moreover, low-resolution models do not resolve ocean mesoscale eddies, which contribute to water-mass transformation via convection and lateral buoyancy fluxes, particularly in the Labrador Sea (Garcia-Quintana et al., 2019).

A previous ocean resolution sensitivity study of Labrador Sea deep-water formation found that low-resolution simulations likely overestimate deep-water formation and subduction in that region compared to high-resolution ocean simulations (Garcia-Quintana et al., 2019). This is because of the large role that convective eddies play during the restratification phase in the spring and summer months. Mixed-layer depths are also likely too thick in low-resolution models due to the absence of eddies (Garcia-Quintana et al., 2019). Another study found that a higher resolution ocean leads to a more accurate representation of the Atlantic Water inflow through the Iceland-Faroe Ridge (Wekerle et al., 2017). They also found that both the magnitude and the variability of Atlantic Water transport through the Fram Strait are more accurate in a higher resolution model (Wekerle et al., 2017). Another study looked at different combinations of atmospheric and ocean resolutions, and found that an increased

atmospheric resolution results in a substantially weakened AMOCz (by about 5 Sv), and when combined with an eddy-resolving ocean, improves the simulated Gulf Stream separation (Sein et al., 2018). They showed that increased ocean resolution led to a strengthened deep AMOCz cell but a weakened upper cell in the Labrador Sea and Grand Banks. This raises interesting questions, e.g., how does the ocean resolution of a model affect the partitioning of WMT between the different deepwater formation regions? Also, would the mechanisms of low-frequency AMOC and OHT variability found in Chapter 2, which indicate a major role for the Labrador Sea in driving AMOC variability, still hold in a high-resolution model?

In this chapter as a whole, we first compare the mean states of WMT and AMOC in a low and high-resolution coupled model to reanalysis-forced ocean simulations to determine whether the high-resolution model more effectively reproduces what is found in the reanalysis-forced simulations. We then investigate both what parameters determine the mean states of WMT and AMOC in the coupled models with different ocean and atmospheric resolutions and how the variability is affected by the differences in resolution and mean states.

In Part I, we aim to examine how well low and high-resolution coupled model simulations reproduce the climatological water-mass transformation (WMT) and AMOCσ found in ocean simulations forced with atmospheric reanalyses, which we refer to as 'reanalysis-forced' throughout this chapter. We also aim to determine exactly what explains the differences between the WMT from coupled model data and the reanalysis-forced simulations. To do this, we first compute the climatological surface-forced water-mass transformation (WMT) in high and low-resolution versions of a coupled model simulation. Then we compare both of these to high and low-resolution versions of the same ocean model forced with atmospheric reanalysis data.

In Part II, we use LFCA (see Chapter 2) to analyze the mechanisms of low-frequency variability in AMOCσ in the same high and low-resolution coupled models that we used in part 1 (see Description of models, below). The primary goal here is to determine whether the mechanisms of low-frequency OHT and AMOC variability that we described in Chapter 2 still hold in a high-resolution model, i.e. whether the Labrador Sea still plays a major role

in driving multidecadal AMOC variability once mesoscale eddies are resolved.

3.2 Description of models

For the low-resolution coupled model simulation, we use output from a 1800-year pre-industrial control simulation of the 1° Coupled Earth System Model Version 1 (CESM1-LR) (Hurrell, 2013). For the high-resolution coupled model simulation, we use output from a 500-year pre-industrial control simulation of CESM1.3 by the International Laboratory for High-Resolution Earth System Prediction (iHESP) (Chang et al., 2020), which uses an eddy-resolving 0.1° version of the Parallel Ocean Component version 2 (POP2) and a 0.25° version of the Community Atmosphere Model version 5 (CAM5). We henceforth refer to this simulation as CESM1.3-HR. Unlike its low-resolution counterpart, this model does not include the overflow parameterization, while still not fully resolving the overflow processes. At the time of this analysis, output data from the last 190 years of the CESM1.3-HR simulation had not yet been released, and the first 150 years of the simulation are considered to be the spin-up, so in this analysis we include years 150-310.

For the low and high-resolution reanalysis-forced simulations, we use output from 1° and 0.1° POP2 ocean simulations, respectively, both forced with atmospheric reanalysis data from the Japanese 55-year Reanalysis (JRA-55, Kobayashi et al. 2015; Harada et al. 2016; Kim et al. 2021), spanning over years 1958-2018. Henceforth, we refer to these as JRA55-LR and JRA55-HR, respectively. Here, we take JRA55-HR to be our observation-based dataset, and compare the rest of the simulations to it to determine whether increasing the ocean and atmospheric resolution of a coupled model leads to a more accurate representation of the WMT and AMOC. We include JRA55-LR because it provides a more direct comparison with CESM1-LR, and also will illustrate whether a higher ocean resolution is necessary to accurately resolve the WMT and AMOC from observations.

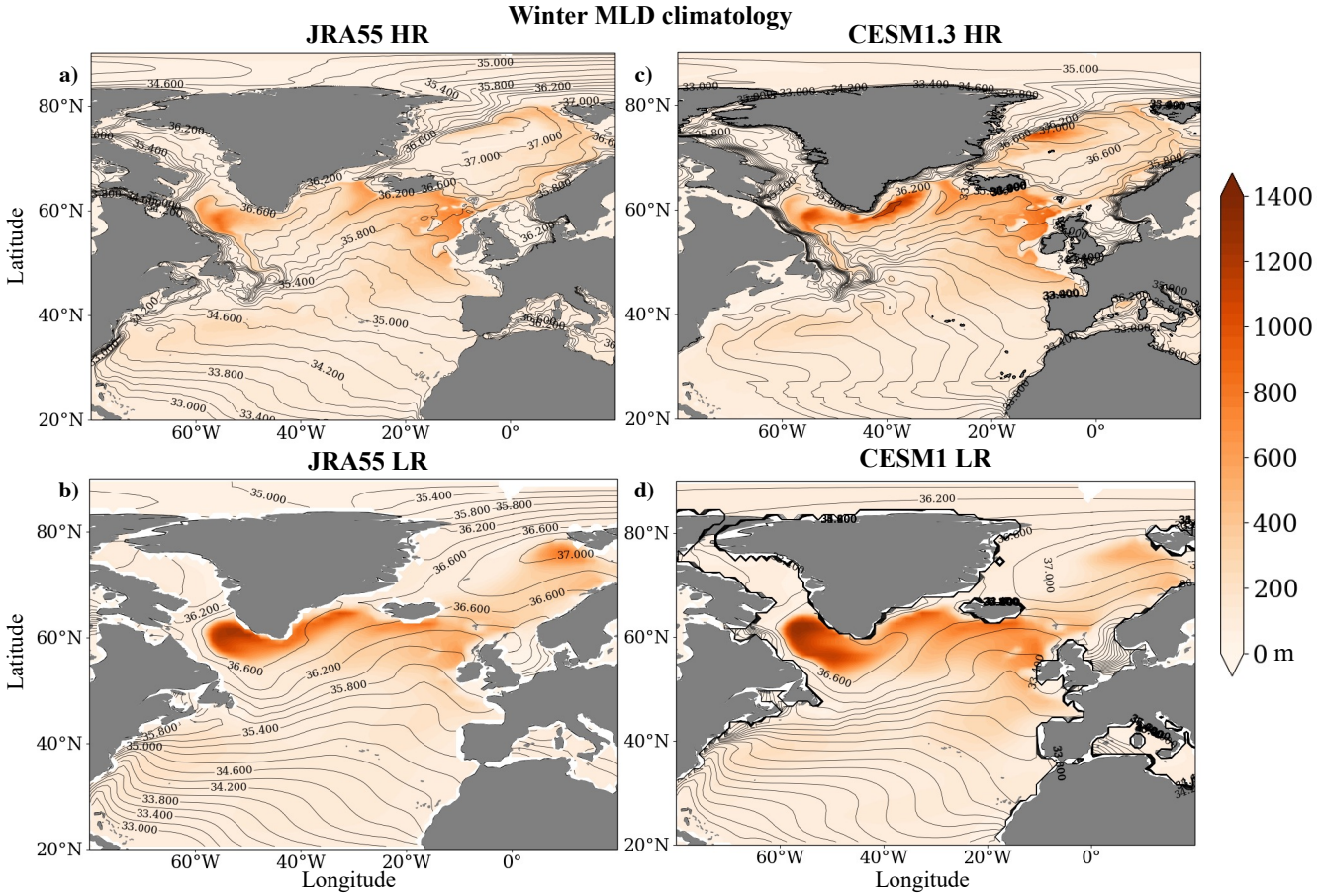

Figure 3.1: Climatological mixed-layer depth (colors) and sea-surface potential density referenced to 2000 m (contours) both averaged over January, February and March in **a)** JRA55-HR, **b)** JRA55-LR, **c)** CESM1.3-HR and **d)** CESM1-LR.

3.3 Part I: Analysis of WMT and AMOC climatology

First, before looking at WMT, it is helpful to analyze the time-mean winter mixed-layer depth (MLD) to determine where the deep convection and deepwater formation occur in the different models, due to its importance for AMOC. In JRA55-HR, deep mixed layers are concentrated mostly in the Labrador Sea and Irminger and Iceland Basins (IIB), with some deep mixed layers in the GIN Seas as well (Fig. 3.1a). In JRA55-LR, the mixed layers overall are deeper, and the deepest mixed layers are concentrated in the Labrador Sea, though there are still deep mixed layers in the IIB and GIN Seas (Fig. 3.1b). In CESM1.3-HR, the MLD patterns look fairly similar to JRA55-HR, but the MLDs are deeper in all of the deepwater formation regions (Fig. 3.1c). In CESM1-LR, the deepest mixed layers are mostly concentrated in the Labrador Sea, even more so than in JRA55-LR, which shows similar overall patterns (Fig. 3.1b, d). It is noteworthy that CESM1.3-HR captures the MLD patterns found in JRA55-HR much better than either of the low-resolution models, despite JRA55-LR being forced with the same atmospheric reanalysis data.

We also look at the AMOCσ climatology to determine how well the coupled simulations (and JRA55-LR) reproduce the AMOC from the reanalysis-forced high-resolution dataset, JRA55-HR. To calculate AMOCσ for each simulation, we use Eq. (2.1) from Chapter 2. In JRA55-HR, the maximum AMOCσ is located at $\sigma_2 = 36.475$ kg m^{-3}, where it reaches 21.8 Sv (Fig. 3.2a). In JRA55-LR, the maximum is located at $\sigma_2 = 36.575$ kg m^{-3} and is equal to 20.7 Sv (Fig. 3.2b). AMOCσ in CESM1.3-HR reaches a maximum of 25.3 Sv at $\sigma_2 = 36.525$ kg m^{-3} (Fig. 3.2c). In CESM1-LR, AMOCσ reaches a maximum of 28.6 Sv at $\sigma_2 = 36.64$ kg m^{-3} (Fig. 3.2d). Hence, JRA55-LR reproduces the AMOC found in JRA55-HR the best of all the other model simulations. Surprisingly, the maximum AMOC is actually lower in JRA55-LR than in JRA55-HR; we would expect a higher resolution simulation to yield a weaker AMOC, as has been found in previous studies (Sein et al., 2018). AMOCσ in CESM1.3-HR is quite a bit closer to JRA55-HR than in CESM1-LR, but is still 3.5 Sv too strong. All of the simulations have AMOC maxima located at higher densities than

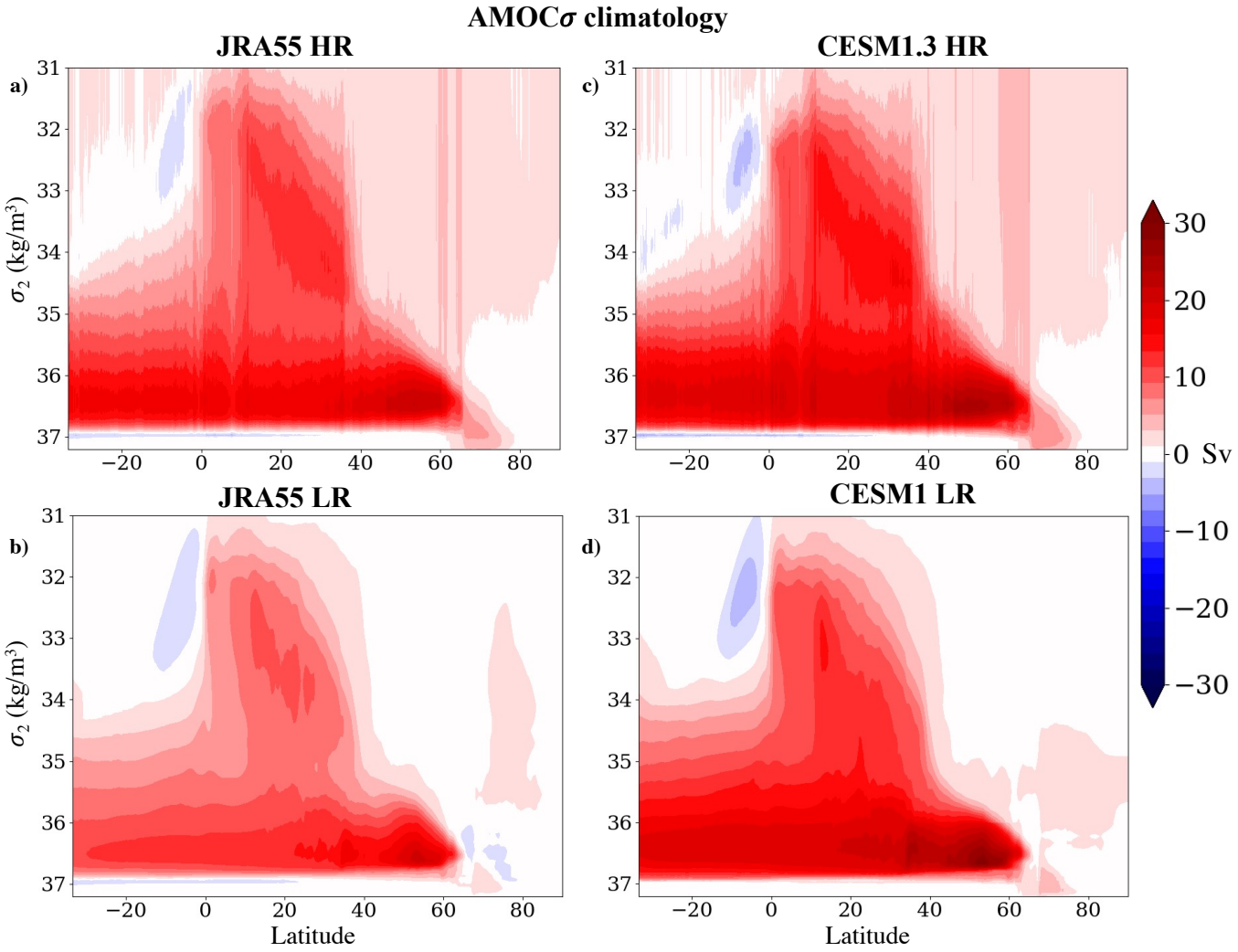

Figure 3.2: Climatological AMOCσ in **a)** JRA55-HR, **b)** JRA55-LR, **c)** CESM1.3-HR and **d)** CESM1-LR.

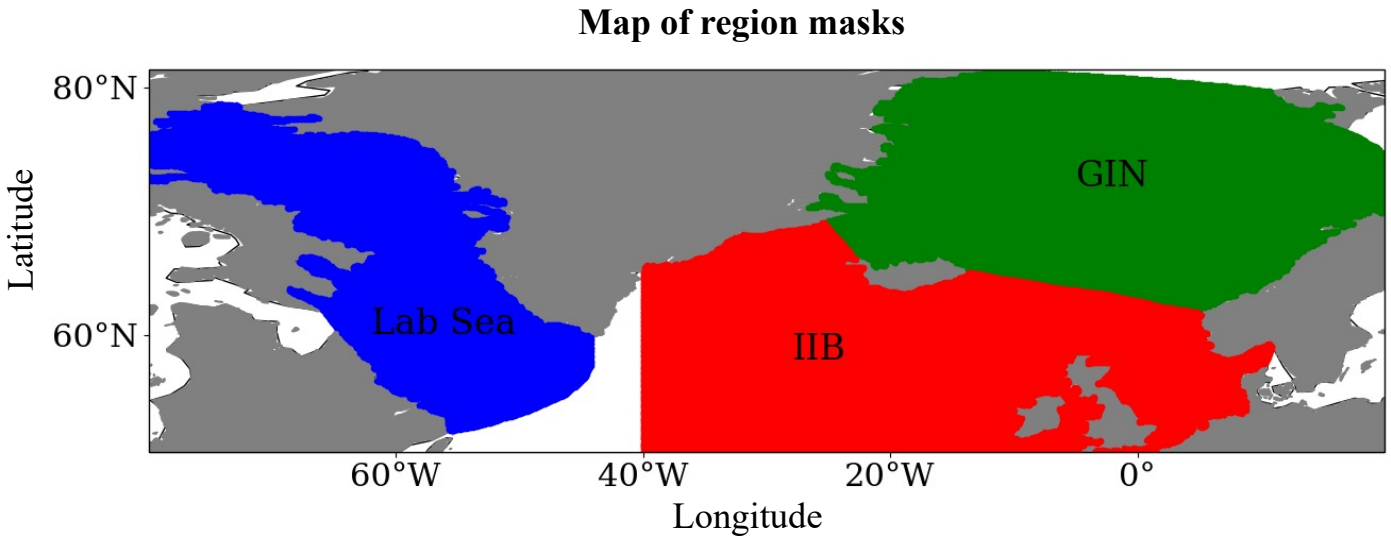

Figure 3.3: Region masks used to calculate the water-mass transformation and surface-forced overturning streamfunction in the Labrador Sea, Irminger and Iceland Basins (IIB) and Greenland-Iceland-Norwegian (GIN) Seas.

JRA55-HR, with CESM1.3-HR being the closest and CESM1-LR being the furthest. These results indicate that although increasing the resolution of the atmosphere and ocean yields an AMOC substantially closer to observations, there are still certain atmospheric processes that are not accurately reproduced in a coupled model.

To calculate the surface-forced WMT, we use Eq. (2.3) from Chapter 2. As in Chapter 2, we neglect the mixing contributions because the model output data do not have sufficient time resolution to calculate them. Here, we compute the WMT separately in the Labrador Sea, Irminger and Iceland Basins (IIB) and GIN Seas using the region masks shown in Fig.

3.3 to determine each region's contribution to the total WMT.

In all four simulations, the thermal WMT component dominates over the haline contribution. Meanwhile, the partitioning of WMT in the different regions varies substantially among the simulations. In JRA55-HR, none of the peaks in WMT in the different regions align with the density of maximum AMOC. However, the IIB contributes the most to the WMT in the density range near where AMOC reaches its maximum (Fig. 3.4a), though both the Labrador Sea and GIN Seas contribute substantially as well. At densities higher than the maximum AMOC, the WMT is dominated by contributions from the Labrador Sea and GIN Seas, with a much narrower peak in the Labrador Sea. Though these densities are further away from the maximum AMOC, they are likely still important for AMOC given that internal mixing acts to reduce the density of the densest water masses. In JRA55-LR, the peaks in the IIB and GIN Seas WMT occur closer to the maximum AMOC, and the IIB still dominates the WMT near the AMOC maximum (Fig. 3.4b). The Labrador Sea peak in WMT is located at about the same density as in JRA55-HR. Also, the peaks in the Labrador Sea and GIN Seas WMT are narrower than they are in JRA55-HR. The WMT curves in CESM1.3-HR look the most similar to JRA55-HR of all the other simulations, with the most notable differences being that the peaks in the IIB and Labrador Sea WMT are substantially larger than in JRA55-HR (Fig. 3.4c). However, the partitioning of the WMT between the different regions is still mostly preserved. In CESM1, on the other hand, the shapes of the WMT curves are very different with much larger peaks in the IIB and the Labrador Sea WMT than in any of the other simulations (Fig. 3.4d). The peak in Labrador Sea WMT is also much narrower than in JRA55-HR and CESM1.3, and looks more similar to JRA55-LR. This seems to indicate that increasing the atmospheric and ocean resolution in a coupled model yields a fairly realistic representation of WMT in the different deepwater formation regions, certainly much more realistic than an equivalent low-resolution coupled model. Also, the major discrepancies between JRA55-LR and JRA55-HR indicate that a higher ocean model resolution is essential in order to provide an accurate representation of WMT, and that getting atmospheric conditions correct is not sufficient.

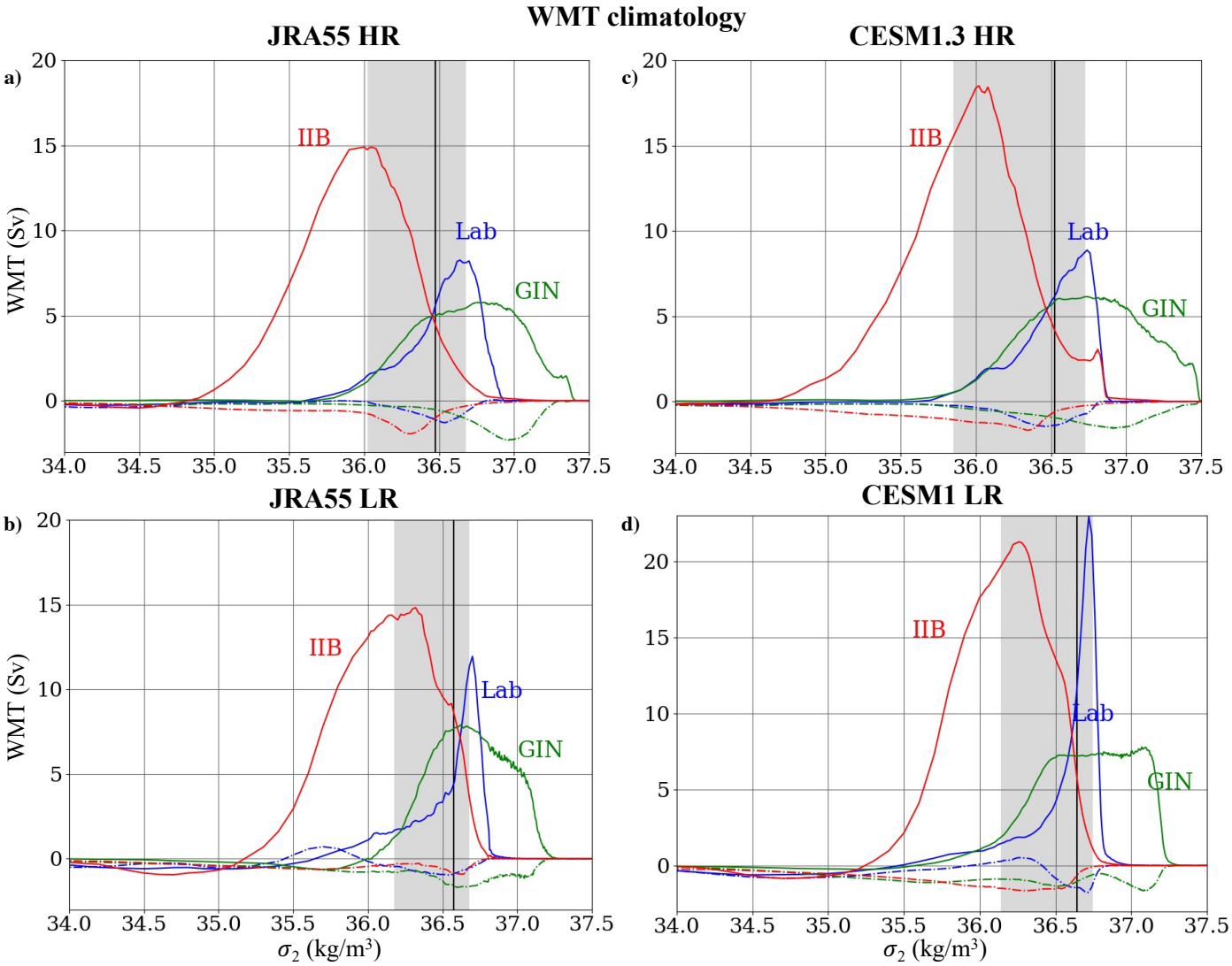

Figure 3.4: Climatological water-mass transformation thermal (solid lines) and freshwater (dashed lines) components in the Labrador Sea, GIN Seas and Irminger and Iceland Basins (IIB) for **a)** JRA55-HR, **b)** JRA55-LR, **c)** CESM1.3-HR and **d)** CESM1-LR. The black vertical lines indicate the density where the climatological AMOCσ reaches its maximum in each model. The grey shaded areas represent the density range where AMOCσ is within 25% of its maximum value.

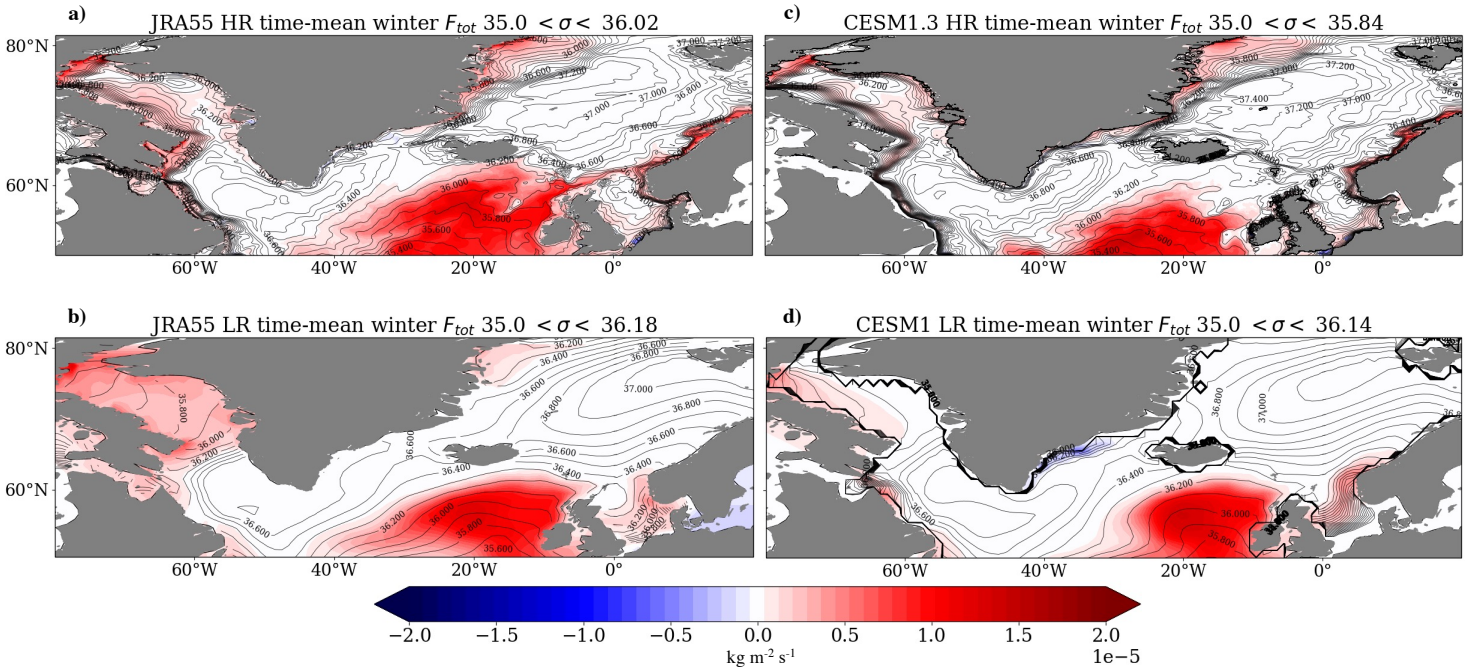

Figure 3.5: Colors: Total climatological winter surface density flux $D(x, y, t)$, calculated using Eq. (2.2) over densities less than the density where AMOC reaches 75% of its maximum. Contours: Time-mean winter sea-surface potential density referenced to 2000 m for **a** JRA55-HR, **b** JRA55-LR, **c)** CESM1.3-HR and **d)** CESM1-LR.

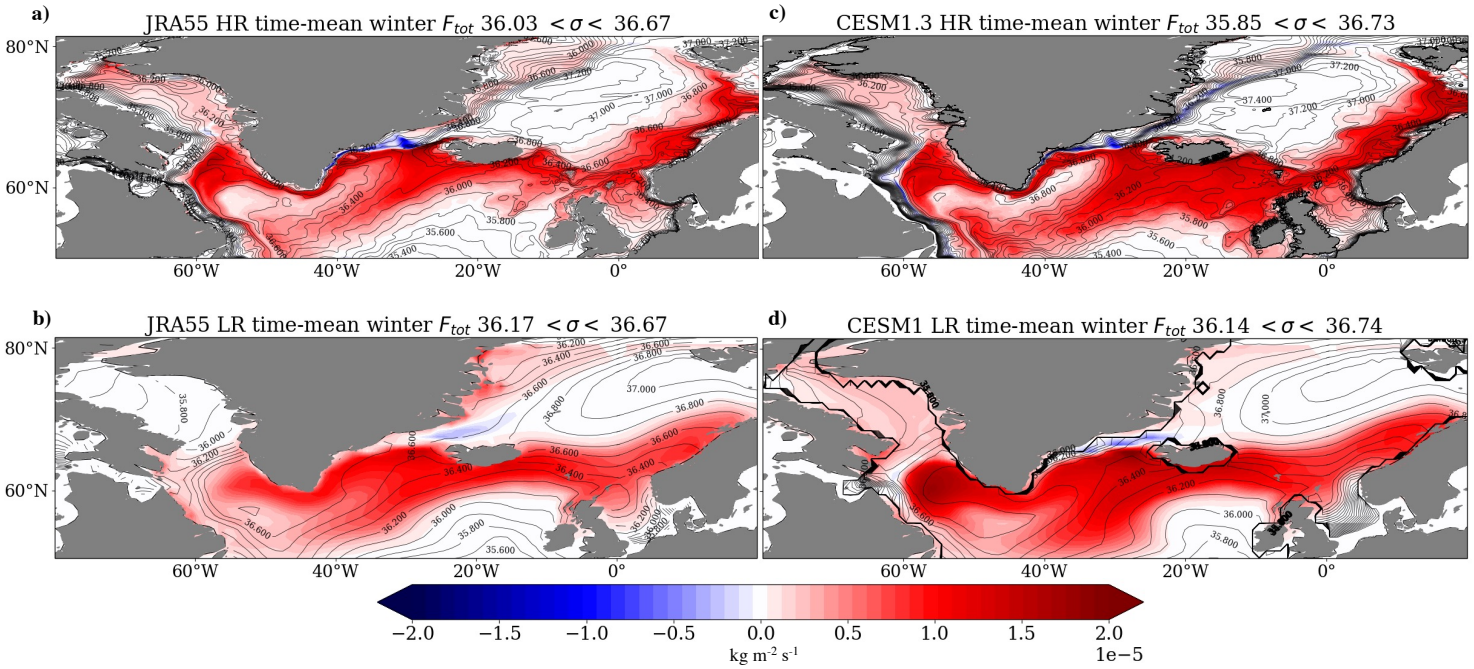

Figure 3.6: Colors: Total climatological winter surface density flux $D(x, y, t)$, calculated using Eq. (2.2) over densities where AMOC is at least 75% of its maximum. Contours: Time-mean winter sea-surface potential density referenced to 2000 m for **a** JRA55-HR, **b** JRA55-LR, **c)** CESM1.3-HR and **d)** CESM1-LR.

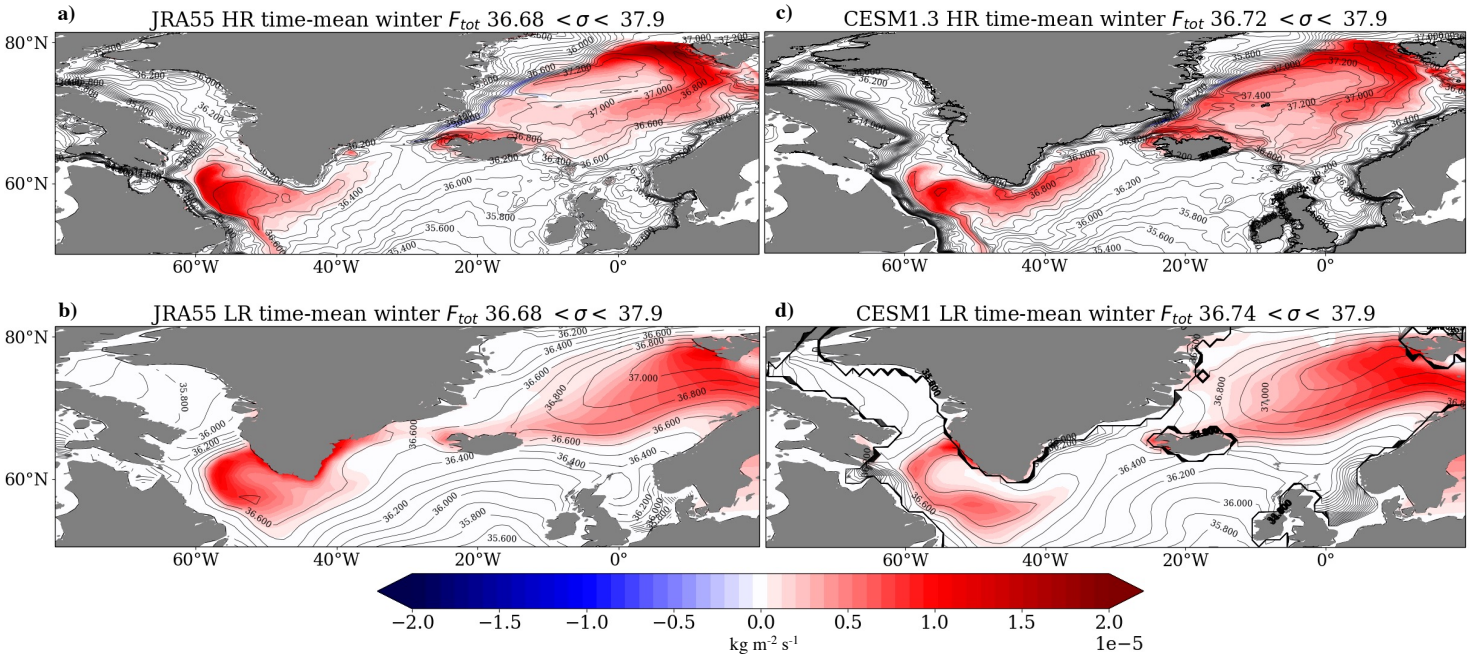

Figure 3.7: Colors: Total climatological winter surface density flux $D(x, y, t)$, calculated using Eq. (2.2) over densities above the maximum density where AMOC reaches 75% of its maximum. Contours: Time-mean winter sea-surface potential density referenced to 2000 m for **a** JRA55-HR, **b** JRA55-LR, **c)** CESM1.3-HR and **d)** CESM1-LR.

To illustrate exactly which parts of each region contribute to the WMT in different density classes, it is useful to look at the full surface-density flux $D(x,y,t)$ calculated from Eq. (2.2). To separate out these contributions, we isolate the $D(x,y,t)$ for densities lower than the minimum density where AMOC reaches 75% of its maximum (Fig. 3.5), densities within the density range where AMOC is at least 75% of its maximum (Fig. 3.6), and densities above that density range (Fig. 3.7). In the lowest density range, the surface-density flux is concentrated in the Irminger and Iceland Basins, with small contributions from the other regions, mainly near coastlines where the water is fresher and lighter than the interior areas (Fig. 3.5). In the density range near the AMOC maximum, CESM1.3-HR reproduces the density flux patterns found in JRA55-HR fairly well. In both of these simulations, most of the Labrador Sea surface density flux is concentrated in the northern area rather than in the southern part, where density fluxes are weaker (Fig. 3.6a, c). The patterns found in the GIN Seas are also similar; however, the surface density fluxes in the southern part of the IIB are much higher in CESM1.3-HR than in JRA55-HR (Fig. 3.6a, c). The low-resolution simulations show similar overall patterns to JRA55-HR, but lack several key features (Fig. 3.6b, d). For example, Labrador Sea fluxes are more concentrated in the central and southern areas compared to JRA55-HR and CESM1.3-HR, particularly in CESM1-LR (Fig. 3.6d). JRA55-LR reproduces the flux patterns in the IIB and GIN Seas fairly well (Fig. 3.6b). However, neither low-resolution simulation has an accurate representation of the more complex density structure found in JRA55-HR and CESM1.3-HR, where the densities are less uniform, particularly near coastlines. At higher densities, in JRA55-HR and CESM1.3-HR, the interior and southern parts of the Labrador Sea contribute more to WMT than in the lower density classes (Fig. 3.7a, c). There are also more contributions from the more interior and northern parts of the GIN Seas. The same overall patterns are found in the low-resolution simulations (Fig. 3.7b, d). However, in JRA55-LR the surface density fluxes are shifted to the east relative to JRA55-HR and CESM1.3-HR, and the northern part of the GIN Seas is not as emphasized as in the high-resolution simulations, with a much more uniform pattern in the eastern GIN Seas (Fig. 3.7b). In CESM1-LR, the contributions to WMT from the

Labrador Sea are smaller, and the eastern area of the GIN Seas is more emphasized compared to in JRA55-LR (Fig. 3.7d). The patterns in both regions overall look more similar to the high-resolution simulations than JRA55-LR.

To allow for a more direct comparison between AMOCσ and the WMT in the different regions, we also calculate the surface-forced overturning streamfunction using Eq. (2.4) from Chapter 2. However, here we calculate this streamfunction for each of the three regions separately, which will allow us to quantify how much the surface-forced WMT in each region contributes to AMOC (neglecting mixing). It is clear that CESM1.3-HR reproduces the surface-forced overturning found in JRA55-HR far better than either low-resolution simulation in all regions (Fig. 3.8a-d, i-l). In JRA55-LR and CESM1-LR, the overturning is too strong in all the regions, especially in the Labrador Sea and IIB (Fig. 3.8e-h, m-p).

To determine exactly what is responsible for the discrepancies in the WMT between JRA55-HR and the other simulations, we look at climatologies of sea-surface heat flux, sea-surface potential temperature, sea-surface salinity and sea-surface potential density. Although the freshwater fluxes also contribute to the WMT, the freshwater components of WMT are very small in all four simulations. Hence we do not show the freshwater fluxes here. For each of these quantities, we show the climatology in JRA55-HR, then the anomalies for the other simulations relative to JRA55-HR. All three simulations exhibit substantial discrepancies in SSTs compared to JRA55-HR. CESM1.3-HR is warmer than JRA55-HR in most of the regions, with some small cool anomalies in the Irminger Basin and the Iceland Sea (Fig. 3.9c). The warm anomalies are most pronounced in the northern part of the GIN Seas. JRA55-LR exhibits larger anomalies in all regions, and is mostly warmer than JRA55-HR, aside from parts of the Labrador and Norwegian Seas (Fig. 3.9b), which is surprising considering that it is forced with the same atmospheric data as JRA55-HR. CESM1-LR actually reproduces the SST found in JRA55-HR better than JRA55-LR, with a similar anomaly pattern but somewhat smaller anomaly magnitudes (Fig. 3.9d).

CESM1.3-HR best reproduces the surface heat fluxes found in JRA55-HR (Fig. 3.10a, c), with some positive anomalies in the central and northern Labrador Sea and broad negative

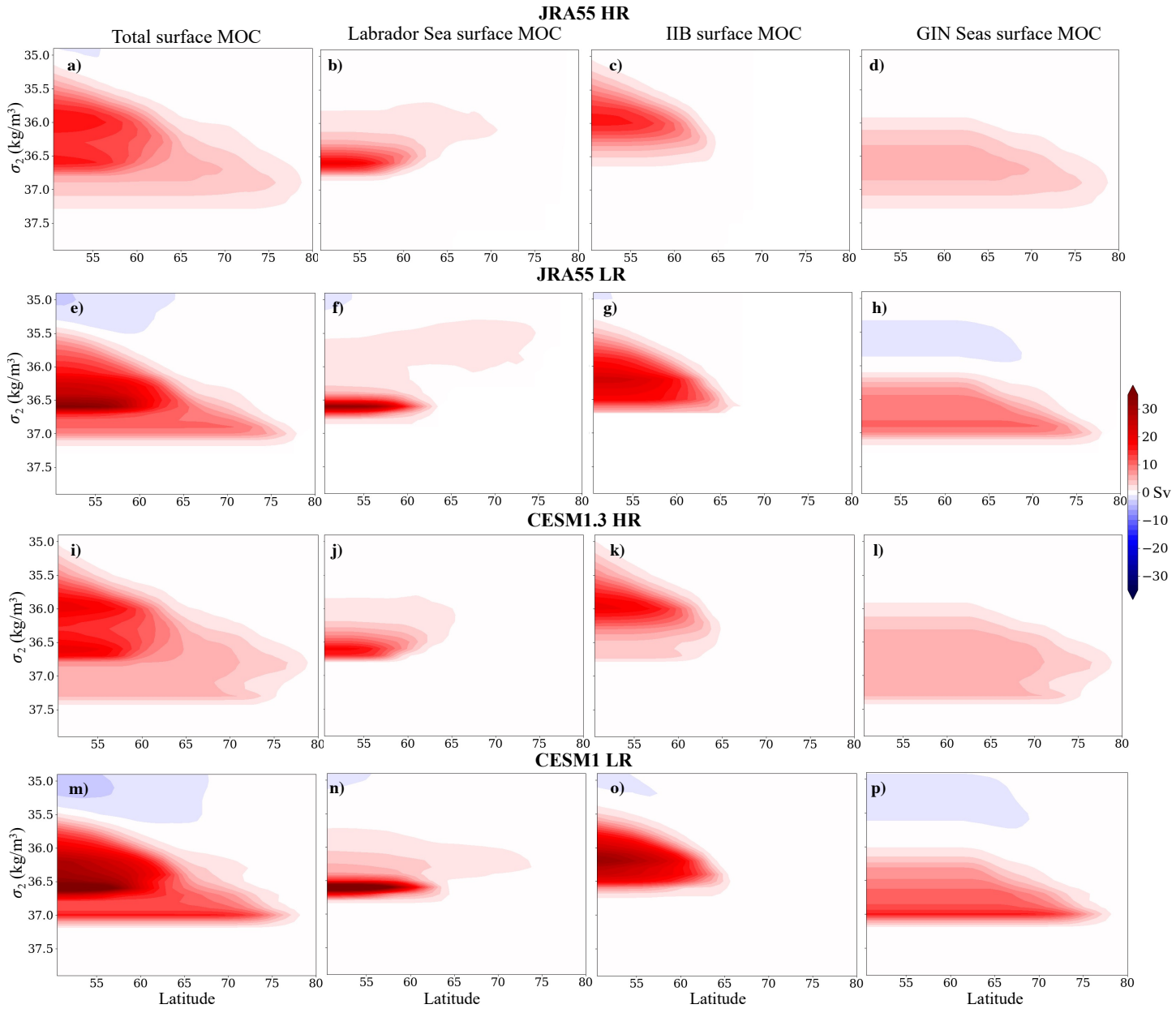

Figure 3.8: Climatological surface-forced overturning streamfunction in **a-d)** JRA55-HR, **e-h)** JRA55-LR, **i-l)** CESM1.3-HR and **m-p)** CESM1-LR computed over all regions (first column), the Labrador Sea (second column), the Irminger-Iceland Basins (IIB, third column) and GIN Seas (fourth column).

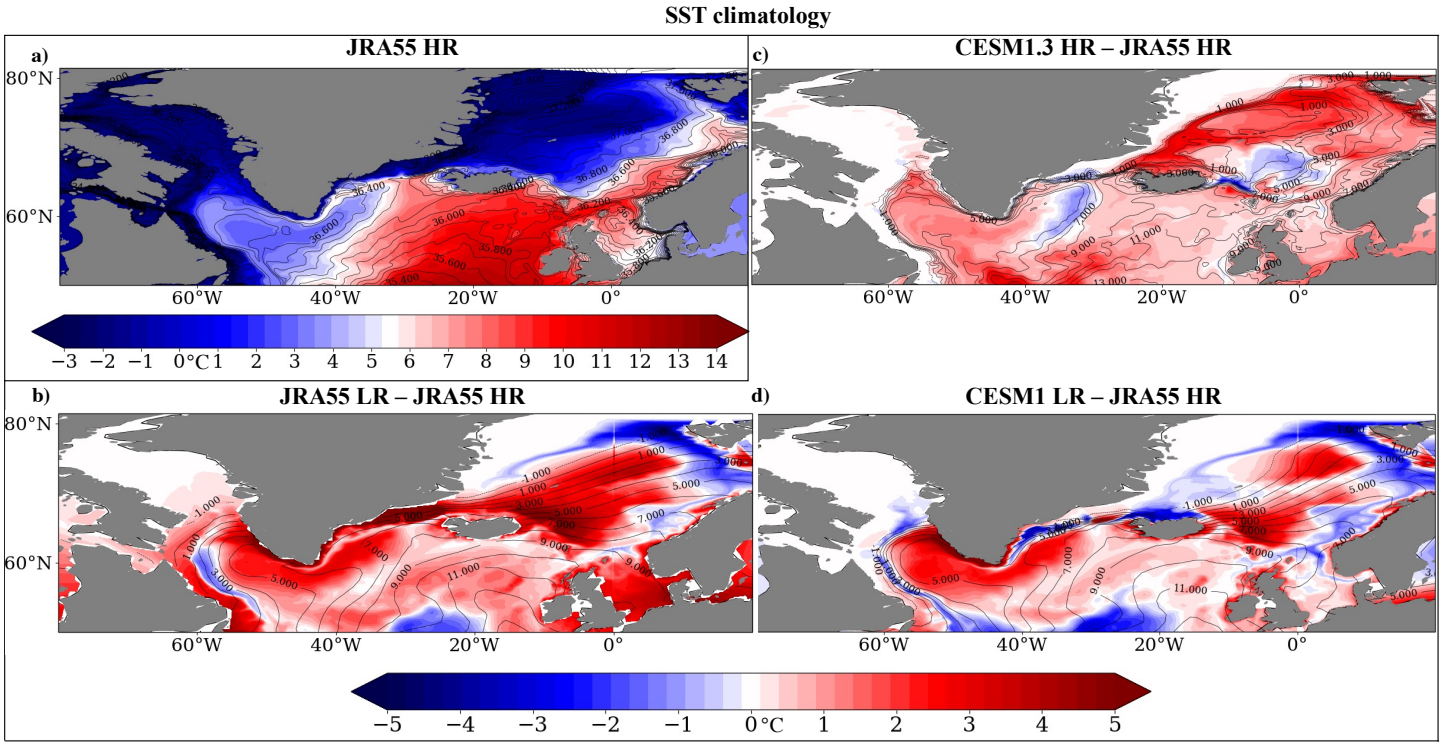

Figure 3.9: **a)** JRA55-HR sea-surface potential temperature climatology. **b-d)** Sea-surface potential temperature climatologies (contours) and anomalies relative to JRA55-HR (colors) for **b)** JRA55-LR, **c)** CESM1.3-HR and **d)** CESM1-LR.

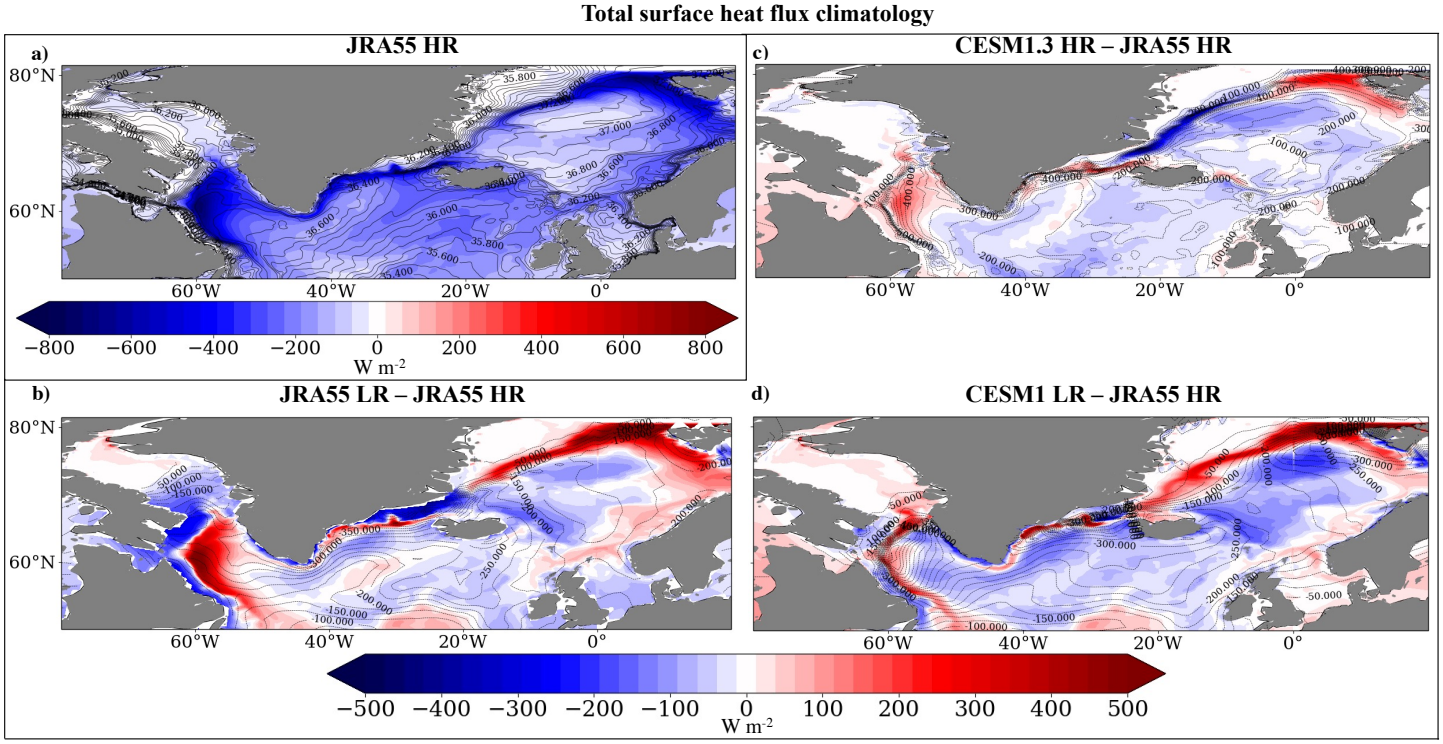

Figure 3.10: **a)** JRA55-HR total sea-surface heat flux climatology. **b-d)** Sea-surface heat flux climatologies (contours) and anomalies relative to JRA55-HR (colors) for **b)** JRA55-LR, **c)** CESM1.3-HR and **d)** CESM1-LR.

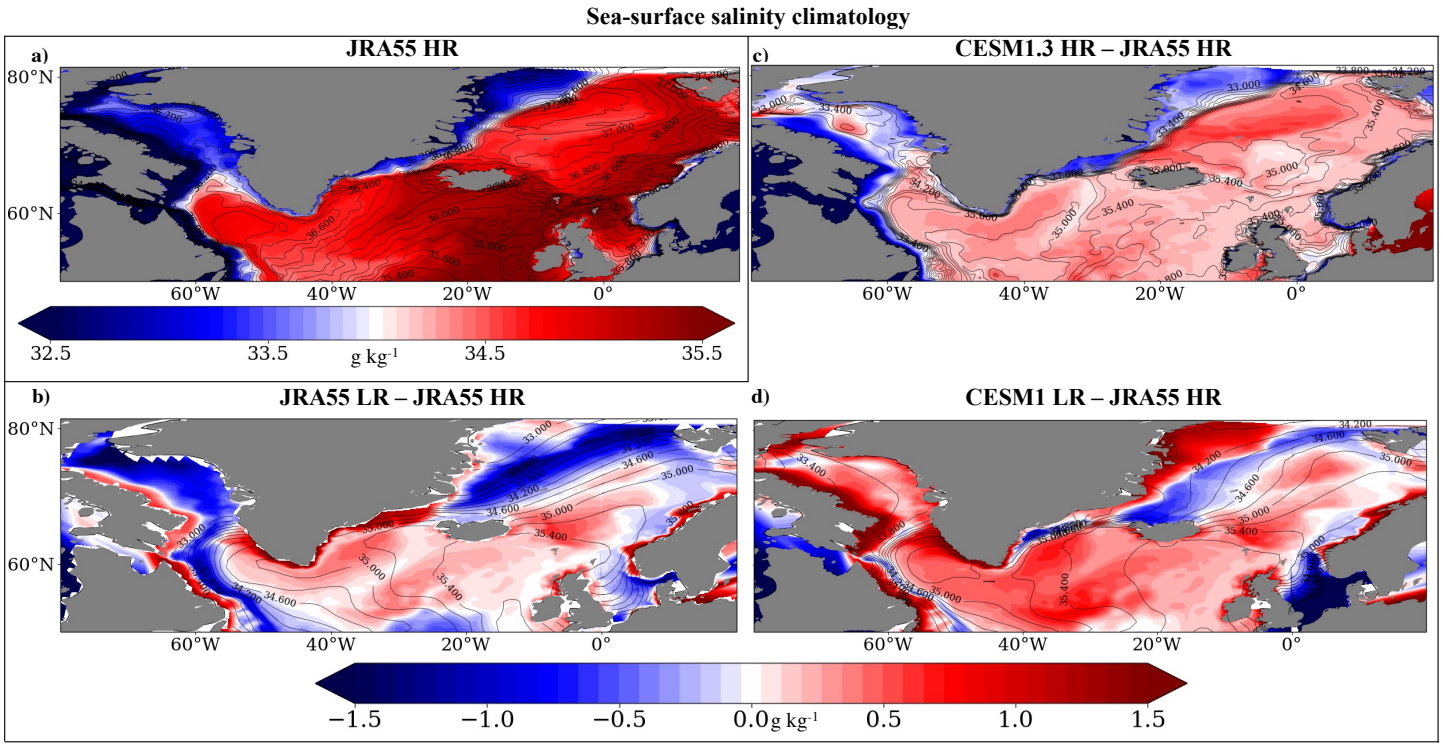

Figure 3.11: **a)** JRA55-HR sea-surface salinity climatology. **b-d)** Sea-surface salinity climatologies (contours) and anomalies relative to JRA55-HR (colors) for **b)** JRA55-LR, **c)** CESM1.3-HR and **d)** CESM1-LR.

anomalies throughout the IIB and GIN Seas, aside from the far north, which exhibits positive anomalies (Fig. 3.10c). The larger (more negative) heat fluxes in the IIB and GIN Seas explain the larger IIB and GIN WMT in CESM1.3-HR compared to JRA55-HR, given that stronger heat fluxes drive higher WMT. JRA55-LR exhibits larger positive anomalies in the Labrador Sea and northern GIN Seas compared to CESM1.3-HR (Fig. 3.10b). In CESM1-LR, there is a mix of positive and negative anomalies in the Labrador Sea, and larger negative anomalies in the central GIN Seas (Fig. 3.10d).

CESM1.3-HR is more saline than JRA55-HR in most regions, with some fresh anomalies in the northern GIN Seas and near coastlines (Fig. 3.11), likely due to increased freshwater

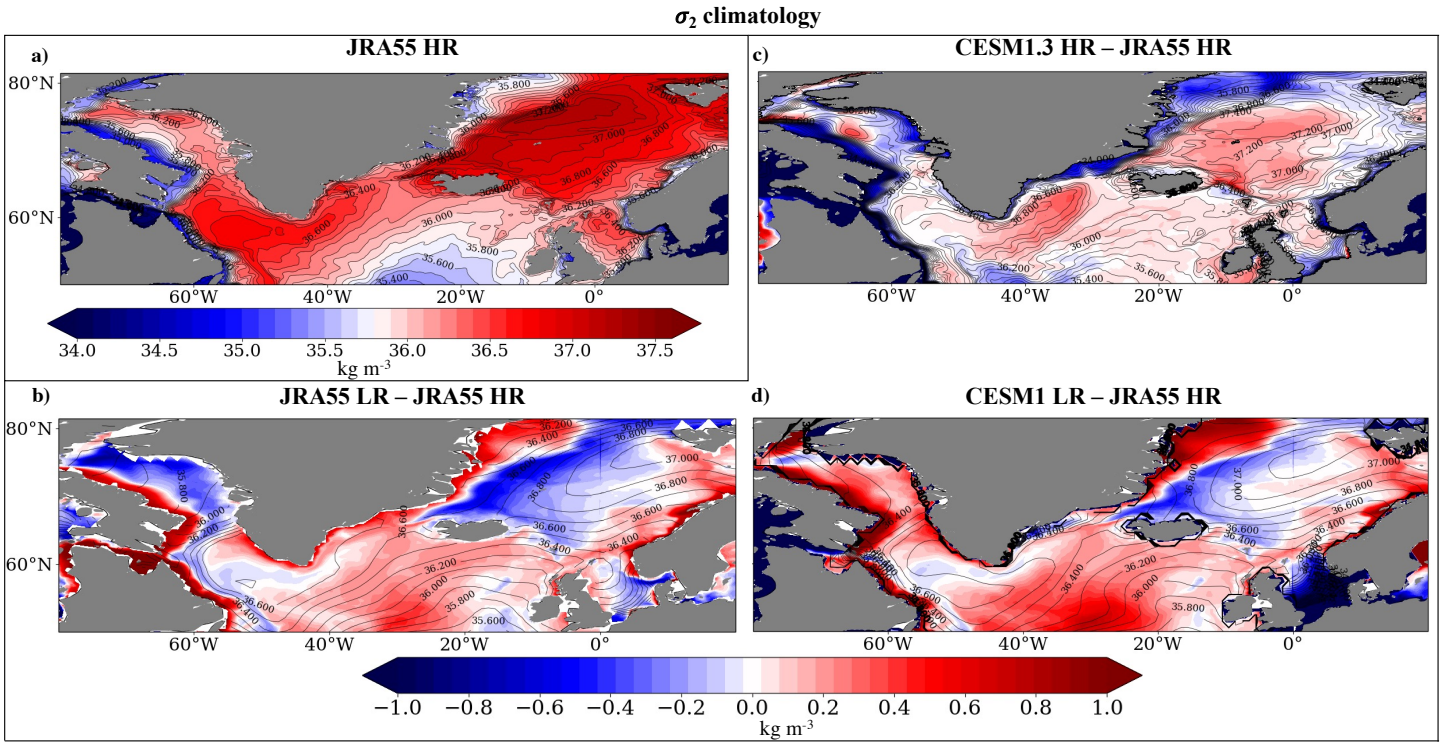

Figure 3.12: **a)** JRA55-HR sea-surface potential density climatology. **b-d)** Sea-surface potential density climatologies (contours) and anomalies relative to JRA55-HR (colors) for **b)** JRA55-LR, **c)** CESM1.3-HR and **d)** CESM1-LR.

runoff compared to JRA55-HR. The salty anomalies are of the same sign as the SST anomalies in the same region, indicating some level of density compensation, though the salinity anomalies dominate, leading to density anomalies of the same sign as the salinity anomalies in most regions (Fig. 3.12c). JRA55-LR has large salinity anomalies relative to JRA55-HR in each region, with fresh anomalies in the western Labrador Sea and positive anomalies to the east, smaller and mostly positive anomalies in the IIB, and a mix of positive and negative anomalies in the GIN Seas (Fig. 3.11b). Similar to in CESM1.3-HR, the salinity anomalies dominate over the temperature anomalies in terms of density, and hence most regions have density anomalies of the same sign as the salinity anomalies (Fig. 3.12b). In CESM1-LR, most regions are more saline than in JRA55-HR, except in parts of the Greenland Sea and the coastal area of the Irminger Basin (Fig. 3.11d). As in the other simulations, these salinity anomalies dominate over the temperature anomalies, and hence most regions are more dense than in JRA55-HR (Fig. 3.12d). The higher densities in the low-resolution simulations explain why the WMT and AMOC peaks occur at higher densities than in JRA55-HR and CESM1.3-HR (Fig. 3.4), and the generally more uniform density fields in the Labrador Sea explain the narrower WMT peaks in the LR simulations compared to JRA55-HR and CESM1.3-HR. Also, the high densities in the GIN Seas in CESM1.3-HR explain why there is positive WMT in that region at higher densities than what is seen in the other models (Fig. 3.4c).

3.4 Summary of AMOC and WMT Climatology

Based on these results, increasing the atmospheric and ocean resolution of a coupled model yields a WMT which better reproduces what is found in a reanalysis-forced high-resolution ocean simulation compared to an equivalent low-resolution coupled simulation. The ocean resolution appears to be particularly important, as even a low-resolution ocean simulation forced with atmospheric reanalyses doesn't represent the WMT as accurately as a full high--resolution coupled model simulation. This makes sense considering that high-resolution simulations more accurately resolve mesoscale ocean eddies, which tends to improve the

representation of mixed-layer depth and deepwater formation, particularly in the Labrador Sea.

This better representation of WMT is explained by a more accurate representation of the density structure in the high-resolution simulation compared to the low-resolution versions, which have relatively uniform density fields in comparison, particularly in the Labrador Sea. Smaller discrepancies in surface heat fluxes in the deepwater formation regions in the high-resolution simulation also help explain why it captures the climatological WMT better than the low-resolution simulations.

3.5 Part II: Mechanisms of low-frequency AMOC variability in CESM1.3-HR and CESM1-LR

In Chapter 2, we found that the Labrador Sea plays a much more dominant role in driving AMOC variability than would be expected based on its role in the climatology. However, it is still worth investigating whether the ocean and atmospheric resolution of a model would affect this result, given that higher resolution models represent Labrador Sea processes much better than low-resolution ones (see Part I). Hence, here we carry out an analysis similar to Chapter 2, except we focus entirely on AMOCσ instead of Atlantic OHT because AMOC is more directly linked to WMT than OHT. Our goal is to determine whether the mechanisms of low-frequency AMOC variability in low-resolution simulations are still found in high-resolution models. Hence we first compute the LFPs and LFCs of annual-mean AMOCσ in CESM1.3-HR and CESM1-LR, then calculate lead-lag regressions between the first LFC and other fields, including AMOCσ, winter MLD, surface-forced WMT and winter sea-level pressure (SLP).

The first LFPs of AMOC in CESM1.3-HR and CESM1-LR share some common features, with maxima in the mid to subpolar latitudes. In CESM1.3-HR, the maximum value is equal to **1.41** Sv and is located at 51.2° N and $\sigma_2 = \mathbf{36.725}$ kg/m^3. In CESM1-LR, the maximum value is equal to **2.51** Sv and is located at 53.5° N and $\sigma_2 = \mathbf{36.74}$ kg/m^3. This is substantially stronger and at a higher latitude and density than in CESM1.3-HR. The peak

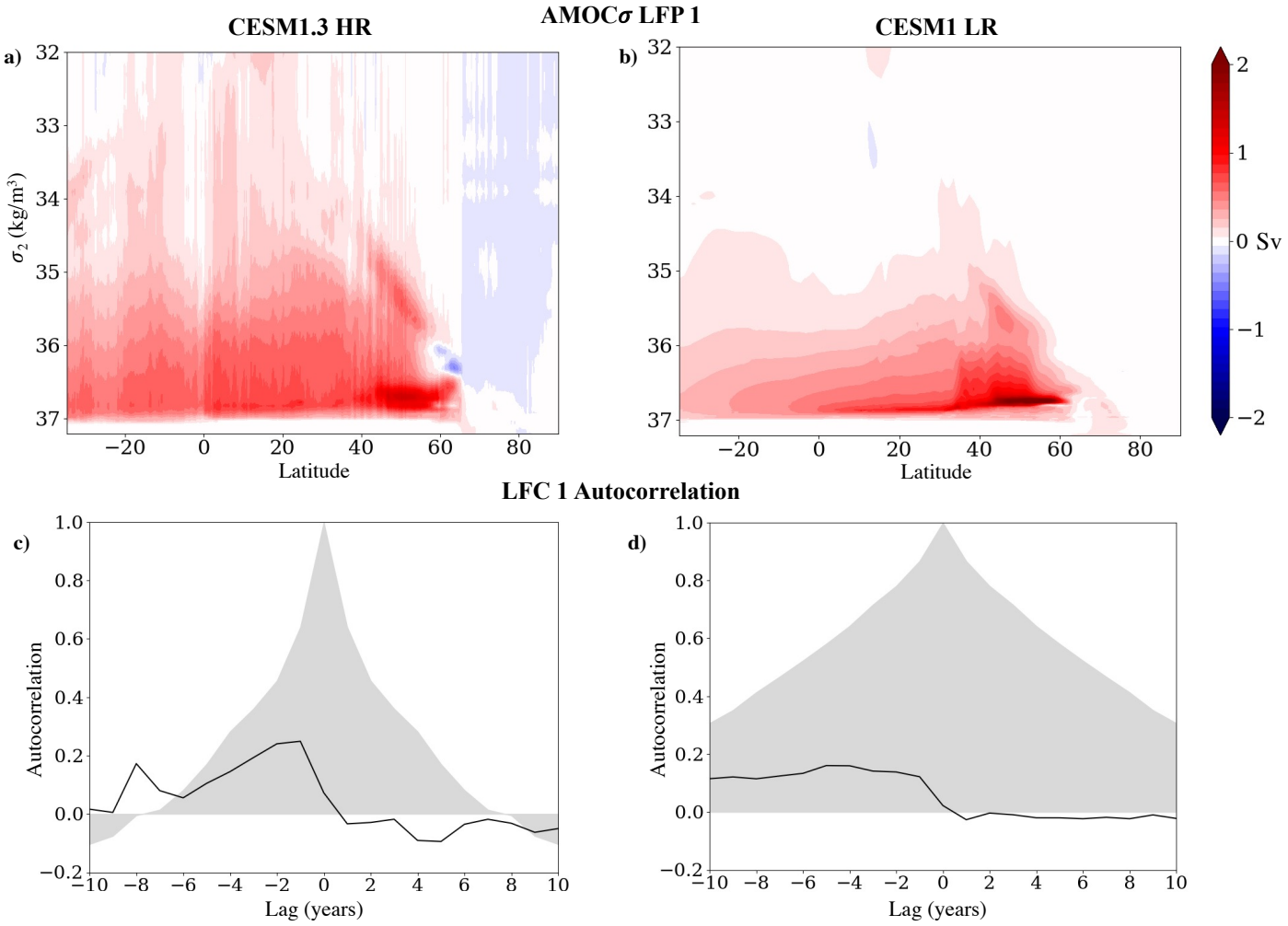

Figure 3.13: Top row: First LFP of AMOCσ for **a)** CESM1.3-HR and **b)** CESM1-LR. Bottom row: Autocorrelations of the first LFC (shaded) and NAO-LFC 1 correlations (solid black lines) for **c)** CESM1.3-HR and **d)** CESM1-LR.

is also broader in CESM1.3-HR. The other major difference is that the positive values extend to lower densities in CESM1.3-HR compared to CESM1-LR. The ratios of low-frequency to total variance for the LFPs are equal to 0.67 and 0.87 for CESM1.3-HR and CESM1-LR, respectively. The LFC autocorrelations remain high for much longer lag times in CESM1-LR compared to CESM1.3-HR (Fig. 3.13c, d). In CESM1.3-HR, the autocorrelation drops off quite quickly, turning negative at lag 8 years (Fig. 3.13c).

In CESM1.3-HR, about four years before the time of maximum AMOC, there is a persistent SLP pattern associated with anomalous northwesterly winds off eastern North America (Fig. 3.14b). This pattern remains until lag zero (Fig. 3.14b-e). After lag zero, the pattern actually reverses (Fig. 3.14e, f) and becomes a pattern that looks more like the negative NAO phase. In CESM1-LR, there is a similar pattern at lead times (Fig. 3.14g-j). At lag zero, this pattern becomes more zonal and the eastern SLP intensifies (Fig. 3.14k). After lag zero, the pattern dissipates completely (Fig. 3.14l). Both of these models show similar patterns at lead times to what is found in the models in Chapter 2. As mentioned in Chapter 2, because the persistence time scale of SLP anomalies is less than one month (Ambaum and Hoskins, 2002), the persistence of this pattern must be due to memory coming from the ocean. However, unlike all of the low-resolution models, including CESM1-LR and the LR models discussed in Chapter 2, CESM1.3-HR actually shows a coherent pattern after the time of maximum AMOC. This indicates a substantial atmospheric response to the low-frequency AMOC variability not seen in the equivalent low-resolution version of the same model. This response can also be seen from the lead-lag correlations of NAO and LFC 1 for CESM1.3-HR (Fig. 3.13c).

These anomalous northwesterly winds at lead times cause mixed layers to deepen in the Labrador Sea in both models (Fig. 3.15a-d, g-j). In CESM1.3-HR, mixed layers reach their deepest at lead 2 before quickly dissipating starting at lag zero (Fig. 3.15a-e). There are also some areas with deep mixed layers in the IIB and GIN Seas at lead times, which remain until lag zero (Fig. 3.15a-e). In CESM1-LR, mixed layers in the Labrador Sea are already deep by lead 6, and remain deep until the time of maximum AMOC, when they rapidly shoal.

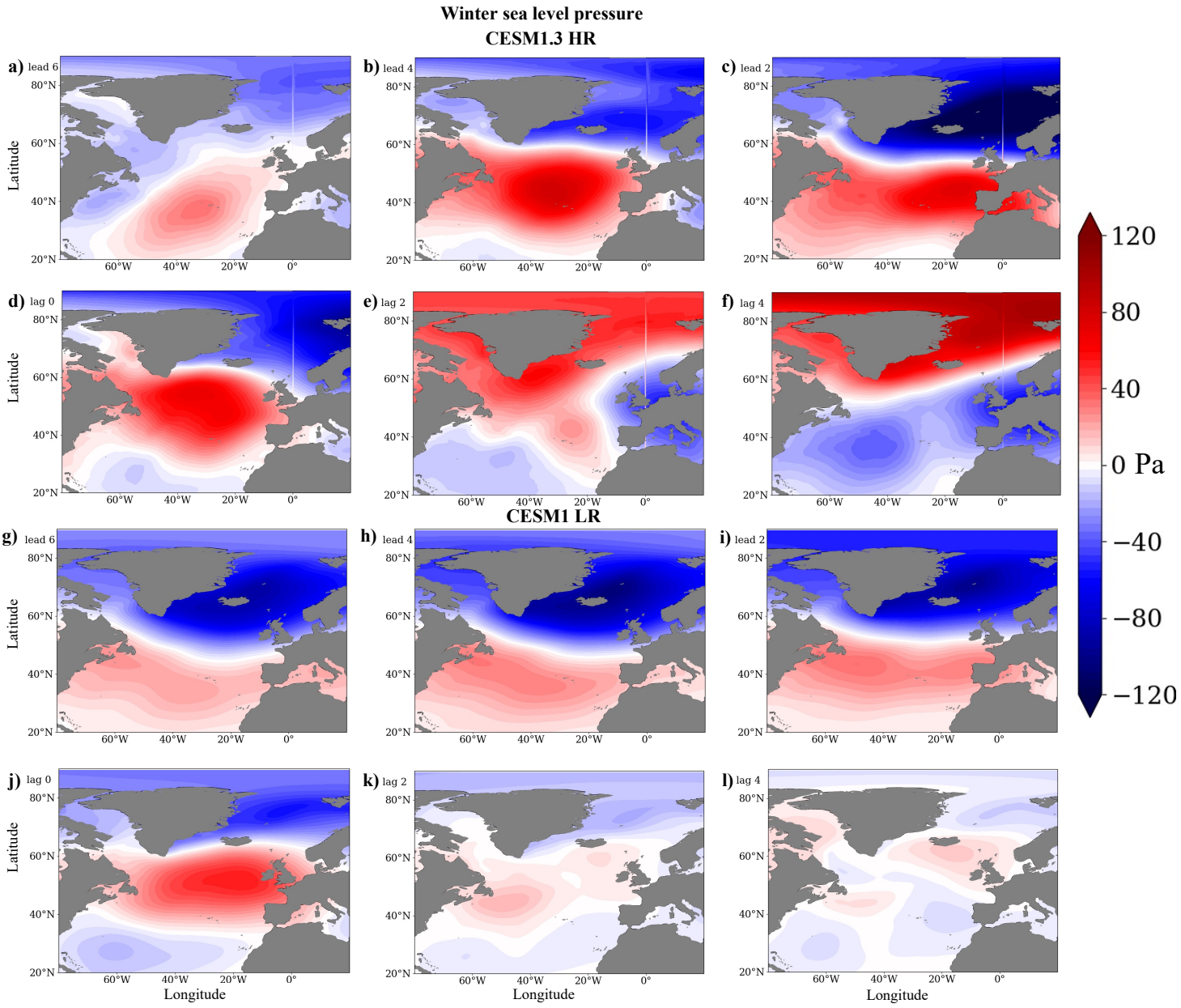

Figure 3.14: Lead-lag regressions of sea-level pressure averaged over January, February and March onto the first LFC of AMOCσ for **(a-f)** CESM1.3-HR and **(g-l)** CESM1-LR. Lead times indicate anomalies that lead the LFC, i.e., prior to the maximum AMOC. Because the LFCs are unitless, the regressions simply have units of Pa (N/m^2).

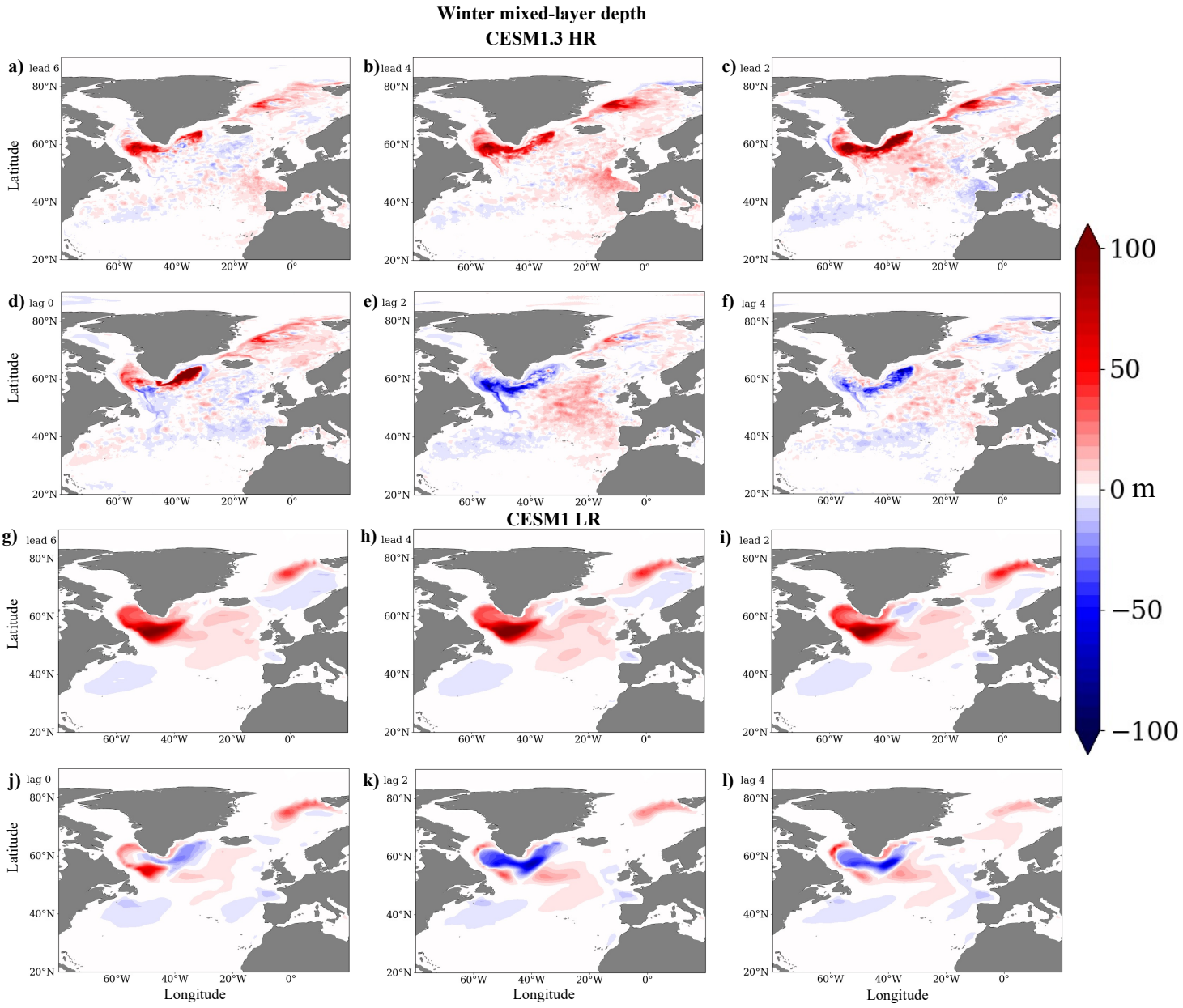

Figure 3.15: Lead-lag regressions of mixed-layer depth averaged over January, February and March onto the first LFC of AMOCσ for **(a-f)** CESM1.3-HR and **(g-l)** CESM1-LR. Lead times indicate anomalies that lead the LFC, i.e., prior to the maximum AMOC. Because the LFCs are unitless, the regressions simply have units of m.

There are also positive MLD anomalies in the GIN Seas at lead times (Fig. 3.15g-k).

In CESM1.3-HR, before the time of maximum AMOC, AMOC steadily strengthens, with positive anomalies rapidly spreading southwards and to lower densities leading up to lag zero (Fig. 3.16a-e). After lag zero, AMOC rapidly weakens (Fig. 3.16f). In CESM1-LR, AMOC is already strong by lead 6 (Fig. 3.16g), with the main feature of the progression to lag zero being that positive anomalies spread southwards and to slightly lower densities (Fig. 3.16g-k). After lag zero, AMOC slowly weakens (Fig. 3.16l). This persistently strong AMOC can be explained by the much higher autocorrelations of LFC 1 in CESM1-LR compared to CESM1.3-HR (Fig. 3.13c, d).

In CESM1.3-HR, concurrent with the strengthening of AMOC and the deepening of mixed layers in the Labrador Sea, IIB and GIN Seas, WMT in the Labrador Sea strengthens, reaching its maximum two years before the time of maximum AMOC (Fig. 3.17a). This peak is equal to 1.29 Sv and is located at $\sigma_2 = 36.81$ kg/m^3, which is at a substantially higher density than the location of the maximum AMOC anomaly at lag zero, but is still within the density range of the broad positive AMOC anomaly. After lead 2, the WMT rapidly decreases. The ENA WMT also increases at lead times, peaking at lead one years (Fig. 3.17c). This peak is equal to 0.75 Sv and is located at $\sigma_2 = 36.84$, which is actually further from the peak in AMOC than the Labrador Sea WMT peak. The peak in ENA WMT is mostly due to changes in IIB WMT rather than the GIN Seas (not shown).

In CESM1-LR, the Labrador Sea WMT also increases at lead times, reaching its maximum at lead 2 years (Fig. 3.17b). This maximum is equal to 3.99 Sv and is located at $\sigma_2 = 36.76$ kg/m^3, which is at a slightly higher density than the maximum AMOC anomaly. The ENA WMT also strengthens at lead times, but already peaks by lead 4 years (Fig. 3.17d). This peak is equal to 0.82 Sv and is located at $\sigma_2 = 36.62$ kg/m^3, which is at a substantially lower density than the maximum AMOC anomaly. This WMT increase is mostly due to changes in the IIB rather than the GIN Seas (not shown).

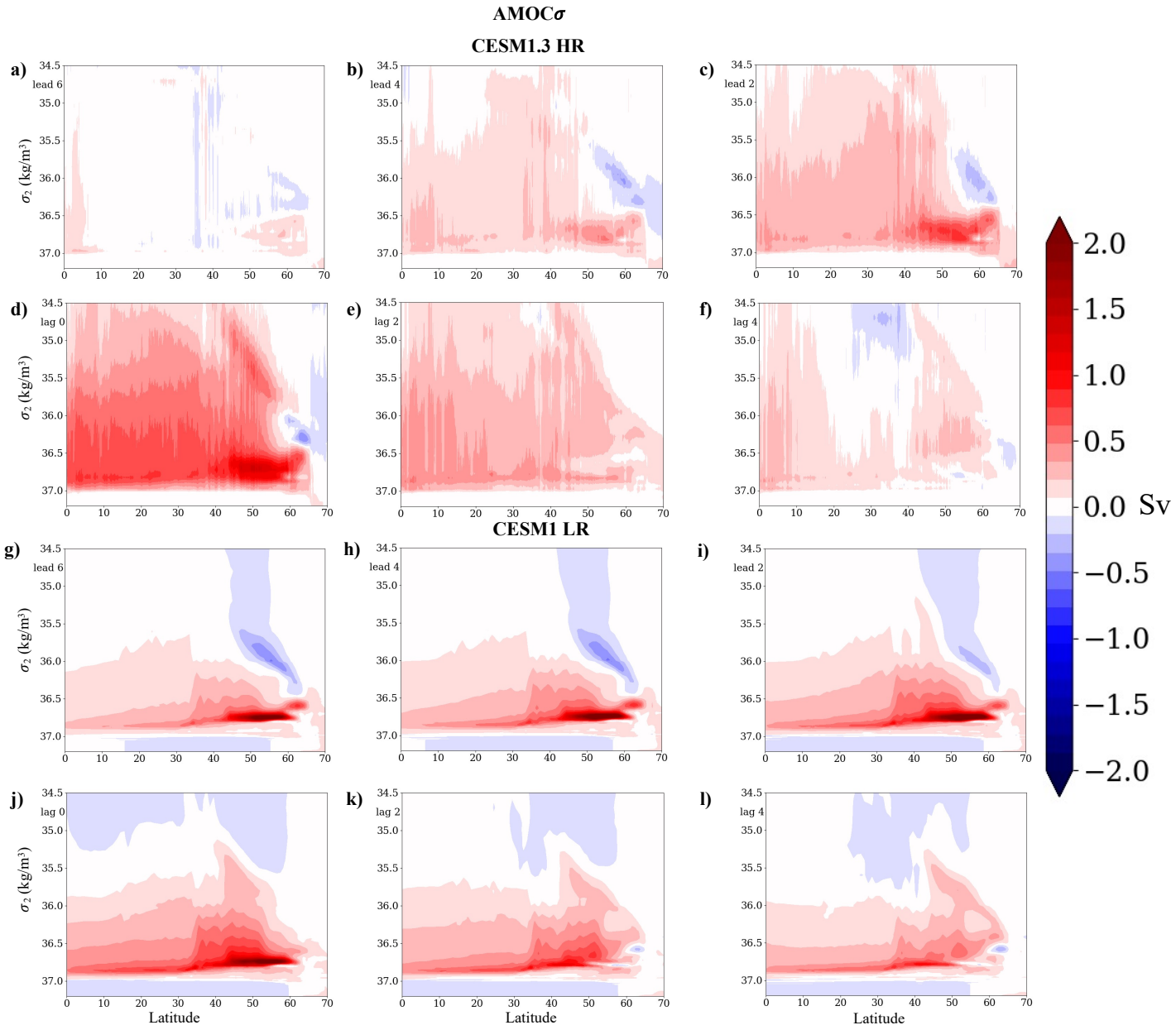

Figure 3.16: Lead-lag regressions of annual-mean AMOC in density coordinates onto the first LFC of AMOCσ for **(a-f)** CESM1.3-HR and **(g-l)** CESM1-LR. Lead times indicate anomalies that lead the LFC, i.e., prior to the maximum AMOC. Because the LFCs are unitless, the regressions simply have units of Sv.

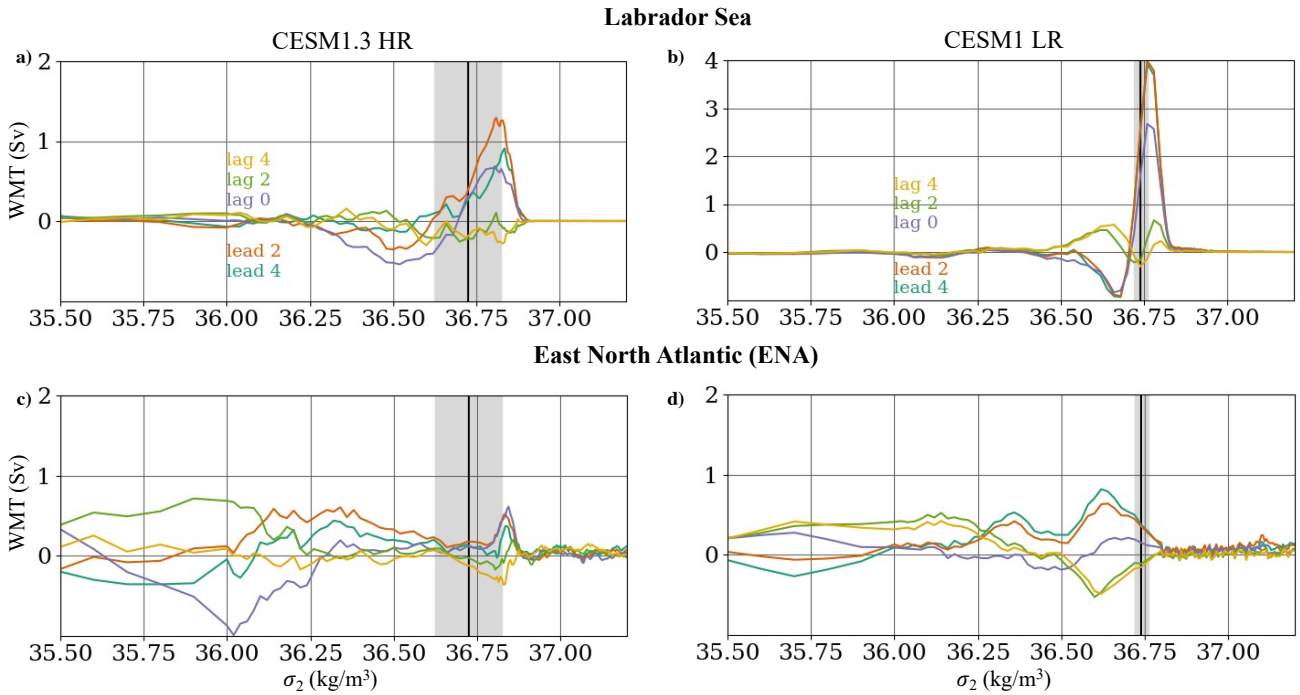

Figure 3.17: Lead-lag regressions of water mass transformation (WMT) onto the first LFC of AMOCσ for CESM1.3-HR (left column) and CESM1-LR (right column). **a, b)** WMT summed over the Labrador Sea region. **c, d)** WMT summed over the Eastern North Atlantic (ENA) section. The black vertical lines indicate the density where the AMOCσ regression at lag zero reaches its maximum in each model. The grey shaded areas represent the density range where the AMOCσ regression at lag zero is within 25% of its maximum value. Fig. 3.3 shows what we consider to be the Labrador Sea, the Irminger and Iceland Basins, and the GIN Seas in this calculation. The Eastern North Atlantic (ENA) here includes both the Irminger and Iceland Basins and the GIN Seas. Lead means LFC 1 lags, i.e., prior to the maximum AMOC. Because the LFCs are unitless, the regressions simply have units of Sv.

3.6 Summary of AMOC variability in CESM1.3-HR and CESM1-LR

Here, we have used LFCA to look at mechanisms of low-frequency AMOC variability in both a low and high-resolution version of the same model. Based on this, it appears that despite the high-resolution model showing a smaller role for the Labrador Sea in climatological WMT and AMOC than in the low-resolution version, it still appears to play a major role in the WMT and AMOC variability. Though it is unclear exactly which density range matters most for AMOC given that we neglect mixing, it is likely that higher density classes matter because mixing tends to make the densest water lighter.

The high-resolution model appears to show a substantial atmospheric response to the AMOC variability not seen in the low-resolution version. This type of atmospheric response has been seen in a study of a medium-resolution coupled model, but with a longer lag time between the AMOC change and the negative NAO response (Wen et al., 2016). A positive NAO-like response to AMOC variability has also been found in a low-resolution model (Dong and Sutton, 2003). Overall, it appears that the mode of variability of AMOC in the high-resolution model is associated with stronger anomalies in atmospheric fields (i.e., sea-level pressure), while the low-resolution version is associated with stronger anomalies in ocean fields, namely the water-mass transformation, particularly in the Labrador Sea.

In comparison to the models shown in Chapter 2 as well as CESM1-LR, CESM1.3-HR shows a lesser role for the Labrador Sea in driving AMOC variability. However, the mechanisms driving the variability are still similar, with a substantial deepening of mixed layers and strengthening of WMT in the Labrador Sea as well as a similar NAO-like pattern leading up to the time of maximum AMOC. The other primary difference compared to the LR models, as mentioned in the previous paragraph, is the enhanced atmospheric response to the AMOC change. However, it is important to note that the high-resolution simulation used here is fairly short (161 years), and it is possible that this response would be weaker when diagnosed from the full 350-year simulation.

3.7 Overall Summary and Conclusions

Our results suggest that increasing the ocean and atmospheric resolution of a coupled model substantially improves the representation of climatological AMOC and WMT. However, the mechanisms driving low-frequency AMOC variability remain qualitatively similar even though the climatologies differ. This is consistent with what we found in Chapter 2, where the mechanisms were similar across three low-resolution models with distinct AMOC and WMT climatologies.

CONCLUSIONS

This dissertation contributes to the understanding of the processes driving low-frequency variability in North Atlantic ocean heat transport and the causes of climatological differences in water-mass transformation and AMOC between models. In Chapter 1, we focused on the mechanisms that drive changes in OHT from the North Atlantic into the Arctic both under CO_2 forcing and internal variability in one low-resolution coupled model. From this analysis, we determined that the mechanisms governing OHT changes differ based on whether the changes are forced by CO_2 or are due to internal variability. Under internal variability, low-frequency increases in OHT from the North Atlantic into the Arctic are caused primarily by a strengthened AMOC farther south, which carries anomalous heat northward into the subpolar gyre. The time-mean subpolar gyre circulation then carries this heat northwards into the Nordic Seas, where both anomalous and time-mean local gyre circulations advect it into the Arctic. However, under CO_2 forcing, AMOC weakens substantially, but CO_2 induced warm temperature anomalies in the North Atlantic and Nordic Seas are advected northward by time-mean circulations and local gyre circulation changes at 70° N. A noteworthy result of this work is that an increase in OHT into the Arctic under global warming can occur even while AMOC and northward OHT decrease farther to the south.

In Chapter 2, we broadened the focus to include the entire North Atlantic, with a primary interest in the link between unforced low-frequency changes in OHT (and AMOC) and different surface properties, including sea-level pressure, surface wind stress, mixed-layer depth, gyre circulations, sea-surface temperature and density, and surface-forced water-mass transformation in deepwater formation regions. In this case, instead of looking solely at one model, we looked at three models with different representations of deepwater formation and deep convection in the high latitude regions to determine how much this representation affects

the link between OHT variability and WMT changes. To do this, we used a novel method called a low-frequency component analysis to isolate a mode of variability that emphasizes low-frequency variability in the OHT data. Using this approach, we identified a mechanism that prevails across the three models - OHT changes are driven by anomalous northwesterly winds off eastern North America that occur in the years leading up to the time of maximum OHT. These winds cool and densify the Labrador Sea water, deepening the mixed layers and increasing the WMT in the region. This WMT increase then causes AMOC and its associated OHT to strengthen. Then the strengthened AMOC carries anomalous warm water northward into the subpolar gyre, which reduces the positive density and WMT anomalies, weakening the AMOC and OHT as a result. The most noteworthy result of this analysis is that the Labrador Sea plays a major role in the WMT, AMOC and OHT variability in all three of the models, despite the fact that other regions, namely the Irminger and Iceland Basins and the GIN Seas, dominate the climatological WMT and AMOC.

In Chapter 3 Part I, we explored the differences in climatological WMT between high and low-resolution coupled model simulations, and compared them to the same high and low resolution ocean models forced with atmospheric reanalyses. Our analysis indicated that a high-resolution eddy-resolving coupled model reproduces the climatological WMT found in a reanalysis-forced ocean simulation much more effectively than its low-resolution counterpart, due to a much better representation of the sea-surface density structure, as well as smaller discrepancies in surface heat fluxes in deepwater formation regions compared to the low-resolution models. Also, the low-resolution reanalysis-forced ocean simulation does not effectively capture the WMT found in the high-resolution version, despite being forced with the same reanalysis data. This indicates that the ocean resolution is very important in setting the mean state of WMT, even when the ocean is forced with the same atmospheric reanalysis data. In Part II, we looked at low-frequency variability in the high and low-resolution coupled model simulations using the same method as in Chapter 2. We found that the high-resolution simulation still exhibits a similar mechanism of low-frequency AMOC variability to the low-resolution version, as well as the low-resolution simulations in Chapter

2. The Labrador Sea WMT still plays a primary role in driving the AMOC variability, albeit reduced compared to the low-resolution simulation. Given that this high-resolution model reproduces reanalysis-forced WMT fairly well, these results raise the interesting possibility that the Labrador Sea might be playing a primary role in driving low-frequency variability in AMOC and OHT despite only playing a minor role in the interannual variability and mean state.

As a whole, these chapters provide a new understanding of the mechanisms of low-frequency variability in OHT into the Arctic as well as North Atlantic OHT. This dissertation describes the mechanisms of North Atlantic OHT in several low-resolution models with distinct representations of subpolar deepwater formation, as well as a high-resolution model that more accurately resolves subpolar ocean properties to check the robustness of the low-resolution analysis results.

BIBLIOGRAPHY

Allen, M. R. and Smith, L. A. (1997). Optimal filtering in singular spectrum analysis. *Physics Letters A*, 234(6):419--428.

Ambaum, M. H. P. and Hoskins, B. J. (2002). The NAO Troposphere-Stratosphere Connection. *Journal of Climate*, 15(14):1969--1978.

Årthun, M. and Eldevik, T. (2016). On Anomalous Ocean Heat Transport toward the Arctic and Associated Climate Predictability. *Journal of Climate*, 29(2):689--704.

Årthun, M., Wills, R. C. J., Johnson, H. L., Chafik, L., and Langehaug, H. R. (2021). Mechanisms of decadal North Atlantic climate variability and implications for the recent cold anomaly. *Journal of Climate*, pages 3421--3439.

Bailey, D. A., Rhines, P. B., and Häkkinen, S. (2005). Formation and pathways of North Atlantic Deep Water in a coupled ice-ocean model of the Arctic-North Atlantic Oceans. *Climate Dynamics*, 25(5):497--516.

Bitz, C. M., Gent, P. R., Woodgate, R. A., Holland, M. M., and Lindsay, R. (2006). The Influence of Sea Ice on Ocean Heat Uptake in Response to Increasing CO2. *Journal of Climate*, 19(11):2437--2450.

Bjerknes, J. (1964). Atlantic Air-Sea Interaction. volume 10 of *Advances in Geophysics*, pages 1--82. Elsevier.

Böning, C. W., Bryan, F. O., Holland, W. R., and Döscher, R. (1996). Deep-Water Formation and Meridional Overturning in a High-Resolution Model of the North Atlantic. *Journal of Physical Oceanography*, 26(7):1142--1164.

Bony, S., Dufresne, J. L., Le Treut, H., Morcrette, J. J., and Senior, C. (2004). On dynamic and thermodynamic components of cloud changes. *Climate Dynamics*, 22(2):71--86.

Brambilla, E. and Talley, L. D. (2008). Subpolar Mode Water in the northeastern Atlantic: 1. Averaged properties and mean circulation. *Journal of Geophysical Research: Oceans*, 113(C4).

Brandt, P., Funk, A., Czeschel, L., Eden, C., and Böning, C. W. (2007). Ventilation and Transformation of Labrador Sea Water and Its Rapid Export in the Deep Labrador Current. *Journal of Physical Oceanography*, 37(4):946--961.

Brodeau, L. and Koenigk, T. (2016). Extinction of the northern oceanic deep convection in an ensemble of climate model simulations of the 20th and 21st centuries. *Climate Dynamics*, 46(9):2863--2882.

Caesar, L., Rahmstorf, S., Robinson, A., Feulner, G., and Saba, V. (2018). Observed fingerprint of a weakening Atlantic Ocean overturning circulation. *Nature*, 556(7700):191--196.

Cane, M. A., Clement, A. C., Murphy, L. N., and Bellomo, K. (2017). Low-Pass Filtering, Heat Flux, and Atlantic Multidecadal Variability. *Journal of Climate*, 30(18):7529--7553.

Chafik, L. and Rossby, T. (2019). Volume, Heat, and Freshwater Divergences in the Subpolar North Atlantic Suggest the Nordic Seas as Key to the State of the Meridional Overturning Circulation. *Geophysical Research Letters*, 46(9):4799--4808.

Chang, P., Zhang, S., Danabasoglu, G., Yeager, S. G., Fu, H., Wang, H., Castruccio, F. S., Chen, Y., Edwards, J., Fu, D., Jia, Y., Laurindo, L. C., Liu, X., Rosenbloom, N., Small, R. J., Xu, G., Zeng, Y., Zhang, Q., Bacmeister, J., Bailey, D. A., Duan, X., DuVivier, A. K., Li, D., Li, Y., Neale, R., Stössel, A., Wang, L., Zhuang, Y., Baker, A., Bates, S., Dennis, J., Diao, X., Gan, B., Gopal, A., Jia, D., Jing, Z., Ma, X., Saravanan, R., Strand,

W. G., Tao, J., Yang, H., Wang, X., Wei, Z., and Wu, L. (2020). An Unprecedented Set of High-Resolution Earth System Simulations for Understanding Multiscale Interactions in Climate Variability and Change. *Journal of Advances in Modeling Earth Systems*, 12(12):e2020MS002298.

Chylek, P., Hengartner, N., Lesins, G., Klett, J. D., Humlum, O., Wyatt, M., and Dubey, M. K. (2014). Isolating the anthropogenic component of Arctic warming. *Geophysical Research Letters*, 41(10):3569--3576. 2014GL060184.

Cuny, J., Rhines, P. B., Niiler, P. P., and Bacon, S. (2002). Labrador Sea Boundary Currents and the Fate of the Irminger Sea Water. *Journal of Physical Oceanography*, 32(2):627--647.

Danabasoglu, G., Bates, S. C., Briegleb, B. P., Jayne, S. R., Jochum, M., Large, W. G., Peacock, S., and Yeager, S. G. (2012a). The CCSM4 Ocean Component. *Journal of Climate*, 25(5):1361--1389.

Danabasoglu, G., Yeager, S. G., Kwon, Y.-O., Tribbia, J. J., Phillips, A. S., and Hurrell, J. W. (2012b). Variability of the Atlantic Meridional Overturning Circulation in CCSM4. *Journal of Climate*, 25(15):5153--5172.

Danabasoglu, G., Yeager, S. G., Kwon, Y.-O., Tribbia, J. J., Phillips, A. S., and Hurrell, J. W. (2012c). Variability of the Atlantic Meridional Overturning Circulation in CCSM4. *Journal of Climate*, 25(15):5153--5172.

Day, J. J., Hargreaves, J. C., Annan, J. D., and Abe-Ouchi, A. (2012). Sources of multi--decadal variability in Arctic sea ice extent. *Environmental Research Letters*, 7(3):034011.

de Boyer Montégut, C., Madec, G., Fischer, A. S., Lazar, A., and Iudicone, D. (2004). Mixed layer depth over the global ocean: An examination of profile data and a profile-based climatology. *Journal of Geophysical Research: Oceans*, 109(C12).

de Boyer Montégut, C., Mignot, J., Lazar, A., and Cravatte, S. (2007). Control of salinity on the mixed layer depth in the world ocean: 1. General description. *Journal of Geophysical Research: Oceans*, 112(C6).

Delworth, T., Manabe, S., and Stouffer, R. J. (1993). Interdecadal Variations of the Thermohaline Circulation in a Coupled Ocean-Atmosphere Model. *Journal of Climate*, 6(11):1993--2011.

Delworth, T. L. and Zeng, F. (2016). The Impact of the North Atlantic Oscillation on Climate through Its Influence on the Atlantic Meridional Overturning Circulation. *Journal of Climate*, 29(3):941--962.

Delworth, T. L., Zeng, F., Vecchi, G. A., Yang, X., Zhang, L., and Zhang, R. (2016). The North Atlantic Oscillation as a driver of rapid climate change in the Northern Hemisphere. *Nature Geosci*, 9(7):509--512.

Delworth, T. L., Zhang, R., and Mann, M. E. (2007). *Decadal to Centennial Variability of the Atlantic from Observations and Models*, pages 131--148. American Geophysical Union (AGU).

Deser, C., Alexander, M. A., Xie, S.-P., and Phillips, A. S. (2010). Sea Surface Temperature Variability: Patterns and Mechanisms. *Annual Review of Marine Science*, 2(1):115--143. PMID: 21141660.

Dmitrenko, I. A., Polyakov, I. V., Kirillov, S. A., Timokhov, L. A., Frolov, I. E., Sokolov, V. T., Simmons, H. L., Ivanov, V. V., and Walsh, D. (2008). Toward a warmer Arctic Ocean: Spreading of the early 21st century Atlantic Water warm anomaly along the Eurasian Basin margins. *Journal of Geophysical Research (Oceans)*, 113:C05023.

Docquier, D., Grist, J. P., Roberts, M. J., Roberts, C. D., Semmler, T., Ponsoni, L., Massonnet, F., Sidorenko, D., Sein, D. V., Iovino, D., Bellucci, A., and Fichefet, T. (2019).

Impact of model resolution on Arctic sea ice and North Atlantic Ocean heat transport. *Climate Dynamics*, 53(7):4989--5017.

Dong, B. and Sutton, R. (2002). Variability in North Atlantic heat content and heat transport in a coupled ocean-atmosphere GCM. *Climate Dynamics*, 19(5):485--497.

Dong, B. and Sutton, R. T. (2003). Variability of Atlantic Ocean heat transport and its effects on the atmosphere. *Annals of Geophysics*, 46(1).

Dong, B. and Sutton, R. T. (2005). Mechanism of Interdecadal Thermohaline Circulation Variability in a Coupled Ocean-Atmosphere GCM. *Journal of Climate*, 18(8):1117--1135.

Dong, B.-W. and Sutton, R. T. (2001). The dominant mechanisms of variability in Atlantic Ocean Heat Transport in a Coupled Ocean-Atmosphere GCM. *Geophysical Research Letters*, 28(12):2445--2448.

Drijfhout, S. S. and Hazeleger, W. (2006). Changes in MOC and gyre-induced Atlantic Ocean heat transport. *Geophysical Research Letters*, 33(7).

Dunne, J. P., John, J. G., Adcroft, A. J., Griffies, S. M., Hallberg, R. W., Shevliakova, E., Stouffer, R. J., Cooke, W., Dunne, K. A., Harrison, M. J., Krasting, J. P., Malyshev, S. L., Milly, P. C. D., Phillipps, P. J., Sentman, L. T., Samuels, B. L., Spelman, M. J., Winton, M., Wittenberg, A. T., and Zadeh, N. (2012). GFDL's ESM2 Global Coupled Climate-Carbon Earth System Models. Part I: Physical Formulation and Baseline Simulation Characteristics. *Journal of Climate*, 25(19):6646--6665.

Dunne, J. P., John, J. G., Shevliakova, E., Stouffer, R. J., Krasting, J. P., Malyshev, S. L., Milly, P. C. D., Sentman, L. T., Adcroft, A. J., Cooke, W., Dunne, K. A., Griffies, S. M., Hallberg, R. W., Harrison, M. J., Levy, H., Wittenberg, A. T., Phillips, P. J., and Zadeh, N. (2013). GFDL's ESM2 Global Coupled Climate-Carbon Earth System Models. Part II:

Carbon System Formulation and Baseline Simulation Characteristics. *Journal of Climate*, 26(7):2247--2267.

Ebisuzaki, W. (1997). A Method to Estimate the Statistical Significance of a Correlation When the Data Are Serially Correlated. *Journal of Climate*, 10:2147--2153.

Eden, C. and Jung, T. (2001). North Atlantic Interdecadal Variability: Oceanic Response to the North Atlantic Oscillation (1865-1997). *Journal of Climate*, 14(5):676--691.

Ganachaud, A. and Wunsch, C. (2000). Improved estimates of global ocean circulation, heat transport and mixing from hydrographic data. *Nature*, 408(6811):453--457.

Ganachaud, A. and Wunsch, C. (2003). Large-Scale Ocean Heat and Freshwater Transports during the World Ocean Circulation Experiment. *Journal of Climate*, 16(4):696--705.

Garcia-Quintana, Y., Courtois, P., Hu, X., Pennelly, C., Kieke, D., and Myers, P. G. (2019). Sensitivity of Labrador Sea Water Formation to Changes in Model Resolution, Atmospheric Forcing, and Freshwater Input. *Journal of Geophysical Research: Oceans*, 124(3):2126--2152.

Gent, P. R., Danabasoglu, G., Donner, L. J., Holland, M. M., Hunke, E. C., Jayne, S. R., Lawrence, D. M., Neale, R. B., Rasch, P. J., Vertenstein, M., Worley, P. H., Yang, Z.-L., and Zhang, M. (2011). The Community Climate System Model Version 4. *Journal of Climate*, 24(19):4973--4991.

Good, S. A., M. J. M. and Rayner, N. A. (2013). EN4: Quality controlled ocean temperature and salinity profiles and monthly objective analyses with uncertainty estimates. *Journal of Geophysical Research: Oceans*, 118:6704--6716.

Gregory, J. M., Dixon, K. W., Stouffer, R. J., Weaver, A. J., Driesschaert, E., Eby, M., Fichefet, T., Hasumi, H., Hu, A., Jungclaus, J. H., Kamenkovich, I. V., Levermann, A.,

Montoya, M., Murakami, S., Nawrath, S., Oka, A., Sokolov, A. P., and Thorpe, R. B. (2005). A model intercomparison of changes in the Atlantic thermohaline circulation in response to increasing atmospheric CO2 concentration. *Geophysical Research Letters*, 32(12):n/a--n/a. L12703.

Grist, J. P., Josey, S. A., and Marsh, R. (2012). Surface estimates of the Atlantic overturning in density space in an eddy-permitting ocean model. *Journal of Geophysical Research: Oceans*, 117(C6).

Grist, J. P., Josey, S. A., Marsh, R., Kwon, Y.-O., Bingham, R. J., and Blaker, A. T. (2014). The Surface-Forced Overturning of the North Atlantic: Estimates from Modern Era Atmospheric Reanalysis Datasets. *Journal of Climate*, 27(10):3596--3618.

Grist, J. P., Marsh, R., and Josey, S. A. (2009). On the Relationship between the North Atlantic Meridional Overturning Circulation and the Surface-Forced Overturning Streamfunction. *Journal of Climate*, 22(19):4989--5002.

Groeskamp, S., Sloyan, B. M., Zika, J. D., and McDougall, T. J. (2017). Mixing Inferred from an Ocean Climatology and Surface Fluxes. *Journal of Physical Oceanography*, 47(3):667--687.

Gulev, S. K., Barnier, B., Molines, J.-M., Penduff, T., and Chanut, J. (2007). Impact of spatial resolution on simulated surface water mass transformations in the Atlantic. *Ocean Modelling*, 19(3):138 -- 160.

Haines, K. and Old, C. (2005). Diagnosing Natural Variability of North Atlantic Water Masses in HadCM3. *Journal of Climate*, 18(12):1925--1941.

Harada, Y., Kamahori, H., Kobayashi, C., Endo, H., Kobayashi, S., Ota, Y., Onoda, H., Onogi, K., Miyaoka, K., and Takahashi, K. (2016). The JRA-55 Reanalysis: Representa-

tion of Atmospheric Circulation and Climate Variability. *Meteorological magazine. No. 2*, 94(3):269--302.

Hersbach, H. and Dee, D. (2016). ERA5 reanalysis is in production. *ECMWF newsletter*, 147(7):5--6.

Heuze, C. (2017). North Atlantic deep water formation and AMOC in CMIP5 models. *Ocean Science*, 13(4):609--622.

Holland, M. and Bitz, C. (2003). Polar amplification of climate change in coupled models. *Climate Dynamics*, 21:221--232.

Huber, M. B. and Zanna, L. (2017). Drivers of uncertainty in simulated ocean circulation and heat uptake. *Geophysical Research Letters*, 44(3):1402--1413.

Hurrell, J. W. (2013). The community earth system model: A framework for collaborative research. *Bull. Amer. Meteor. Soc.*, 94:1339--1360.

Hwang, Y.-T., Frierson, D. M. W., and Kay, J. E. (2011). Coupling between Arctic feedbacks and changes in poleward energy transport. *Geophysical Research Letters*, 38(17). L17704.

Isachsen, P. E., Mauritzen, C., and Svendsen, H. (2007). Dense water formation in the Nordic Seas diagnosed from sea surface buoyancy fluxes. *Deep Sea Research Part I: Oceanographic Research Papers*, 54(1):22--41.

Jackson, L. C., Roberts, M. J., Hewitt, H. T., Iovino, D., Koenigk, T., Meccia, V. L., Roberts, C. D., Ruprich-Robert, Y., and Wood, R. A. (2020). Impact of ocean resolution and mean state on the rate of AMOC weakening. *Climate Dynamics*.

Jónsson, S. and Valdimarsson, H. (2012). Water mass transport variability to the North Icelandic shelf, 1994--2010. *ICES Journal of Marine Science*, 69(5):809--815.

Josey, S. A., Grist, J. P., and Marsh, R. (2009). Estimates of meridional overturning circulation variability in the North Atlantic from surface density flux fields. *Journal of Geophysical Research: Oceans*, 114(C9).

Jungclaus, J. H., Lohmann, K., and Zanchettin, D. (2014). Enhanced 20th-century heat transfer to the Arctic simulated in the context of climate variations over the last millennium. *Climate of the Past*, 10(6):2201--2213.

Katsman, C. A., Spall, M. A., and Pickart, R. S. (2004). Boundary Current Eddies and Their Role in the Restratification of the Labrador Sea. *Journal of Physical Oceanography*, 34(9):1967--1983.

Khatiwala, S., Schlosser, P., and Visbeck, M. (2002). Rates and Mechanisms of Water Mass Transformation in the Labrador Sea as Inferred from Tracer Observations. *Journal of Physical Oceanography*, 32(2):666--686.

Kim, W. M., Yeager, S., Chang, P., and Danabasoglu, G. (2018). Low-Frequency North Atlantic Climate Variability in the Community Earth System Model Large Ensemble. *Journal of Climate*, 31(2):787--813.

Kim, W. M., Yeager, S., and Danabasoglu, G. (2020). Atlantic Multidecadal Variability and Associated Climate Impacts Initiated by Ocean Thermohaline Dynamics. *Journal of Climate*, 33(4):1317--1334.

Kim, W. M., Yeager, S., and Danabasoglu, G. (2021). Revisiting the Causal Connection between the Great Salinity Anomaly of the 1970s and the Shutdown of Labrador Sea Deep Convection. *Journal of Climate*, 34(2):675 -- 696.

Knight, J. R., Allan, R. J., Folland, C. K., Vellinga, M., and Mann, M. E. (2005). A signature of persistent natural thermohaline circulation cycles in observed climate. *Geophysical Research Letters*, 32(20).

Kobayashi, S., Ota, Y., Harada, Y., Ebita, A., Moriya, M., Onoda, H., Onogi, K., Kamahori, H., Kobayashi, C., Endo, H., Miyaoka, K., and Takahashi, K. (2015). The JRA-55 Reanalysis: General Specifications and Basic Characteristics. *Meteorological magazine. No. 2*, 93(1):5--48.

Koenigk, T. and Brodeau, L. (2014). Ocean heat transport into the Arctic in the twentieth and twenty-first century in EC-Earth. *Climate Dynamics*, 42(11):3101--3120.

Koenigk, T., Fuentes-Franco, R., Meccia, V., Gutjahr, O., Jackson, L. C., New, A. L., Ortega, P., Roberts, C., Roberts, M., Arsouze, T., Iovino, D., Moine, M.-P., and Sein, D. V. (2020). Deep water formation in the North Atlantic Ocean in high resolution global coupled climate models. *Ocean Science Discussions*, 2020:1--39.

Kostov, Y., Armour, K. C., and Marshall, J. (2014). Impact of the Atlantic meridional overturning circulation on ocean heat storage and transient climate change. *Geophysical Research Letters*, 41(6):2108--2116.

Kuhlbrodt, T., Jones, C. G., Sellar, A., Storkey, D., Blockley, E., Stringer, M., Hill, R., Graham, T., Ridley, J., Blaker, A., Calvert, D., Copsey, D., Ellis, R., Hewitt, H., Hyder, P., Ineson, S., Mulcahy, J., Siahaan, A., and Walton, J. (2018). The Low-Resolution Version of HadGEM3 GC3.1: Development and Evaluation for Global Climate. *Journal of Advances in Modeling Earth Systems*, 10(11):2865--2888.

Kushnir, Y. (1994). Interdecadal Variations in North Atlantic Sea Surface Temperature and Associated Atmospheric Conditions. *Journal of Climate*, 7(1):141--157.

Kwon, Y.-O. and Frankignoul, C. (2014). Mechanisms of Multidecadal Atlantic Meridional Overturning Circulation Variability Diagnosed in Depth versus Density Space. *Journal of Climate*, 27(24):9359--9376.

L. Bryden, H. and Imawaki, S. (2001). Chapter 6.1 Ocean heat transport. In Siedler, G., Church, J., and Gould, J., editors, *Ocean Circulation and Climate*, volume 77 of *International Geophysics*, pages 455--474. Academic Press.

Langehaug, H. R., Medhaug, I., Eldevik, T., and Otterå, O. H. (2012a). Arctic/Atlantic Exchanges via the Subpolar Gyre. *Journal of Climate*, 25(7):2421--2439.

Langehaug, H. R., Rhines, P. B., Eldevik, T., Mignot, J., and Lohmann, K. (2012b). Water mass transformation and the North Atlantic Current in three multicentury climate model simulations. *Journal of Geophysical Research: Oceans*, 117(C11).

Large, W. G., McWilliams, J. C., and Doney, S. C. (1994). Oceanic vertical mixing: A review and a model with a nonlocal boundary layer parameterization. *Reviews of Geophysics*, 32(4):363--403.

Latarius, K. and Quadfasel, D. (2016). Water mass transformation in the deep basins of the Nordic Seas: Analyses of heat and freshwater budgets. *Deep Sea Research Part I: Oceanographic Research Papers*, 114:23 -- 42.

Lazier, J., Hendry, R., Clarke, A., Yashayaev, I., and Rhines, P. (2002). Convection and restratification in the Labrador Sea, 1990-2000. *Deep Sea Research Part I: Oceanographic Research Papers*, 49(10):1819--1835.

Levitus, S. (1983). Climatological Atlas of the World Ocean. *Eos, Transactions American Geophysical Union*, 64(49):962--963.

Li, F., Lozier, M. S., Danabasoglu, G., Holliday, N. P., Kwon, Y.-O., Romanou, A., Yeager, S. G., and Zhang, R. (2019). Local and Downstream Relationships between Labrador Sea Water Volume and North Atlantic Meridional Overturning Circulation Variability. *Journal of Climate*, 32(13):3883--3898.

Li, D., R. Z. and Knutson, T. (2017). On the discrepancy between observed and CMIP5 multi-model simulated Barents Sea winter sea ice decline. *Nature Communications*, 8(14991).

Lilly, J. M., Rhines, P. B., Schott, F., Lavender, K., Lazier, J., Send, U., and D'Asaro, E. (2003). Observations of the Labrador Sea eddy field. *Progress in Oceanography*, 59(1):75--176.

Lozier, M. S., Li, F., Bacon, S., Bahr, F., Bower, A. S., Cunningham, S. A., de Jong, M. F., de Steur, L., deYoung, B., Fischer, J., Gary, S. F., Greenan, B. J. W., Holliday, N. P., Houk, A., Houpert, L., Inall, M. E., Johns, W. E., Johnson, H. L., Johnson, C., Karstensen, J., Koman, G., Le Bras, I. A., Lin, X., Mackay, N., Marshall, D. P., Mercier, H., Oltmanns, M., Pickart, R. S., Ramsey, A. L., Rayner, D., Straneo, F., Thierry, V., Torres, D. J., Williams, R. G., Wilson, C., Yang, J., Yashayaev, I., and Zhao, J. (2019). A sea change in our view of overturning in the subpolar North Atlantic. *Science*, 363(6426):516--521.

Lumpkin, R. and Speer, K. (2003). Large-Scale Vertical and Horizontal Circulation in the North Atlantic Ocean. *Journal of Physical Oceanography*, 33(9):1902--1920.

MacMartin, D. G., Tziperman, E., and Zanna, L. (2013). Frequency Domain Multimodel Analysis of the Response of Atlantic Meridional Overturning Circulation to Surface Forcing. *Journal of Climate*, 26(21):8323--8340.

MacMartin, D. G., Zanna, L., and Tziperman, E. (2016). Suppression of Atlantic Meridional Overturning Circulation Variability at Increased CO2. *Journal of Climate*, 29(11):4155--4164.

Mahajan, S., Zhang, R., and Delworth, T. L. (2011). Impact of the Atlantic Meridional Overturning Circulation (AMOC) on Arctic Surface Air Temperature and Sea Ice Variability. *Journal of Climate*, 24(24):6573--6581.

Mahlstein, I. and Knutti, R. (2011). Ocean Heat Transport as a Cause for Model Uncertainty in Projected Arctic Warming. *Journal of Climate*, 24(5):1451--1460.

Manabe, S. and Stouffer, R. J. (1988). Two Stable Equilibria of a Coupled Ocean-Atmosphere Model. *Journal of Climate*, 1(9):841--866.

Marsh, R. (2000). Recent Variability of the North Atlantic Thermohaline Circulation Inferred from Surface Heat and Freshwater Fluxes. *Journal of Climate*, 13(18):3239--3260.

Marshall, J., Armour, K., Scott, J., Kostov, Y., Hausmann, U., Ferreira, D., Shepherd, T., and Bitz, C. (2014a). The ocean's role in polar climate change: asymmetric Arctic and Antarctic responses to greenhouse gas and ozone forcing. *Philosophical Transactions of the Royal Society*, 372(20130040).

Marshall, J., Scott, J. R., Armour, K. C., Campin, J. M., Kelley, M., and Romanou, A. (2014b). The ocean's role in the transient response of climate to abrupt greenhouse gas forcing. *Climate Dynamics*, 44(7):2287--2299.

McCartney, M. S. and Talley, L. D. (1982). The Subpolar Mode Water of the North Atlantic Ocean. *Journal of Physical Oceanography*, 12(11):1169--1188.

Mecking, J. V., Keenlyside, N. S., and Greatbatch, R. J. (2015). Multiple timescales of stochastically forced North Atlantic Ocean variability: A model study. *Ocean Dynamics*, 65(9):1367--1381.

Megann, A. (2018). Estimating the numerical diapycnal mixing in an eddy-permitting ocean model. *Ocean Modelling*, 121:19--33.

Menary, M. B., Hodson, D. L. R., Robson, J. I., Sutton, R. T., and Wood, R. A. (2015a). A Mechanism of Internal Decadal Atlantic Ocean Variability in a High-Resolution Coupled Climate Model. *Journal of Climate*, 28(19):7764--7785.

Menary, M. B., Hodson, D. L. R., Robson, J. I., Sutton, R. T., Wood, R. A., and Hunt, J. A. (2015b). Exploring the impact of CMIP5 model biases on the simulation of North Atlantic decadal variability. *Geophysical Research Letters*, 42(14):5926--5934. 2015GL064360.

Menary, M. B., Jackson, L. C., and Lozier, M. S. (2020). Reconciling the Relationship Between the AMOC and Labrador Sea in OSNAP Observations and Climate Models. *Geophysical Research Letters*, 47(18):e2020GL089793. e2020GL089793 10.1029/2020GL089793.

Menary, M. B., Kuhlbrodt, T., Ridley, J., Andrews, M. B., Dimdore-Miles, O. B., Deshayes, J., Eade, R., Gray, L., Ineson, S., Mignot, J., Roberts, C. D., Robson, J., Wood, R. A., and Xavier, P. (2018). Preindustrial Control Simulations With HadGEM3-GC3.1 for CMIP6. *Journal of Advances in Modeling Earth Systems*, 10(12):3049--3075.

Mignot, J., de Boyer Montégut, C., Lazar, A., and Cravatte, S. (2007). Control of salinity on the mixed layer depth in the world ocean: 2. Tropical areas. *Journal of Geophysical Research: Oceans*, 112(C10).

Msadek, R., Johns, W. E., Yeager, S. G., Danabasoglu, G., Delworth, T. L., and Rosati, A. (2013). The Atlantic Meridional Heat Transport at 26.5 °N and Its Relationship with the MOC in the RAPID Array and the GFDL and NCAR Coupled Models. *Journal of Climate*, 26(12):4335--4356.

Nummelin, A., Li, C., and Hezel, P. J. (2017). Connecting ocean heat transport changes from the midlatitudes to the Arctic Ocean. *Geophysical Research Letters*, 44(4):1899--1908. 2016GL071333.

Nurser, A. J. G., Marsh, R., and Williams, R. G. (1999). Diagnosing Water Mass Formation from Air-Sea Fluxes and Surface Mixing. *Journal of Physical Oceanography*, 29(7):1468--1487.

Oldenburg, D., Armour, K. C., Thompson, L., and Bitz, C. M. (2018). Distinct Mechanisms of Ocean Heat Transport Into the Arctic Under Internal Variability and Climate Change. *Geophysical Research Letters*, 45(15):7692--7700.

Oldenburg, D., Wills, R. C. J., Armour, K. C., Thompson, L., and Jackson, L. C. (2021). Mechanisms of Low-Frequency Variability in North Atlantic Ocean Heat Transport and AMOC. *Journal of Climate*, 34(12):4733--4755.

Parsons, L. A., Yin, J., Overpeck, J. T., Stouffer, R. J., and Malyshev, S. (2014). Influence of the Atlantic Meridional Overturning Circulation on the monsoon rainfall and carbon balance of the American tropics. *Geophysical Research Letters*, 41(1):146--151.

Peixoto, J. P. and Oort, A. H. (1993). Physics of Climate. *American Institute of Physics, New York*, page 520.

Pérez-Brunius, P., Rossby, T., and Watts, D. R. (2004). Transformation of the Warm Waters of the North Atlantic from a Geostrophic Streamfunction Perspective. *Journal of Physical Oceanography*, 34(10):2238--2256.

Petit, T., Lozier, M. S., Josey, S. A., and Cunningham, S. A. (2020). Atlantic Deep Water Formation Occurs Primarily in the Iceland Basin and Irminger Sea by Local Buoyancy Forcing. *Geophysical Research Letters*, 47(22):e2020GL091028. e2020GL091028 2020GL091028.

Pickart, R. S. and Spall, M. A. (2007). Impact of Labrador Sea Convection on the North Atlantic Meridional Overturning Circulation. *Journal of Physical Oceanography*, 37(9):2207--2227.

Piecuch, C. G. and Ponte, R. M. (2011). Mechanisms of interannual steric sea level variability. *Geophysical Research Letters*, 38(15).

Pithan, F. and Mauritsen, T. (2014). Arctic amplification dominated by temperature feedbacks in contemporary climate models. *Nature Geoscience*, 7(3):181--184.

Radko, T., Kamenkovich, I., and Dare, P.-Y. (2008). Inferring the Pattern of the Oceanic Meridional Transport from the Air-Sea Density Flux. *Journal of Physical Oceanography*, 38(12):2722--2738.

Rahmstorf, S. (2002). Ocean circulation and climate during the past 120,000 years. *Nature*, 419(6903):207--214.

Reynolds, R. W., Rayner, N. A., Smith, T. M., Stokes, D. C., and Wang, W. (2002). An Improved In Situ and Satellite SST Analysis for Climate. *Journal of Climate*, 15(13):1609--1625.

Rhines, P., Häkkinen, S., and Josey, S. A. (2008). *Is Oceanic Heat Transport Significant in the Climate System?*, pages 87--109. Springer Netherlands, Dordrecht.

Roberts, M. J., Baker, A., Blockley, E. W., Calvert, D., Coward, A., Hewitt, H. T., Jackson, L. C., Kuhlbrodt, T., Mathiot, P., Roberts, C. D., Schiemann, R., Seddon, J., Vannière, B., and Vidale, P. L. (2019). Description of the resolution hierarchy of the global coupled HadGEM3-GC3.1 model as used in CMIP6 HighResMIP experiments. *Geoscientific Model Development*, 12(12):4999--5028.

Roberts, M. J., Jackson, L. C., Roberts, C. D., Meccia, V., Docquier, D., Koenigk, T., Ortega, P., Moreno-Chamarro, E., Bellucci, A., Coward, A., Drijfhout, S., Exarchou, E., Gutjahr, O., Hewitt, H., Iovino, D., Lohmann, K., Putrasahan, D., Schiemann, R., Seddon, J., Terray, L., Xu, X., Zhang, Q., Chang, P., Yeager, S. G., Castruccio, F. S., Zhang, S., and Wu, L. (2020). Sensitivity of the Atlantic Meridional Overturning Circulation to Model Resolution in CMIP6 HighResMIP Simulations and Implications for Future Changes. *Journal of Advances in Modeling Earth Systems*. e2019MS002014 2019MS002014.

Rugenstein, M. A. A., Winton, M., Stouffer, R. J., Griffies, S. M., and Hallberg, R. (2013). Northern High-Latitude Heat Budget Decomposition and Transient Warming. *Journal of Climate*, 26(2):609--621.

Schauer, U., Fahrbach, E., Osterhus, S., and Rohardt, G. (2004). Arctic warming through the Fram Strait-Oceanic heat transport from three years of measurements. *Journal of geophysical research, 109(C6), C06026*.

Schlesinger, M. E. and Ramankutty, N. (1994). An oscillation in the global climate system of period 65-70 years. *Nature*, 367(6465):723--726.

Schneider, T. and Griffies, S. (1999). A Conceptual Framework for Predictability Studies. *Journal of Climate*, 12:3133--3155.

Schneider, T. and Held, I. M. (2001). Discriminants of Twentieth-Century Changes in Earth Surface Temperatures. *Journal of Climate*, 14(3):249--254.

Sein, D. V., Koldunov, N. V., Danilov, S., Sidorenko, D., Wekerle, C., Cabos, W., Rackow, T., Scholz, P., Semmler, T., Wang, Q., and Jung, T. (2018). The Relative Influence of Atmospheric and Oceanic Model Resolution on the Circulation of the North Atlantic Ocean in a Coupled Climate Model. *Journal of Advances in Modeling Earth Systems*, 10(8):2026--2041.

Serreze, M. C., Barrett, A. P., Stroeve, J. C., Kindig, D. N., and Holland, M. M. (2009). The emergence of surface-based Arctic amplification. *The Cryosphere*, 3(1):11--19.

Singh, H. A., Rasch, P. J., and Rose, B. E. J. (2017). Increased Ocean Heat Convergence Into the High Latitudes With CO2 Doubling Enhances Polar-Amplified Warming. *Geophysical Research Letters*, 44(20):10,583--10,591.

Skagseth, Ø., Furevik, T., Ingvaldsen, R., Loeng, H., Mork, K. A., Orvik, K. A., and Ozhigin, V. (2008). *Volume and Heat Transports to the Arctic Ocean Via the Norwegian and Barents Seas*, pages 45--64. Springer Netherlands, Dordrecht.

Smeed, D. A., McCarthy, G. D., Cunningham, S. A., Frajka-Williams, E., Rayner, D., Johns, W. E., Meinen, C. S., Baringer, M. O., Moat, B. I., Duchez, A., and Bryden, H. L. (2014). Observed decline of the Atlantic meridional overturning circulation 2004-2012. *Ocean Science*, 10(1):29--38.

Smethie, W. M. and Fine, R. A. (2001). Rates of North Atlantic Deep Water formation calculated from chlorofluorocarbon inventories. *Deep-Sea Research Part I: Oceanographic Research Papers*, 48(1):189--215.

Spall, M. (2004). Boundary Currents and Watermass Transformation in Marginal Seas. *Journal of Physical Oceanography - J PHYS OCEANOGR*, 34.

Speer, K. and Tziperman, E. (1992). Rates of Water Mass Formation in the North Atlantic Ocean. *Journal of Physical Oceanography*, 22(1):93--104.

Speer, K. G. (1997). A note on average cross-isopycnal mixing in the North Atlantic ocean. *Deep Sea Research Part I: Oceanographic Research Papers*, 44(12):1981--1990.

Straneo, F. (2006a). Heat and Freshwater Transport through the Central Labrador Sea. *Journal of Physical Oceanography*, 36(4):606--628.

Straneo, F. (2006b). On the Connection between Dense Water Formation, Overturning, and Poleward Heat Transport in a Convective Basin. *Journal of Physical Oceanography*, 36(9):1822--1840.

Swift, J. H. and Aagaard, K. (1981). Seasonal transitions and water mass formation in the

Iceland and Greenland seas. *Deep Sea Research Part A. Oceanographic Research Papers*, 28(10):1107--1129.

Tandon, A. and Zhao, L. (2004). Mixed layer transformation for the North Atlantic for 1990-2000. *Journal of Geophysical Research: Oceans*, 109(C5).

Taylor, K. E., Stouffer, R. J., and Meehl, G. A. (2012). An Overview of CMIP5 and the Experiment Design. *Bulletin of the American Meteorological Society*, 93(4):485--498.

Thornalley, D. J. R., Oppo, D. W., Ortega, P., Robson, J. I., Brierley, C. M., Davis, R., Hall, I. R., Moffa-Sanchez, P., Rose, N. L., Spooner, P. T., Yashayaev, I., and Keigwin, L. D. (2018). Anomalously weak Labrador Sea convection and Atlantic overturning during the past 150 years. *Nature*, 556(7700):227--230.

Ting, M., Kushnir, Y., Seager, R., and Li, C. (2009). Forced and Internal Twentieth-Century SST Trends in the North Atlantic. *Journal of Climate*, 22(6):1469--1481.

Treguier, A. M., Theetten, S., Chassignet, E. P., Penduff, T., Smith, R., Talley, L., Beismann, J. O., and Böning, C. (2005). The North Atlantic Subpolar Gyre in Four High-Resolution Models. *Journal of Physical Oceanography*, 35(5):757--774.

Trossman, D. S., Thompson, L., Mecking, S., and Warner, M. J. (2012). On the formation, ventilation, and erosion of mode waters in the North Atlantic and Southern Oceans. *Journal of Geophysical Research: Oceans*, 117(C9).

Tulloch, R. and Marshall, J. (2012). Exploring Mechanisms of Variability and Predictability of Atlantic Meridional Overturning Circulation in Two Coupled Climate Models. *Journal of Climate*, 25(12):4067--4080.

Tziperman, E. (1986). On the Role of Interior Mixing and Air-Sea Fluxes in Determining the Stratification and Circulation of the Oceans. *Journal of Physical Oceanography*, 16(4):680--693.

Venzke, S., Allen, M. R., Sutton, R. T., and Rowell, D. P. (1999). The Atmospheric Response over the North Atlantic to Decadal Changes in Sea Surface Temperature. *Journal of Climate*, 12(8):2562--2584.

Vörösmarty, C., Fekete, B., Meybeck, M., and Lammers, R. (2000). Geomorphometric attributes of the global system of rivers at 30-minute spatial resolution. *Journal of Hydrology*, 237(1):17--39.

Walin, G. (1982). On the relation between sea-surface heat flow and thermal circulation in the ocean. *Tellus*, 34(2):187--195.

Wekerle, C., Wang, Q., Danilov, S., Schourup-Kristensen, V., von Appen, W.-J., and Jung, T. (2017). Atlantic Water in the Nordic Seas: Locally eddy-permitting ocean simulation in a global setup. *Journal of Geophysical Research: Oceans*, 122(2):914--940.

Wen, N., Frankignoul, C., and Gastineau, G. (2016). Active AMOC-NAO coupling in the IPSL-CM5A-MR climate model. *Climate Dynamics*, 47(7):2105--2119.

Wills, R. C. and Schneider, T. (2015). Stationary Eddies and the Zonal Asymmetry of Net Precipitation and Ocean Freshwater Forcing. *Journal of Climate*, 28(13):5115--5133.

Wills, R. C., Schneider, T., Wallace, J. M., Battisti, D. S., and Hartmann, D. L. (2018). Disentangling Global Warming, Multidecadal Variability, and El Niño in Pacific Temperatures. *Geophysical Research Letters*, 45(5):2487--2496.

Wills, R. C. J., Armour, K. C., Battisti, D. S., and Hartmann, D. L. (2019a). Ocean-Atmosphere Dynamical Coupling Fundamental to the Atlantic Multidecadal Oscillation. *Journal of Climate*, 32(1):251--272.

Wills, R. C. J., Battisti, D. S., Proistosescu, C., Thompson, L., Hartmann, D. L., and Armour, K. C. (2019b). Ocean Circulation Signatures of North Pacific Decadal Variability. *Geophysical Research Letters*, 46(3):1690--1701.

Xu, X., Rhines, P. B., and Chassignet, E. P. (2018). On Mapping the Diapycnal Water Mass Transformation of the Upper North Atlantic Ocean. *Journal of Physical Oceanography*, 48(10):2233--2258.

Yan, X., Zhang, R., and Knutson, T. R. (2017). The role of Atlantic overturning circulation in the recent decline of Atlantic major hurricane frequency. *Nature Communications*, 8(1):1695.

Yan, X., Zhang, R., and Knutson, T. R. (2018). Underestimated AMOC Variability and Implications for AMV and Predictability in CMIP Models. *Geophysical Research Letters*, 45(9):4319--4328.

Yeager, S. (2015). Topographic Coupling of the Atlantic Overturning and Gyre Circulations. *Journal of Physical Oceanography*, 45(5):1258--1284.

Yeager, S. G., Karspeck, A. R., and Danabasoglu, G. (2015). Predicted slowdown in the rate of Atlantic sea ice loss. *Geophysical Research Letters*, 42(24):10,704--10,713. 2015GL065364.

Yu, L., X. J. and Weller, R. A. (2008). Multidecade Global Flux Datasets from the Objectively Analyzed Air-sea Fluxes (OAFlux) Project: Latent and sensible heat fluxes, ocean evaporation, and related surface meteorological variables. *OAFlux Project Technical Report*, OA-2008-01.

Zhang, L. and Wang, C. (2013). Multidecadal North Atlantic sea surface temperature and Atlantic meridional overturning circulation variability in CMIP5 historical simulations. *Journal of Geophysical Research: Oceans*, 118(10):5772--5791.

Zhang, R. (2010). Latitudinal dependence of Atlantic meridional overturning circulation (AMOC) variations. *Geophysical Research Letters*, 37(16).

Zhang, R. (2015). Mechanisms for low-frequency variability of summer Arctic sea ice extent. *Proceedings of the National Academy of Sciences*, 112(15):4570--4575.

Zou, S., Lozier, M. S., Li, F., Abernathey, R., and Jackson, L. (2020). Density-compensated overturning in the Labrador Sea. *Nature Geoscience*.